LEIBNIZ-INSTITUT FÜR ATMOSPHÄREN PHYSIK IAP

Application of a constant temperature anemometer for balloon-borne stratospheric turbulence soundings

Olga Alicja Sumińska

December 5, 2008

Thesis submitted for the degree of Master of Science of the University of Rostock

Leibniz Institute for Atmospheric Physics
in Kühlungsborn

Abstract

This thesis presents the development of hardware and software for a high-resolution observation system for in-situ investigation of stratospheric turbulence. It presents also a description of laboratory and field tests, first results and analysis of collected data. The setup, consisting of a constant temperature hot-wire anemometer and data handling system, was placed in the payload of a meteorological balloon and lifted to the height of about 35 km. The position of the setup, as well as the data necessary for temperature and density correction, were provided by a meteorological radiosonde. The acquired wind data were both stored on an SD-card and transmitted by a telemetry system to a stationary receiver in the Leibniz Institute of Atmospheric Physics (IAP) in Kühlungsborn, Germany. The high frequency response of the hot-wire anemometer enabled an investigation of stratospheric turbulent layers with spatial resolution of 0.25 cm. The results show that a constant temperature hot-wire anemometer is an effective instrument in investigation of turbulent layers in the stratosphere.

Contents

1 Introduction **1**
1.1 The Atmosphere . . . 1
1.2 Thermodynamics of the dry atmosphere . . . 2
1.3 Motivation . . . 4

2 Turbulence in the atmosphere **11**
2.1 Basics of turbulence theory . . . 11
2.2 The origin of turbulence in the free atmosphere . . . 14
2.3 Methods of stratospheric turbulence measurements . . . 15
2.3.1 In-situ methods . . . 16
2.3.2 Remote sensing . . . 17

3 Constant Temperature Anemometry **19**
3.1 Basic principles of hot-wire anemometry . . . 19
3.2 Turbulence measurements with CTA . . . 22
3.3 Hardware . . . 22
3.4 Bridge adjustment and calibration . . . 23
3.5 Temperature and density effect . . . 26

4 Supporting instrumentation **29**
4.1 Radiosonde system . . . 29
4.2 Telemetry . . . 30
4.2.1 Modem and transmitting antenna . . . 31
4.2.2 Receiving antenna . . . 32
4.3 The recovery system . . . 33

5 Analysis software **35**
5.1 WindData software . . . 35
5.2 Methods of mathematical analysis . . . 37

6 Test measurements **41**
6.1 Wind tunnel experiments . . . 41
6.1.1 Calibration . . . 41
6.1.2 Contamination effect . . . 45
6.1.3 Pitch and yaw effects . . . 45

6.2 Tests in vacuum chamber 48
6.3 Comparison of 55P13 and 55P03 probe 49
6.4 Turbulence spectrum from on-ground measurements 52

7 Balloon-borne experiment **61**
7.1 Measurements overview 62
7.2 CTA data analysis 66
7.3 Comparison of CTA and radar measurements 72
7.4 Discussion 73

8 Summary and outlook **77**

List of Figures **81**

References **84**

1 Introduction

1.1 The Atmosphere

The Earth's atmosphere is a very complicated, dynamic system which plays a significant role in transport of energy from the Sun to the Earth's surface, as well as in the transport of energy, momentum and chemical constituents between regions of the Earth. The state of the atmosphere is characterized by various physical quantities, like pressure, density, temperature and velocity, which strongly correlate with each other. The most common division of the atmosphere is the one according to major changes in the temperature gradient. Figure 1.1 shows four atmospheric layers with respect to the conditions at Kühlungsborn, Germany (54°07'N, 11°46'E). The profile from the left plot is based on lidar observations between 1 and 98 km and can serve as a representative example of summer mid-latitude conditions.

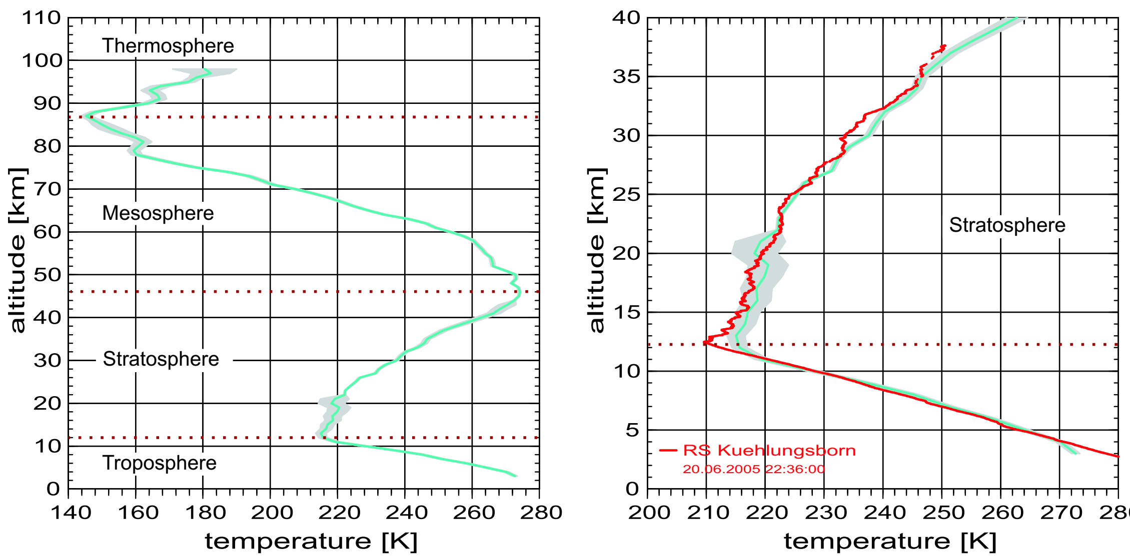

Figure 1.1: A night temperature profile from 20th June 2005 in Kühlungsborn, Germany. The left plot shows lidar measurements of temperature between 1 and 98 km. The brown dotted horizontal lines indicate the "pauses" between the atmospheric layers. The right plot shows the temperature profile in the troposphere and the stratosphere; the lidar measurements are presented by a cyan curve with grey shaded uncertainty, the red line shows a temperature profile obtained from collocated radiosonde observations [*Gerding et al.*, 2008].

The lowest of the atmospheric layers, the so called troposphere, is characterized by a negative vertical temperature gradient. It extends from the Earth's surface up to an altitude at which the temperature gradient is bigger than -2 K/km. The latter region is known as the tropopause and typically is located between 10 km and 12 km at mid latitudes. Above this region, in the stratosphere, as shown in the Figure 1.1, the temperature increases with altitude up to a level at which the temperature reaches its local maximum. This is known as the stratopause and is located at an altitude of approximately 50 km. This vertical thermal structure arises from complex radiative and dynamical processes. The stratosphere is heated due to the absorption of ultraviolet radiation by ozone. Thus, the vertical stratification, with warmer layers above and cooler layers below, occurs and makes the stratosphere *statically stable* in contrast to the troposphere. That results also in intense interactions among radiative, dynamical, and chemical processes, in which horizontal mixing of gaseous components proceeds much more rapidly than vertical mixing. The relationship between the vertical temperature structure and *static stability* will be described further in Chapter 1.2.

The next region, the mesosphere, is characterized by a negative vertical gradient. The division between the mesosphere and the next layer, namely the thermosphere is called the mesopause. The thermosphere extends upwards from the mesopause and is characterized by increasing temperature. The air in the thermosphere is thin in comparison with other layers and a small change in energy can cause a large change in temperature. That's why the temperature in this layer is very sensitive to solar activity.

This vertical thermal structure of the Earth's atmosphere is strongly combined with the dynamics. All the layers interact with each other through mixing of the air and constituents, as well as by the momentum transport. To understand the atmosphere it is necessary to regard it as an ensemble, that is constantly influenced by various coupled processes. Consequently, the full and complete description of this atmosphere requires consideration of the influence of both large- and small-scale motions (see Figure 1.2) on the momentum balance and mass circulation. Although a lot of work has been done in large-scale observation and numerical simulations, there are still many questions to be answered. Most of them consider the small-scales motions. The main reason for this is the difficulty of sounding of these structures.

1.2 Thermodynamics of the dry atmosphere

Static stability plays a very important role in investigation of the atmospheric turbulence. It gives information on the atmospheric regions, where the turbulence can be expected to occur. This chapter describes shortly the basics of atmospheric dynamics and introduces the static stability in terms of atmospheric quantities.

In studies of atmospheric dynamics, the atmosphere can be considered as a continuous fluid medium, or *continuum*. An *air parcel* in this continuum is regarded as an imaginary volume element that is very small compared with the volume of the atmosphere but still contains a large number of molecules. Because air is compressible, the changes experienced by an air parcel include adiabatic expansion and compression when the air parcel rises and descends. As the air parcel is displaced adiabatically, up or down in the atmosphere, a temperature lapse rate Γ_d, known as the dry adiabatic lapse rate will be then given by

$$\Gamma_d = -\frac{\partial T}{\partial z} = \frac{g}{c_p} \tag{1.1}$$

where g is the gravitational acceleration and c_p is the specific heat of air at a constant pressure. The dry adiabatic lapse rate is approximately 9.8 K/km in the troposphere and the lower stratosphere. In a stably stratified atmosphere, cooling occurs for upward displacements, and warming results from downward displacements. Thus, when vertical motion is not uniformly distributed in the atmosphere, air parcels with the most relative displacement experience the greatest temperature differences from the surrounding air mass. Subsequently, as a rising parcel becomes cooler and more dense than the surrounding air mass, the force of gravity causes buoyancy effects to restore the parcel toward its original altitude levels. Conversely, as a descending parcel becomes warmer or less dense than the surrounding ambient air, it experiences restoring buoyancy which forces it toward its original altitude.

Since the temperature of an air parcel will change in the case of vertical displacement, it is useful to define a measure of temperature which remains constant as long as the air parcel moves adiabatically. The potential temperature, Θ, is such a quantity. It is defined as the temperature that a parcel of dry air at pressure p would have if it was brought adiabatically to a standard pressure p_s. It is given by

$$\Theta = T(p_s/p)^{R/c_p} \tag{1.2}$$

where T is the current absolute temperature (in K) and R is the gas constant of air. If the potential temperature is a function of height, the atmospheric lapse rate $\Gamma = -\partial T/\partial z$, may differ from the adiabatic lapse rate and

$$\frac{T}{\Theta}\frac{\partial \Theta}{\partial z} = \Gamma_d - \Gamma \tag{1.3}$$

This difference is observed for example when wind blows over a mountain. An air current experiences then an orographic lift, which causes periodic changes of atmospheric pressure, temperature and orthometric height in a flow. A difference between the atmospheric and adiabatic lapse rate can also be caused by the surface wind blowing over an escarpment or plateau, by upper winds deflected over a thermal updraft or cloud street, or by frontal systems.

From Eq. 1.3 one can easily verify that when the actual temperature lapse rate is less then the adiabatic lapse rate ($\Gamma < \Gamma_d$), potential temperature Θ increases with height. In this case, an air parcel undergoing an adiabatic displacement from its equilibrium level, will be positively (negatively) buoyant when displaced vertically downward (upward) and will return to its equilibrium level. The atmosphere is then said to be statically stable or *stably stratified*. The resulting imbalance between the buoyancy and gravitational force causes air parcels to perform simple harmonic motions in a vertical direction around their equilibrium positions. This adiabatic oscillation leads to evolution of *internal* *gravity waves*, which strongly influence the temperature profile and are important factor in momentum and energy transport in the atmosphere. The angular frequency of this oscillation is known as the Brunt-Väisälä or buoyancy frequency, N. It is related to the potential temperature, Θ, by

$$N^2 = \frac{g \partial ln\Theta}{\partial z} \tag{1.4}$$

Like the vertical gradient of the potential temperature, the Brunt-Väisälä frequency is a measure of static stability. A positive value of N^2 indicates that the atmosphere is statically stable and the value increases with increasing static stability.

In the stratosphere, where ambient temperatures increase with altitude, the parcel temperature grows at rates of 10 to 13 K/km, causing the buoyancy forces to act as a stiff spring. In comparison, weaker spring force effects are experienced in the troposphere and mesosphere, where parcel temperature grows at rates from 4 to 8 K/km. This effect, in which parcel altitude displacements are opposed by buoyancy forces, is much stronger in the stratosphere than in either the troposphere or the mesosphere. The time scales corresponding to the Brunt-Väisälä frequency have typical values of approximately 4 min in the stratosphere, 10 -20 min in the troposphere and 6 min in the mesosphere. Due to this exhibited stability in time and space and because of the absence of regular convection, the processes in the stratosphere take place very slowly compared to those in the troposphere. All these factors combined with the additional decrease of density make the stratosphere a proper place for amplification and partial breaking of gravity waves, which further can result in the creation of turbulent layers.

1.3 Motivation

The Earth's atmosphere is in continuous motion of a varied and complex nature. In the atmosphere one can distinguish phenomena, or features, whose typical size and typical lifetime cover a very wide range. The spatial scales of those phenomena are determined by their typical size (or wavelength) and the time-scales by their lifetime (or period). The scales of the horizontally largest features are comparable to the sizes of the Earth (Rossby waves). The turbulence, on the contrary, can have a spatial scales of only a few millimeters. Between all the atmospheric phenomena, the energy transport, from the largest to the smallest scales, occurs. Figure 1.2 shows characteristic length scales associated with turbulence in the atmosphere as calculated by Prof. Dr. F.-J. Lübken from IAP, Kühlungsborn. The presented scales indicate the breakpoints between subranges, at which different forces dominate. Further description of the scales of turbulence is enclosed in Chapter 2.1.

One of the most important factors in energy transport in the atmosphere are the gravity waves. Figure 1.3 shows gravity waves structure in temperature field. The measurements were carried out with lidar system at IAP, Kühlungsborn at night between 12th and 13th November 2003. Gravity waves are able to transport momentum many kilometers upward from the Earth's surface during their propagation through the atmosphere. Their main impact on the dynamical state of atmosphere takes place at altitudes between 10 and 100 km. Furthermore, the breaking of gravity waves is a direct source of turbulence in the stratosphere as well as in the mesosphere. The models and measurements accomplished in the middle atmosphere indicate great importance of gravity waves and turbulence for understanding of this region. In the mesosphere the gravity waves strongly influence the energy budget. In the stratosphere their impact on the energy budget is relatively weaker. However, turbulence in this region indicates the gravity waves breaking and that gives information on the 'missing' energy in the mesosphere.

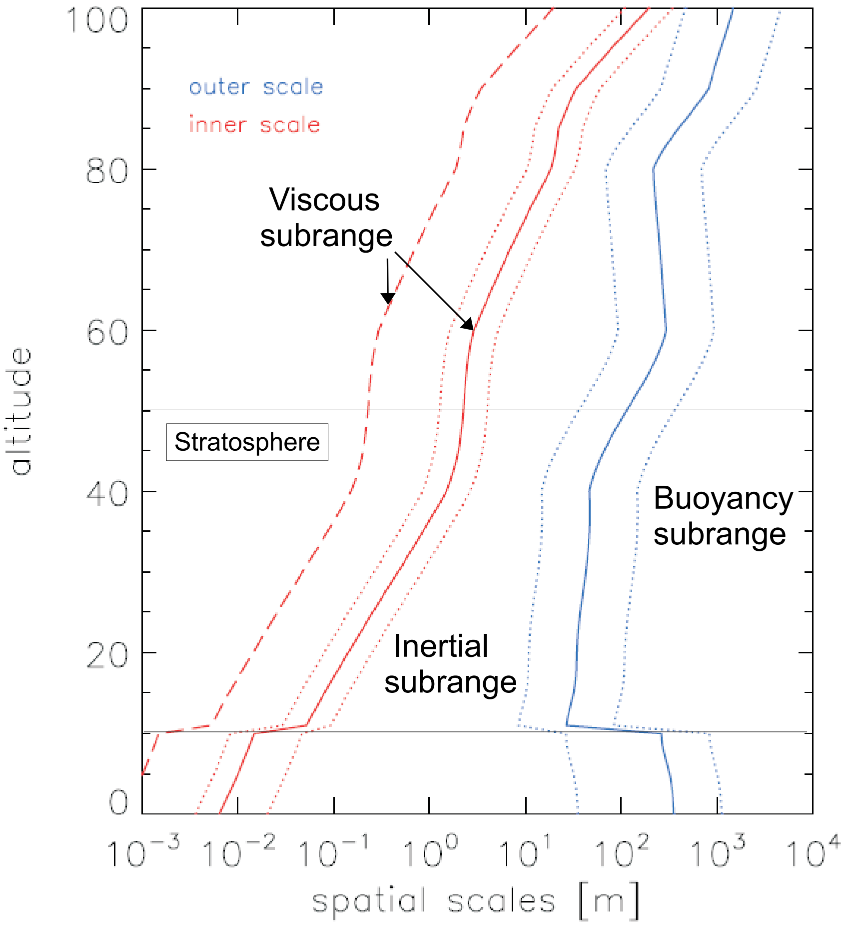

Figure 1.2: Length scales of importance for turbulence in the atmosphere. The dashed red line indicates Kolmogoroff microscale. Outer scale is represented by blue lines, inner scale by red lines. The scales were calculated as suggested by *Lübken et al.* [1993]. Prepared by Prof. Dr. F.-J. Lübken from IAP, Kühlungsborn.

The atmospheric turbulent fluctuations in the wind field mix layers of different temperatures, densities and trace gases content. And due to this they influence the transfer

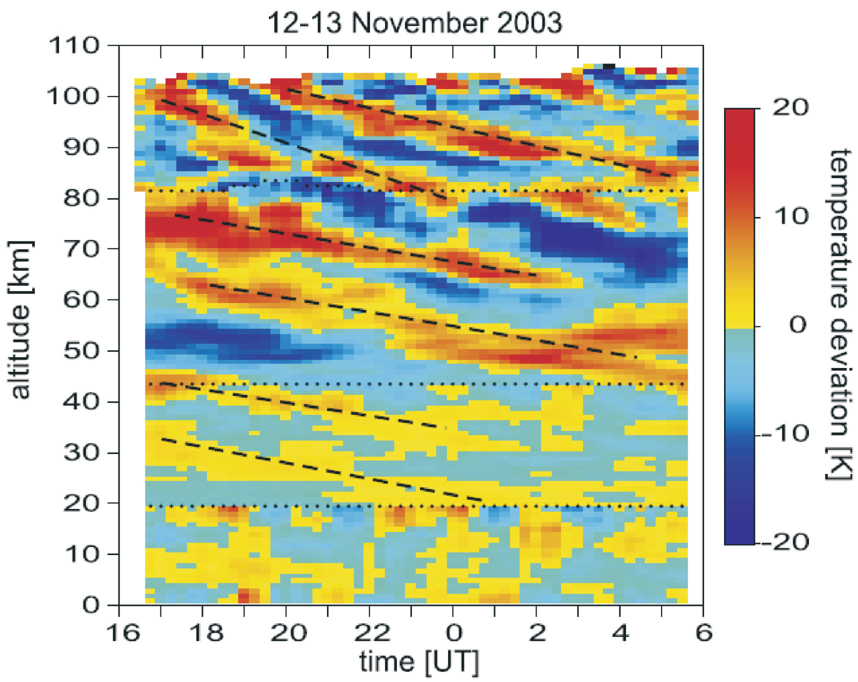

Figure 1.3: Gravity waves visible in temperature field. The measurements were carried out over Kühlungsborn (54°N) with lidar system during the night between 12th and 13th November 2003. The dashed lines indicate the phase propagation.

of heat, matter, and momentum between the different air masses, as well as the energy and momentum deposition.

The current progress of computational atmospheric dynamics is demonstrating the ability of numerical simulations to describe destabilizing processes associated with almost all of the structures observed in the atmosphere. The models however require basic information about the dynamics and composition of the atmosphere and should also be verified by observations. Nowadays, it is possible to accomplish the measurements of large and small scale atmospheric structures at nearly all altitudes. In the troposphere and the mesosphere remote sensing techniques are widely used. Radar enables exploration of the atmosphere at altitudes between 1 and approximately 16 km [*Fritts et al.*, 2003; *Serafimovich et al.*, 2005; *Kalapureddy et al.*, 2007] and because of relatively large electron densities above 60 km also in the mesosphere and the thermosphere [*Hocking*, 1996; *Latteck et al.*, 2005; *Engler et al.*, 2005]. In-situ techniques are applicable in the troposphere [*Barat et al.*, 1984; *Muschinski et al.*, 2001], stratosphere [*Lilly and Lester*, 1974; *Barat and Bertin*, 1983; *Dalaudier et al.*, 1989], mesosphere and lower thermosphere [*Lübken et al.*, 1992; *Strelnikov*, 2006].

The in-situ techniques base on measurements of turbulence effect on the spatial fluctuations of a tracer. These fluctuations are created by turbulent velocity fluctuations acting on a mean gradient of the tracer. The tracer has to be 'conservative', which means it should not change in time other than by turbulent motions. In addition, it should be 'passive', what means that it should not influence the turbulent flow. In the troposphere, the most used tracers are potential temperature and velocity fluctuations. The in-situ measurements in this layer are performed mostly from aircrafts and balloons. In the mesosphere, the turbulent tracers are relative neutral density fluctuations (created when an air parcel is elevated vertically by turbulent motions) and plasma density fluctuations [*Lübken et al.*, 1992; *Lübken and Lehmacher*, 1993]. In this case, the instruments are lifted to the mesosphere with rockets.

The measurements of small scales structures in the stratosphere are technically more difficult than in the other layers. It is caused by the restrictions in reaching to the altitudes above 10 - 12 km and by the static stability of this layer. *Hocking* [1985] writes that 'The region between 30 and 80 km is the most uncertain part of the graph [of the Fig. 1.2]'. It is due to the lack of appropriate research method, that would enable investigation of the flow with resolution equal 10^{-1} - 10^{-2} m.

As for now there are two methods that are able to provide much-needed high resolution information about the turbulence in the stratosphere: radar and in-situ methods like aircraft- or balloon-borne soundings. Unfortunately, radar and aircraft-borne soundings have restricted spatial coverage. Radar is able to provide measurements below the altitude of approximately 16 km. Above this height the refractive index of the atmosphere is too small to enable investigation of turbulence with this technique. The aircraft-borne soundings can be performed mostly only up to the tropopause, lower stratosphere region. This limitation arises from the technical construction of the aeroplanes, which require certain ambient conditions that are not available at higher altitudes.

The heights between 0 and 40 km can be reached by meteorological balloons. Balloon-borne atmospheric soundings have been used for more than one hundred years and provide inter alia density, wind and temperature data (cf. temperature profile in Figure 1.1). In the 1980's much research has been done on the possibilities of making stratospheric turbulence measurements from balloon-borne platforms [*Barat and Bertin*, 1983; *Barat et al.*, 1984; *Yamanaka et al.*, 1985]. As shown in Figure 1.2 stratospheric turbulence has scales smaller than a few centimeters and because of that the measurements of this phenomenon require very high spatial resolution. Technique available twenty years ago did not enable sampling of the data with a frequency fine enough for satisfactory wind field soundings.

Nowadays, the instruments, as well as the telemetry systems, give us the opportunity for much better resolution. A constant temperature anemometer (CTA), such as was used in our experiments, is a well known tool in the fluid dynamics (description in Chapter 3). It enables sampling the wind field with a frequency of 2 kHz resulting in a spatial resolution of 0.25 cm at balloon ascent rate of 5 m/s. Based on the table from Figure 1.2 it can be estimated that such a rate is enough for investigation of the turbulence.

During every balloon-borne experiment, the payload is influenced by the mean wind velocity due to the balloon motions. Thus, during a flight our anemometer measures a velocity relative to the payload, more precisely the vertical wind shear between the wind at the balloon level and the mostly deviant wind at the level of the gondola system. This permitted measurements of the horizontal wind with the CTA and due to this obtaining of the turbulence layers.

Figure 1.4 shows a typical method of turbulent field analysis. The plotted power spectral density (PSD) indicates the total average power distributed over some range of wavenumbers. The left chart indicates the wavenumbers that were reached in the atmospheric turbulence research of *Barat* [1982]. On the right-hand side one can find a result of test measurements made with the CTA. Both of those measurements were carried out at an altitude of approximately 27 km. Comparison of those two charts shows how much information can be gained with the new system.

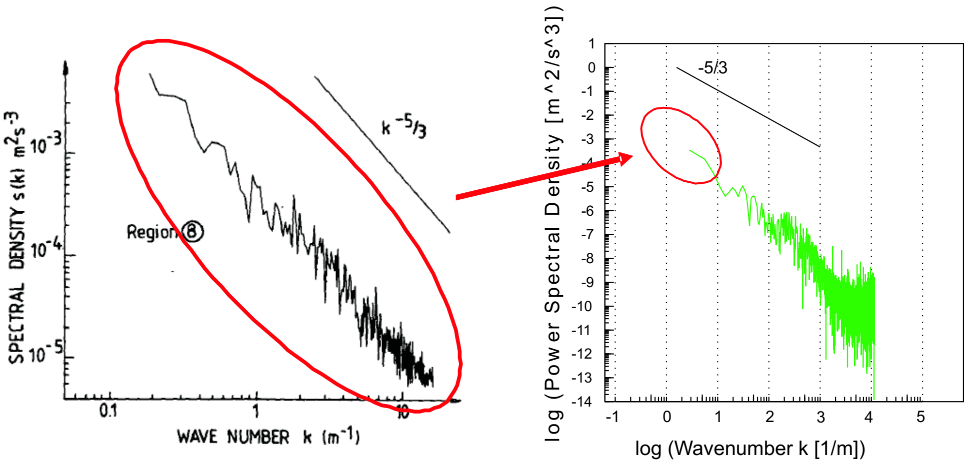

Figure 1.4: Power spectral density (PSD) of in-situ turbulence measurements. The left plot shows the analysis of data of wind shear [*Barat*, 1982], the right one PSD of data acquired with a DantecDynamics constant temperature anemometer 55P13. Both measurements were carried out at an altitude of approximately 27 km. The comparison of both plots shows, that the spatial resolution available with the new method is four orders of magnitudes better than the one available with the method used by *Barat* [1982] .

To summarize, the stratospheric turbulence is an important factor in understanding the stratosphere and through this also the whole atmosphere. Until now, there has been no method that would enable the measurement of stratospheric structures smaller than a few centimeters (see Figure 1.2). The new balloon-borne technique, that has been developed at the Leibniz Institute of Atmospheric Physics in Kühlungsborn, Germany, takes advantage of a high resolution that can be achieved with a constant temperature anemometer and yields satisfactory results.

The thesis includes description of the new method of stratospheric turbulence soundings. The fundamentals of atmospheric dynamics and motivation are presented in Chapter 1. Chapter 2 is devoted to turbulence as an atmospheric phenomenon. It includes basics of turbulence theory, characteristics of stratospheric turbulence and its measurements. The constant temperature anemometer, that was applied for the turbulence soundings is described in Chapter 3. In Chapter 4 other devices utilized at the experiment are shortly characterized. The software serving for compression of the binary data and providing the velocity data determination and analysis is presented in Chapter 5. The instrument was examined in laboratory and outdoor test. Descriptions and results of those experiments are shown in Chapter 6. Finally, Chapter 7 presents the preparation of the first test flight and data acquired during the sounding.

2 Turbulence in the atmosphere

Turbulence is a phenomenon present in all fluids, and it comprises a large class of motion with a complex, irregular and rather unpredictable nature [*Blackadar*, 1997]. At this time, there is no definition of turbulence that would completely describe this phenomenon. Instead, there is a widespread agreement, that has been provided by *Lumley and Panofsky* [1964] and concerns some of the turbulent flow attributes:

1. Turbulence is stochastic by nature. Although its equations are deterministic, they are nonlinear by nature and highly sensitive to small differences in the initial state. Because it is impossible to observe the initial state accurately enough, the turbulent movement cannot be treated in a deterministic way.

2. Small-scale turbulence is isotropic.

3. Any two marked particles that are free to move within a turbulent flow, will become increasingly distant from each other with time.

4. Vorticity is an essential attribute of turbulence.

5. Turbulence is dissipative. The energy of turbulence is transferred from large, well-organized eddies toward smaller eddies and eventually into molecular motions.

6. Turbulence occurs in a flow in case of large spatial dimensions and small viscosity (large Reynolds number).

Since most motions in the atmosphere are turbulent to some degree [*Blackadar*, 1997], turbulence plays a significant role in defining the evolution and structure of the atmosphere. Its influence on mixing and transport of momentum and energy at different altitudes has often been studied (e.g. *Lilly and Lester* [1974]; *Lübken* [1993]; *Alisse et al.* [2000]; *Strelnikov* [2006]). These efforts contributed greatly to our knowledge of the impact of turbulence in the dynamics of the atmosphere. However, due to inherited limitations or necessary assumptions, they have not fully characterized the relevant processes.

2.1 Basics of turbulence theory

Because of its non-linearity, rotation and the dimensionality of turbulence, there is no equation that would precisely describe this phenomenon. The quantitative approach to the study of turbulent fluids was begun by Sir Osborne Reynolds in his turbulence research in the latter part of the nineteenth century [*Reynolds*, 1895]. His study was restricted to incompressible fluids, later this restriction was removed by L. R. Richardson [*Richardson*, 1920]. Reynolds separated each of the velocity components U_i into two parts: a mean value, denoted by $\overline{U_i} = \langle U_i \rangle$ and a turbulent part, denoted by U_i', so that

$$U_i = \overline{U_i} + U_i' \tag{2.1}$$

Since the turbulent fluctuating velocities are of the order of a few percent of the mean velocity, the turbulence can be regarded as incompressible even if the fluid is not. The turbulent kinetic energy TKE per unit mass is then given by:

$$TKE = \frac{1}{2}\overline{U'^2} \tag{2.2}$$

with $\overline{U'^2} = \overline{U_x'^2 + U_y'^2 + U_z'^2}$. It plays a vital role in determining the atmospheric dynamics and coupling [*Kalapuereddy et al.*, 2007]. The TKE depends on TKE dissipation rate or eddy dissipation rate ε, which can be written as

$$\varepsilon = -\frac{d}{dt}\frac{1}{2}\overline{U'^2}, \tag{2.3}$$

and denotes a rate at which kinetic energy is transferred to heat. The ε parameter gives the turbulence in the velocity field and is one of the fundamental parameters used in determination of the turbulence characteristics. It represents the rate at which energy cascades to smaller eddy units. The energy is converted into heat due to the presence of a viscous force. As one can see in Eq. 2.3, the dissipation rate depends on temporal fluctuations in the velocity field. The dissipation takes place at the smallest scales in the flow (small sizes of eddies), because there the velocities are the largest. The amount of dissipating energy is determined however by the large, or energy-containing, scales in the flow [*Holmes et al.*, 1996].

Generally, turbulence can be characterized by a number of length scales: at least one for the energy-containing range, and one from the dissipative range. There may also be others, but they can be expressed in terms of the above mentioned scales. The complexity of the mathematical description of turbulence depends on the number of length scales that are necessary to describe the energy-containing range [*Gatski et al.*, 1996]. Turbulence in the stratosphere consists of more than one length scale because of its complicated production mechanisms. That makes it difficult to predict. Figure 2.1 shows the typical kinetic energy distribution in the turbulent stratospheric flow field. It shows how turbulent energy is distributed over the structures of different spatial scales. The ordinate represents the energy density, E. The upper abscissa corresponds to the spatial scale of a turbulent structure l, which is related to the wavenumber $k = l/2\pi$ (lower abscissa).

As shown at the beginning of the Chapter, the energy exchange between the mean flow and the turbulence is governed by the dynamics of the large eddies. Therefore, the energy enters the turbulence mainly at length scales which are comparable to the

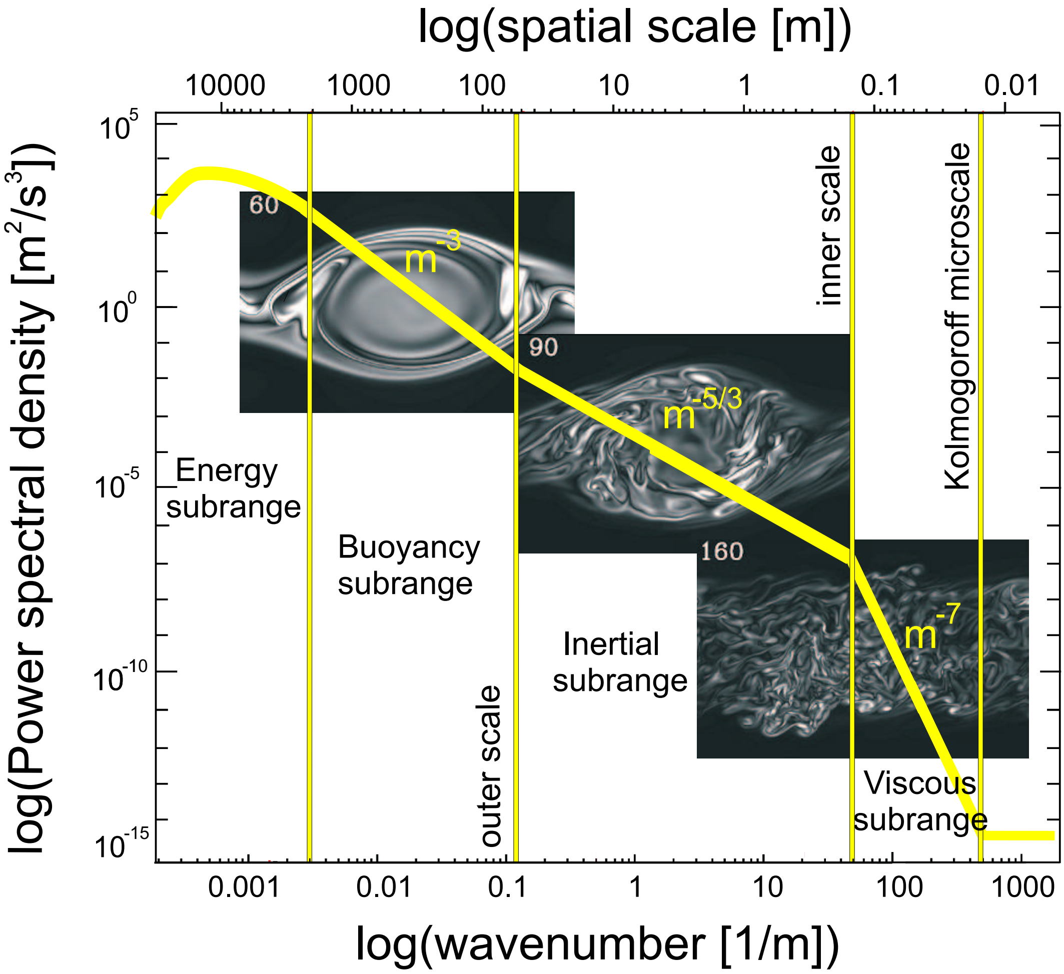

Figure 2.1: Energy spectrum of turbulence after *Strelnikov* [2006] with figures of turbulence of Reynolds number equal 60, 90 and 160. Based on *Fritts and Alexander* [2003].

sizes of the largest eddies occurring in the flow. In the spectrum from Figure 2.1, the left-most part, called the energy subrange represents the region with those scales. The acquired energy is transformed from large eddies to small eddies by a process of vortex stretching. This results in an energy cascade within the turbulent flow. The next part of the spectrum is the buoyancy subrange, since buoyancy forces are dominant. In this subrange the gravity waves are observed. The next two subranges are called the inertial subrange and the viscous subrange. In the inertial subrange the motion of the turbulent eddies is completely dominated by inertial forces and in the viscous subrange the energy is dissipated to heat by viscous forces.

A mathematical description of the last two subranges has been introduced by *Kolmogoroff* [1941]. He suggested that, as the energy was passed from one scale to another, it would lose detailed information about the mechanisms of energy production. If the number of steps in the cascade was sufficiently great, it could be presumed that all information would be lost. The small scales would only 'know' how much energy they were receiving and they might be expected to be isotropic [*Gatski et al.*, 1996]. That is why, although the large-scale motion is often highly non-isotropic, the fine-scale motion can be regarded as locally isotropic. The assumptions of isotropic and approximately homogeneous wind fluctuations for scales less than the largest eddies provide the base for the Kolmogoroff theory. A mathematical description of the inertial subrange was first derived by *Kolmogoroff* [1941] from dimensional reasoning and is well accepted to be $E(k) \propto k^{-5/3}$ for a one dimensional spectrum. The viscous subrange part has much steeper slope and can be described by $E(k) \propto k^{-7}$ [*Heisenberg*, 1948; *von Weizsäcker*, 1948]. It has to be emphasized, that although the introduced description is not strictly mathematical, it agrees reasonably well with experimental results.

2.2 The origin of turbulence in the free atmosphere

There are two processes believed to be dominant mechanisms for turbulence generation in the free atmosphere: breaking of gravity waves (GW) and Kelvin-Helmholtz (KH) instabilities, which can also accompany the breaking of gravity waves. The Kelvin-Helmholtz instability appears to play significant role at lower altitudes, in the tropopause and lower stratopause, where vertical wavelengths and vertical group velocities tend to be small. Gravity wave breaking becomes increasingly important at higher altitudes, where wavelengths and group velocities are larger. This process is a dominant source of turbulence in the higher stratosphere, mesosphere and lower thermosphere [*Fritts et al.*, 2003]. Both of those turbulence creation processes can occur only in a dynamically instable air layer, by a Richardson number $Ri < 1/4$ [*Fritts et al.*, 2003]. The Richardson number can be regarded as an indicator for a turbulence degree in a flow and is given by:

$$Ri = \frac{N^2}{[(\frac{\partial U_i}{\partial z})^2 + (\frac{\partial U_j}{\partial z})^2]} \tag{2.4}$$

where N is the Brunt-Väisälä frequency.

In the atmosphere, KH instabilities are most often associated with strong shears of mean wind or accompany low-frequency gravity waves, which have small vertical group velocities and slowly evolving amplitudes and shear [*Fritts et al.*, 2003]. Due to the friction force between two air masses with different speed, irregularities in the form of penetration of one layer into the other one develop. Arisen billows entrain the heavier fluid from below and lighter fluid from above and create alternating bands of positive and negative static stability. Further, the entrainment and overturning within the KH billow establish an approximately adiabatic mean thermal structure, from which secondary instabilities and turbulence arise.

Inertial gravity waves are transverse waves that can occur in any fluid stably stratified with density. They arise from restoring forces of gravity acting downwards and buoyancy acting upwards on vertical displacement fluid parcels (see Chapter 1.2). Internal gravity waves observed in the atmosphere have scales ranging from meters to kilometers and dominate fluctuations in the stratosphere. The most common sources of internal gravity waves are the winds blowing over topography and cumulus convective clouds. Other sources are: adjustment toward equilibrium of jets and of unsteady vertical flows and the sudden formation of patches by a dynamical instability [*Fritts and Alexander*, 2003]. During their propagation, gravity waves are able to transport momentum and energy many kilometers upward from the Earth's surface. At higher altitudes, the amplitudes of waves increase due to decrease of density, until they encounter their breaking level. There the amplitudes are so large, that the wave motion becomes irreversible and the waves deposit energy and momentum into mean flow. Such quasi-continuous gravity wave breaking generates drag and diffusion that strongly influence the global circulation and temperature patterns of the middle atmosphere. Turbulence arises when the flow is either dynamically (KH instability) or convectively unstable (potential temperature decreases with altitude) and the timescale for instability growth is sufficiently shorter than that describing the evolution of the wave field [*Fritts and Alexander*, 2003]. The transfer of momentum from the wave field to the mean flow associated with wave breaking involves not only local mixing of the density field but also a marked impact on the vertical variations of horizontal velocity [*Afanasyev and Peltier*, 2001].

In the stratosphere, the turbulence occurs mostly in layers of limited depth. The turbulence extent is determined by the scale of shear instability or wave breaking and therefore confided vertically by stratification. The turbulence is characterized by patchy high frequency fluctuations in the wind fields and long-lived energetic eddies with a vertical scale of a few tens to a few hundreds meters. The sizes of a single eddy are mostly less than few centimeters and its lifetime is not more than one minute (see Figure 1.2).

The knowledge of stratospheric turbulence is not only important in the process of understanding the atmospheric dynamics, but can also contribute to design risk definitions for aircrafts. The critical layer behavior in the lower stratosphere must be ascertained to enable the time and place prediction of appearance of so called *clear air turbulence* (CAT) layers. The clear air turbulence is frequently encountered around jet streams or sometimes near mountain ranges. It is impossible to detect either with the naked eye or with conventional radar. Because of that it is difficult to avoid. The aircrafts crossing the turbulent layer experience sudden unexpected accelerations or 'bumps', what creates hazard for the navigation, the planes construction and for the passengers. Nowadays, the soundings of those fluctuations are carried out mostly by aircraft-borne instruments [*Hicks et al.*, 1967; *Glover et al.*, 1969; *Stearns et al.*, 1981].

2.3 Methods of stratospheric turbulence measurements

A good way to estimate the turbulence activity is to measure the turbulent kinetic energy TKE or the TKE dissipation rate ε (see Chapter 2.1). There exist several methods that can be used to determine those parameters in the stratosphere. The in-situ methods include balloon- or aircraft-borne measurements of fluctuations, mostly of the wind field. The remote sensing investigations are mainly based on radar measurements.

Chapter 2.3.1 is an introduction to in-situ methods in the stratospheric turbulence soundings. It includes characteristics and examples of balloon-borne measurements, their advantages and related obstacles.

Chapter 2.3.2 introduces turbulence research with radar. It provides a short description of two measurements techniques and emphasis the one, that is used at Leibniz Institute of Atmospheric Physics (IAP) in Kühlungsborn, Germany. An example of wind measurements carried out with this method is included in Chapter 7.3.

2.3.1 In-situ methods

The in-situ measurements of stratospheric turbulence base generally on sounding of wind, temperature, pressure or humidity gradients and estimation of some key parameters of isotropic turbulence. Those parameters are mostly: root-mean-square of fluctuating velocity components

$$U'_{r.m.s} = \sqrt{U'^2} \tag{2.5}$$

and dissipation rate of kinetic energy ε. The sounding systems are lifted to the defined altitudes with aircrafts or meteorological balloons. Since the aeroplanes reach only the lower regions of stratosphere, the balloon-borne methods are the only ones to measure the wind fluctuations in the mid-stratosphere. The first attempts at the balloon-borne stratospheric turbulence sounding were made more than 20 years ago. The works of *Barat* [1982], *Barat and Bertin* [1983] , *Yamanaka et al.* [1985] and *Dalaudier et al.* [1989] provided first pieces of information on the turbulent flow characteristics and its influence on the dynamics of the stratosphere. Moreover, they pointed the direction of further studies in this field.

Although, the soundings of atmosphere with meteorological balloons have more than one hundred years history, there are still many problems encumbering this method. One of the largest obstacles in the high-resolution in-situ measurements seems to be the telemetry and eventual data storage. The balloon track is hard to predict exactly and to follow, what strongly interferes the continuous data acquisition with directed telemetry systems. Another possibility is an application of storage devices on board. In this case a high-capacity storage device has to be used or compression procedure has to be compiled. Furthermore, the set-ups must be robust enough to deliver correct data under the stratospheric conditions and to stand the impact. Weight of the payload is also an important factor in the balloon-borne measurements and has to be taken under consideration during the constructions of the measuring instruments. In the turbulence soundings additionally the challenge of high spatial (i.e temporal) resolution occurs. All those factors make the preparation and accomplishing of the measurements from the balloon payloads very complicated. Moreover, solving those problems does not ensure the system recovery.

More information on the balloon-borne measurements of the stratospheric turbulence is given in Chapter 4. There one can find description of the telemetry and recovery system used during the first balloon-borne turbulence sounding at IAP, Kühlungsborn. Chapter 7 is devoted to the sounding, shows results of the measurements and provides an analysis of the acquired data.

2.3.2 Remote sensing

The largest advantage of radar is its capability to record continuously and uninterrupted for long periods of time (even 24 hours per day). The basic principle of radar is transmission and reception of high energy pulses. The recorded echoes provide information on magnitude, phase and time interval between pulse emission and return. Through those, the object polarization and Doppler frequency can be obtained. Radar offers potential to study long-term variability of atmospheric turbulence up to 16 km. In the lower stratosphere radar is able to provide the maximal vertical resolution of 150 m. The horizontal resolution of radar with a beamwidth of 7 ° is approximately 1.2 km at 10 km altitude, at 15 km it is equal about 1.8 km. Thus, the quality of radar turbulence measurements is significantly lower than that of in-situ methods.

The radar ranging height depends on the gradients of atmospheric variables and the electron density changing with the altitude. In the stratosphere, gradients of those variables are too small to provide sufficient vertical resolution. The measurement are possible only up to about 16 km. Two different radar techniques are used in the research in the troposphere and lower stratosphere:

- method using measurements base on the spectral width, such as from Doppler beam swinging analysis.
- method using measurements of the absolute signal power determined using calibrated radar,

The first method is utilized at IAP, Kühlungsborn. In this case, the energy dissipation rate ε is obtained from the Doppler spectral width parameter determined by radar observations. The observed spectral width in velocity units σ_{obs} of a received radar signal is given by:

$$\sigma_{obs} = \frac{\lambda}{2} f_{(1/2)obs}, \tag{2.6}$$

where $f_{(1/2)obs}$ is the half-power half-width of the Doppler spectrum in the frequency domain and λ the radar wavelength [*Hocking*, 1996]. If the beamwidth of the transmitting radar is smaller than 10°, only turbulent fluctuations in the atmosphere cause the spectral broadening and the contribution of the background wind can be neglected [*Engler et al.*, 2005]. The spectral width from a radar beam is influenced by the turbulent fluctuation σ_{turb} and by broadening effects due to wind shear. The following equation displays the contributing parts which determine the observed spectral width:

$$\sigma^2{}_{obs} = \sigma^2{}_{beam} + \sigma^2{}_{shear} + \sigma^2{}_{turb} = \sigma^2{}_{corr} + \sigma^2{}_{turb} \tag{2.7}$$

The correction of beam and shear broadening is combined in the term $\sigma^2{}_{corr}$. After separating the turbulent contribution, it can be converted into *root-mean-square fluctuating* *velocity*:

$$U'^2{}_{r.m.s} = \frac{\sigma^2{}_{turb}}{2ln2} \tag{2.8}$$

The fluctuations U' in the wind field are measured at scales of $\lambda/2$. The radar used in IAP is able to reach scales of about 2.8 m. In this case the $-5/3$ slope of the energy spectrum of the turbulence (Figure 2.1) cannot be measured. However, it can be assumed that the $U'^2{}_{r.m.s}$ is caused by small scale turbulence and short period gravity waves. Due to this, the turbulent kinetic energy dissipation rate ε_{turb} can be derived as:

$$\varepsilon_{turb} = 0.47(\frac{\sigma_{turb}}{\sqrt{2ln2}})^2 N(\frac{1}{c_f})^{2/3} \tag{2.9}$$

where c_f is a correction term due to influence of high frequency gravity waves on the turbulent fluctuation [*Hocking*, 1996].

The absolute signal power method involves determining the backscattered power received with a radar and then using radar characteristics such as the beam width, wavelength, transmitter power, antenna gain and antenna effective area to determine an effective turbulence structure constant C_n^2. This structure function can then be related to the energy dissipation rate ε through a relation considering the conditions within the defined volume [*Hocking*, 1996]. Although the relations are relatively simple, there are complications involved in evaluation of the turbulence strength by this method. Most of them result from assumptions that are hardly fulfilled in the atmosphere. For example, in this method the radar volume is assumed to be completely filled with turbulence. In the real atmosphere however, only a fraction of the volume is filled. In order to make a meaningful estimate of the energy dissipation rate ε it is necessary to determine this fraction. This can be determined only in an approximate calculation and can still lead to large errors in ε.

3 Constant Temperature Anemometry

The constant temperature is one of the modes of hot-wire anemometer (HWA) operation. The hot-wire anemometry has been used for many years in fluid mechanics as a relatively cheap and effective method of measuring the rapid fluctuations in turbulent flows. The sensors are thin metallic elements heated by an electric current (Joule effect) and cooled by the incident flow, which acts by virtue of its mass flux and its temperature. From the temperature, resistance or current attained by the sensor, it is possible to obtain the information on the flow [*Bellot*, 1976]. High temporal (up to hundred kHz) and spatial resolution, which enables eddies' investigation down to 1 mm or less, as well as the high temperature tolerance and instantaneous provision of velocity information make the hot-wire anemometer one of the most appropriate tools in measurements of small-scale turbulence.

Although, the hot-wire anemometer (HWA) seems to be a proper instrument for the atmospheric turbulence soundings, up to now it has been mostly utilized only in the Earth's boundary layer. Several measurements have been also carried out in the troposphere and the tropopause region. In those cases soundings were performed from aircraft-borne platforms [*Merceret*, 1976; *Siebert et al.*, 2005] or the HWA were deployed with kite/blimp systems [*Muschinski et al.*, 2001]. In the new developed method described in this thesis, HWA system was placed in a payload of a balloon. That allowed lifting the HWA up to an altitude of 35 km and provided information on the turbulence in the lower and mid stratosphere.

3.1 Basic principles of hot-wire anemometry

Fundamentally, the hot-wire anemometry makes use of the principle of heat loss from a heated surface being dependent on the flow conditions passing over it [*Payne*, 2001]. The sensing element in our case is a tungsten wire, that is heated by an electric current to a temperature of approximately 250 °C. The heat is transferred from the wire mainly through convection. This heat loss is strongly dependent on the excess temperature of the wire, the physical properties of the sensing element and on its geometrical configuration. By hot-wire anemometry the sizes of the sensing element are small, so that the Reynolds number of the flow is very low and the flow pattern over the sensor can be assumed to be symmetrical and quasi-steady. Due to the statement of the flow continuity, the mean free path of the particles is very much less than the diameter of the wire and conventional heat transfer theories are applicable [*Steinback and Nagabushana*, 1996]. Furthermore, the length of the sensor is much greater than its diameter. Hence, it may be assumed that the loss by conduction through the ends is negligible and the relation for the heat transfer from an infinite cylinder can be applied.

The convective heat transfer rate, $\dot{Q}$ for a flow is generally given by an expression

$$\dot{Q} = hA_s\Theta, \tag{3.1}$$

where h is a convective heat transfer coefficient, A_s is the surface area of the body gaining/losing energy, $\Theta = T_w - T_a$ is the difference between the temperature of the surface T_w and the temperature of the fluid flowing over the body T_a. For a cylinder in a cross-flow, the solution for the convective heat transfer coefficient leads to the following expression for the rate:

$$\dot{Q} = [A + B(\rho U)^n]\Theta, \tag{3.2}$$

The values A and B are constants, valid for given temperatures T_w, T_a and given wire. Physically these constants include the effects of quantities like thermal conductivity and size of the sensor. They can be determined by calibration of the sensor. The exponent n is strongly dependent on the type and Reynolds number of the sensor as well as on the flow characteristics. The ρU represents the mass flux.

Hot-wire anemometers can be operated in one of two modes, constant current (CC) mode and constant temperature (CT) mode. In our experiments the second one was used. The major advantage of maintaining the hot-wire at a constant operational temperature and thereby at a constant resistance is that the thermal inertia of the sensing element is automatically adjusted when the flow conditions vary. The electronic circuit of chosen CTA is shown schematically in Figure 3.1. The mode of operation is achieved by incorporating a feedback differential amplifier into the hot-wire anemometer circuit. Such set-up obtains a rapid variation in the heating current and compensates for instantaneous changes in the flow velocity [*Bruun*, 1995].

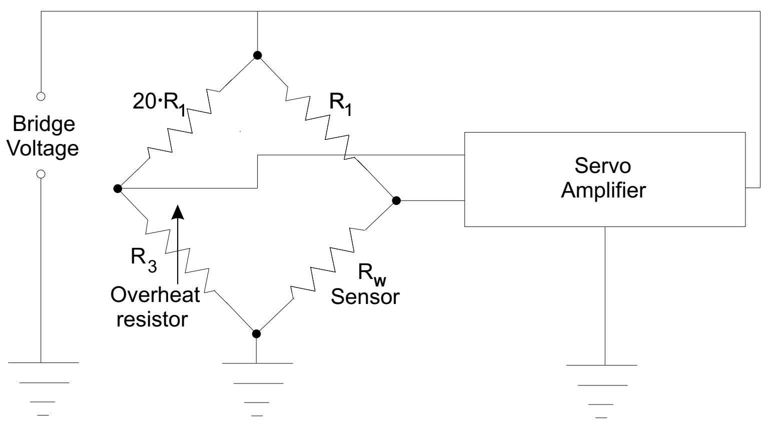

Figure 3.1: Constant Temperature Anemometer principle diagram.

The hot-wire forms a part of a Wheatstone bridge, such that the wire resistance is kept constant over the bandwidth of the feedback loop. The sensor is the largest electrical resistance in the probe. Thus, the electrical power dissipation $\dot{Q}_{elec}$, when the sensor is heated, is given by:

$$\dot{Q}_{elec} = I^2 R_w. \tag{3.3}$$

I corresponds to the current passing through the sensor and R_w to the sensor resistance by the temperature T_w. For steady-state operation, the rate of electric power dissipation equals the rate of convective heat transfer. That is:

$$I^2 R_w = [A + B(\rho U)^n]\Theta. \tag{3.4}$$

Using Ohm's law on the circuit shown in the Figure 3.1,

$$E^2 R_w = (R_1 + R_w)^2 [A + B(\rho U)^n]\Theta, \tag{3.5}$$

where E is electromotive force, R_1 is one of two non-temperature dependent resistors. Because the used hot-wire anemometers work in the constant temperature mode, R_w and Θ are held constant [*Jagoda et al.*, 2005]. This fact leads to relation:

$$E^2 \sim U^n \tag{3.6}$$

with an assumption that the fluid is incompressible ($\rho = const.$) The electrical resistance of the wire's material increases linearly with temperature, so the resistance can be described as:

$$\frac{R_w - R_0}{R_0} = \alpha(T_w - T_0) \tag{3.7}$$

where R_0 is the value of the resistance at a reference temperature T_0 and α is the temperature coefficient of resistance [*Jagoda et al.*, 2005]. In case of increased current through R_w, more heat is produced. If it is not convected away at a sufficiently high rate, T_w will increase, until Θ becomes large enough for the convection rate to balance the heating rate.

The Wheatstone bridge is essentially balanced, when

$$R_w = \frac{R_3 \cdot R_1}{20 \cdot R_1} \tag{3.8}$$

In case of increase of the heat transfer, the wire's temperature T_w will decrease. If due to this decrease, the R_w becomes lower than $\frac{R_3}{20}$, then an error voltage at the input of the servo-amplifier will be introduced. After considerable amplification, the signal from the amplifier increases the bridge voltage and hence also the current through the sensor. At the end the sensor is heated and the bridge balance is restored, the temperature T_w and resistance R_w are increased. In this way the probe temperature is kept essentially constant and the effect of the thermal inertia of the probe is minimized.

The combination of the sensor's low thermal inertia and the high gain of the servo loop amplifier (see Figure 3.1) provides a very fast response to fluctuations in the flow. In practice, the cut-off frequency of hot-wire probes exceeds 10 kHz and for special applications over 1 MHz can be reached. Since we want to measure turbulence of spatial

Bridge ratio	1:20
Bridge top resistance	20Ω
Maximum probe current	230 mA
Equivalent input drift	0.2 $\mu V/°C$
Equivalent input noise	80 nV pp 0.1-10 Hz, 3 $nV/\sqrt{Hz}$ above 1 kHz
Operating resistance	4-20 Ω
Probe cable	3 m (1 m on probe support and 2 m BNC-BNC cable)
Probe connection	BNC connector
Dimensions	3x6x11 cm
Weight	0.25 kg

Table 3.1: Specifications of DantecDynamics constat temperature anemometer.

scales of a few centimeters to a few millimeters (Figure 1.2), the response frequency sufficient for our research was obtained on 2 kHz. That gives sufficient spatial resolution of 0.25 cm at balloon ascent of 5 m/s and at the same time enables data transfer, transmission through telemetry system and relatively fast handling. Furthermore, the response time of the CTA during measurements in the stratosphere changes due to the low density. This effect is not well known, but it may strongly influence the data and is difficult to be defined and characterized at very high frequency responses. The specification of the CTA is presented in 3.1.

3.2 Turbulence measurements with CTA

Hot-wire anemometers are mostly used in turbulent flows with velocity fluctuations U' small compared to the mean velocity $\overline{U}$. A data acquisition system samples the voltage and records instantaneous voltages, proportional to the instantaneous current through the wire. The time average of the fluctuating component $\overline{U'}$ is zero since the fluctuations are random and the U' at any instant is as likely to be positive as negative. However, the variance $\overline{U'^2}$ is not zero and gives a measure of the intensity of fluctuations (see Chapter 2.1).

3.3 Hardware

A hot-wire system for the measurement of high frequency flow fluctuations consists of an anemometer bridge and a probe mounted on a support. In general, the used systems consist of the following:

- 5 μm wire
- prongs carrying the wire and leading current to it

- probe body carrying the prongs
- probe cable
- anemometer bridge containing Wheatstone's bridge and servo amplifier

Figure 3.2 presents a 55P13 probe with a probe support of a constant temperature anemometer used during our experiments. The sensor is a thin platinum-plated tungsten wire. The hot-wire material is chosen because of its high temperature coefficient of resistance, high specific resistance, high mechanical strength and ability to operate at high temperatures. Those properties provide good flow sensitivity and highest possible strength with a minimum of thermal inertia. The wire is spotwelded to needle-shaped, right-angled prongs which are made of stainless steel (Figure 3.2). During the ascent of the balloon-borne platform, the wire experiences strong vertical wind. Due to the vertical alignment of the wire, the influence of this vertical movement of the platform on the measurements is minimal. Thanks to this, horizontal flow due to the wind shear affects the wire stronger than the artificial vertical flow generated by the ascending balloon. The prongs of the probe are embedded in a probe body. This serves as the electrical connection between probe and probe's cable and provide a mechanical mount for the probe at the same time. The probe cable has a length of 2 m. The bridge electronics is adjusted to the impedance caused by the cable of such length. The anemometer bridge delivers power to operate the probe and provides a low-pass filtering. Furthermore, it connects the setup with an external A/D converter board.

In the turbulence investigation presented in this thesis two DantecDynamics MiniCTA systems were used, one with 55P13 probe and another with 55P03 probe. Both of the implemented types are made of the same material, but the ends of the 55P03 wire are additionally coated with gold to reduce the amount of heat dissipated by the prongs. The chosen 55P13 and 55P03 probes maintain wires of a diameter of 5 μm and a length of 1.25 mm. 55P03, because of its additional prongs' coating, has an overall length of 3 mm (Figure 3.3). Such small wire sizes give minimal disturbance of the flow and suitable spatial resolution, which is required by the turbulence measurements.

Comparison of those two probes in the Earth's boundary layer is included in Chapter 6.3. Additionally, the 55P13 probe was calibrated (Chapter 6.1.1) and investigated due to contamination effect (Chapter 6.1.2), changing sensor yaw and pitch orientation in a flow (Chapter 6.1.3) and changing pressure (Chapter 6.2). The 55P03 probe was firstly chosen only as an alternative to the 55P13 probe. That's why, except the necessary calibration (Chapter 6.1.1), it was tested only in the comparison experiment with the 55P13 probe (Chapter 6.3).

3.4 Bridge adjustment and calibration

Two procedures are necessary before any experiment with the constant temperature anemometer, namely *overheat ratio* adjustment and probe calibration. The overheat

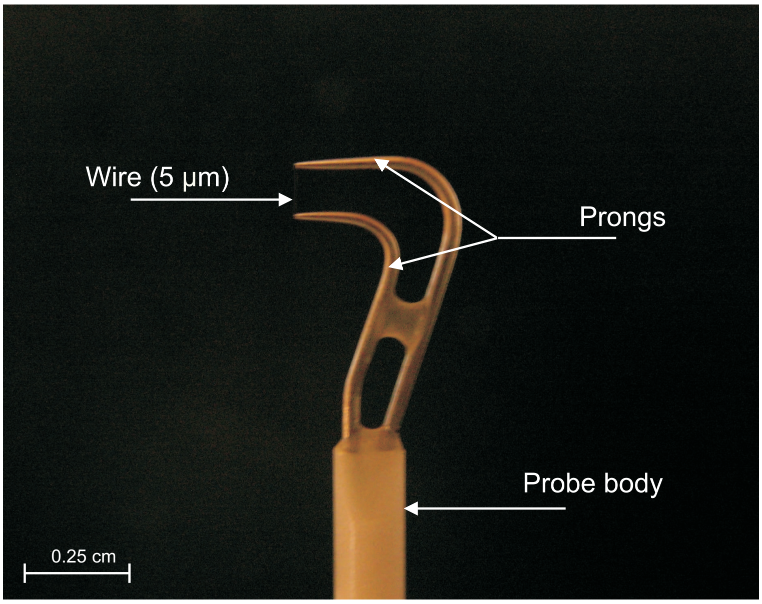

Figure 3.2: Picture of hot-wire probe 55P13.

ratio is the resistance ratio introduced in Eq. 3.7 and can also be written as:

$$\frac{R_w - R_0}{R_0} = a. \tag{3.9}$$

Its adjustment is essential, since it determines the working temperature of the sensor. The ratio a can be used for calculation of the temperature difference $T_w - T_0$, which is also called the *over temperature*:

$$T_w - T_0 = \frac{a}{\alpha}. \tag{3.10}$$

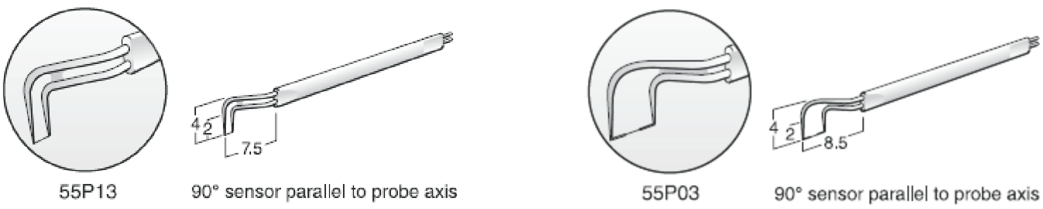

Figure 3.3: Dantec Dynamics 55P13 and 55P03 probes. Schemas from *DantecDynamics* [2007].

This over temperature provides the information about the temperature above the ambient temperature T_0, which is necessary to control the wire's current. To simplify the procedure of adjustment of overheat resistance ratio a, DantecDynamics provides a spreadsheet that calculates the binary code for the overheat resistance in the MiniCTA anemometer. The calculation bases on input of the wanted overheat ratio and ambient temperature together with the probe, support and cable resistance. a provided by those calculation and recommended for air is equal 0.8, the over temperature of the chosen probes is then approximately 220 °C.

Unfortunately, in our application the ambient temperature is varying from set-up to calibration and during the experiment. There are two ways of using the overheat adjustment in this case. In the first one the overheat is adjusted only once and left unchanged during the calibration and data acquisition. The ambient temperature is measured during the procedures and used to correct the anemometer voltages before conversion (see Chapter 3.5 and 7) [*Jørgensen*, 2002]. In the second way the probe resistance is measured, and the overheat is readjusted before the calibration and before each data acquisition. The overheat ratio is then the same in all situations and the temperature influence is minimized. The second method seems to be more accurate. However, in case of measurements in stratosphere due to the significant and fast changes of the temperature, only the first method is applicable.

Since the ratio between the voltage and the velocity is non-linear and heavily dependent upon the individual hot-wire, the feedback circuit must be calibrated for each hot-wire to resolve the dependance. The standard technique for calibrating of the hot-wire is to measure the anemometer bridge voltage response as a function of known mean flow velocity U. This mean flow response is assumed to obey some variation of the King's law (Equation 3.11) response curve for flow over a cylinder and the graph of E vs U is differentiated to obtain dE/dU [*Kirchhoff and Safarik*, 1974]. The King's law is given by:

$$E^2 = A + B \cdot U^n, \tag{3.11}$$

where $n = 0.45$ is a good start value for wire probes [*Jørgensen*, 2002]. However, because of the low accuracy of this kind of curve fits, in our research the response of the anemometer bridge voltage has been also expanded as a least square fit with a 4^{th} order polynomial.

$$U = C_0 + C_1 E_{corr} + C_2 E_{corr}^2 + C_3 E_{corr}^3 + C_4 E_{corr}^4 \tag{3.12}$$

The calibration gives an $E-U$ transfer dependence. This one plotted as $U(E_{corr})$ curve provides C_0 to C_4 constants for a given sensor, operating at a given value of resistance, in a flow of a constant temperature, density, and viscosity. Thus, if measurements take place in other fluids or under other conditions as the calibration procedure, corrections of voltage E due to those variables are necessary. That is why in Eq. 3.12 E_{corr} appears, instead of E. In the next chapter significance as well as methods of the data correction are described.

3.5 Temperature and density effect

After data acquisition some corrections of the measured voltage E are necessary. Since the heat transfer is directly proportional to the temperature difference between the sensor and the fluid, ambient temperature variations are one of the most important error sources in the measurements with the hot-wire anemometers. For a wire probe operated under typical laboratory conditions, the systematic error in measured velocity is approximately 2 % per 1°C change in temperature [*Jørgensen*, 2002]. Calibration plots in form $E = f(U)_{T_{const}}$ or $E = f(T_a)_{U_{const}}$ have been investigated in many publications. Figure 3.4 shows the calibration curves resolved for different ambient temperatures. Figure 3.5 presents response of the CTA on wind speed equal 1 m/s and 2 m/s at various temperatures. The temperature changes between 10 and 80 °C. During measurements at given wind velocity, the increase in the temperature causes decrease in the acquired voltage. The voltage error due to change in the temperature is equal 0.003 V for 1 °C. In the atmosphere temperatures differ significantly with altitude and a correction of the measured voltages is essential. DantecDynamics provides a formula that includes the temperature effects on acquired data. The expression requires the temperature acquisition along with the CTA signal.

$$E_{corr} = (\frac{T_w - T_0}{T_w - T_a})^{0.5} E \tag{3.13}$$

where E is acquired voltage, $T_w = \alpha/a_0 + T_0$ sensor hot temperature. T_0 is ambient reference temperature during sensor calibration and T_a is ambient temperature during data acquisition.

The second important factor for measurements at different altitudes is ambient pressure. It significantly changes the density and the mean free path of particles in the fluid. Normally, this problem is not noticed or simply avoided in hot-wire research. However, in the stratosphere the decreasing pressure has a crucial effect on the observed voltages (see Chapter 7). In Chapter 6.2 one can find description and results of tests in a vacuum chamber that devote to this problem.

Also contamination and humidity have an influence on the hot-wire voltage output. Due to the contamination, the heat transfer is reduced. To avoid problems caused by this factor, the sensor has to be calibrated shortly before the experiment. The importance of this procedure is shown in Chapter 6.1. If the sensor response drifts significantly, it may be necessary to clean the sensor [*Jørgensen*, 2002]. Also the water vapor amount changes with height in the atmosphere and should be considered as a possible source of errors in voltage measurements. However, effects due to temperature, density and contamination seem to have greater impact on the voltage-velocity dependance [*Jørgensen*, 2002].

During our flight experiment with the CTA, the data needed for the necessary corrections were acquired with a radiosonde. In Chapter 4.1 one can find a description of this device and precise information on its role in our experiment. The next chapter presents also another parts of the balloon-borne turbulence sounding instrument: a telemetry (Chapter 4.2) and a recovery (Chapter 4.3) system.

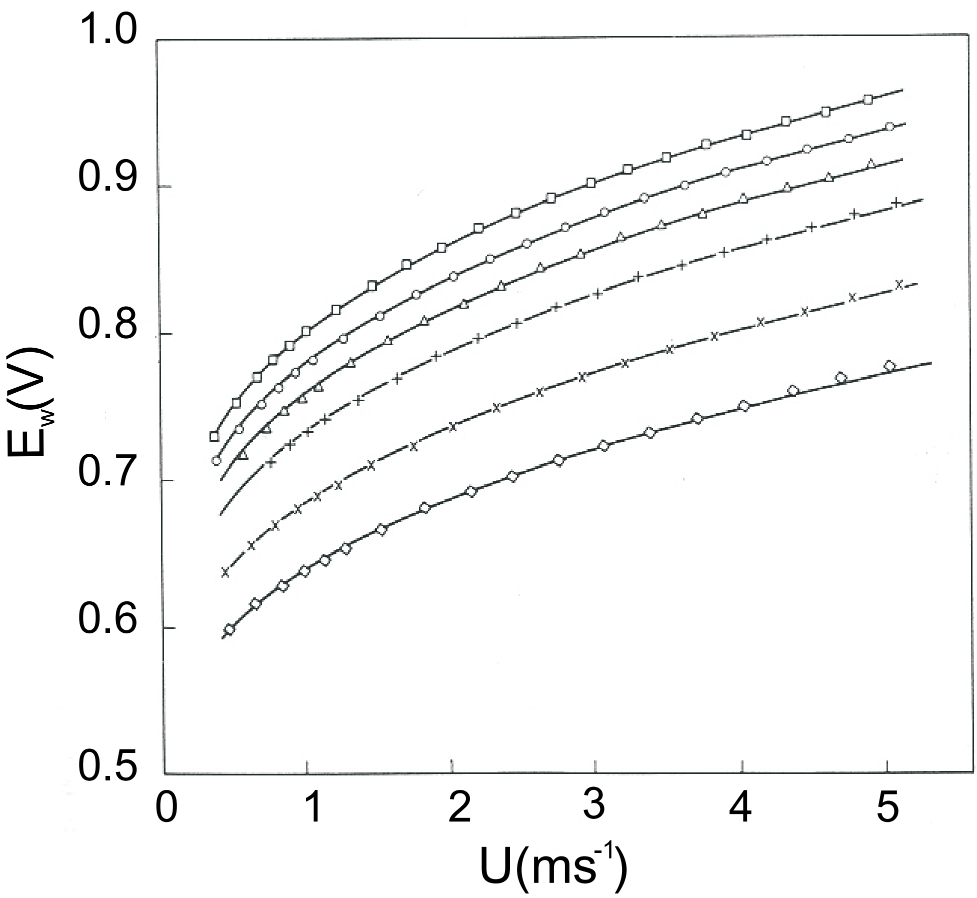

Figure 3.4: The dependence of the constant temperature hot-wire voltage E_w on the air velocity U, for the following ambient temperatures: T_a:(□)10°C, (O) 20°C, (△) 30°C, (+) 40°C, (X) 60°C , (◇) 80°C. $T_w = 200°C$. From [*Bruun*, 1995].

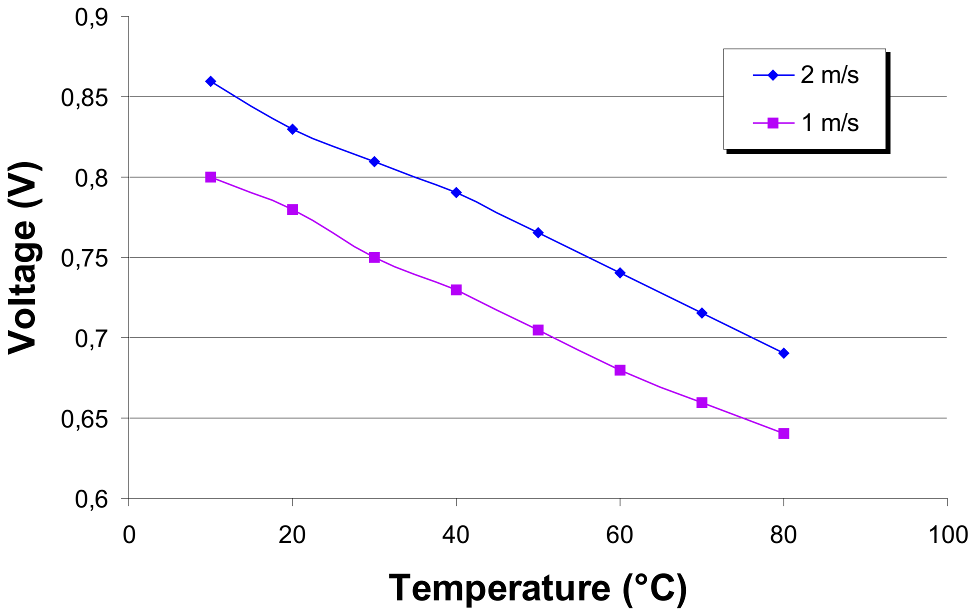

Figure 3.5: Response of CTA on wind equal 1 m/s and 2 m/s at various ambient temperatures. The violet line corresponds to wind equal 1 m/s, the blue one to 2 m/s.

4 Supporting instrumentation

Except the DantecDynamics MiniCTA system, our instrument for balloon-borne turbulence sounding in the stratosphere consists of:

- radiosonde
- telemetry system
- recovery system with a time relay
- 12 V battery providing energy supply for the telemetry and for the CTA

All the devices are able to work under stratospheric conditions and can operate for several hours onboard a platform as an independent payload.

4.1 Radiosonde system

The radiosonde system consists of a balloon-borne radiosonde, receiving and tracking equipment, and computer systems for data processing (see Figure 4.1). The radiosonde is a balloon-borne instrument used for simultaneous measurements and transmission of meteorological data while ascending up to 35 km height through the atmosphere. This device consists of sensors for the measurement of pressure, temperature, and relative humidity. The sensors' information is transmitted in a predetermined sequence to the ground receiving station. There, that information is processed at some fixed time interval. The wind information is processed by tracking the balloon's movement from a GPS signal. The radiosonde observations of the atmosphere describe the vertical profile of temperature, humidity, and wind direction and speed as a function of pressure and geometric height from the surface to the altitude where the sounding is terminated. This observations allow determining other atmospheric parameters like Richardson number (Eq. 2.4), vertical gradient of the potential temperature or the Brunt-Väisälä frequency (Eq. 1.4).

Wind profiles from radiosondes are derived from tracking the displacement of the balloon from the launch site as a function of time. The radiosonde is tracked using a reception of navigational GPS signals by an antenna on the radiosonde (see Figure 4.1). Those GPS signals allow a temporal resolution of a few seconds. However, due to rotation of the radiosondes in a pendulum under the balloon, the winds have to be filtered. It influences the temporal resolution. To avoid contamination of the radiosonde measurements, a suspension length between the radiosonde and the balloon of at least 20 m is necessary [*Wright*, 1997].

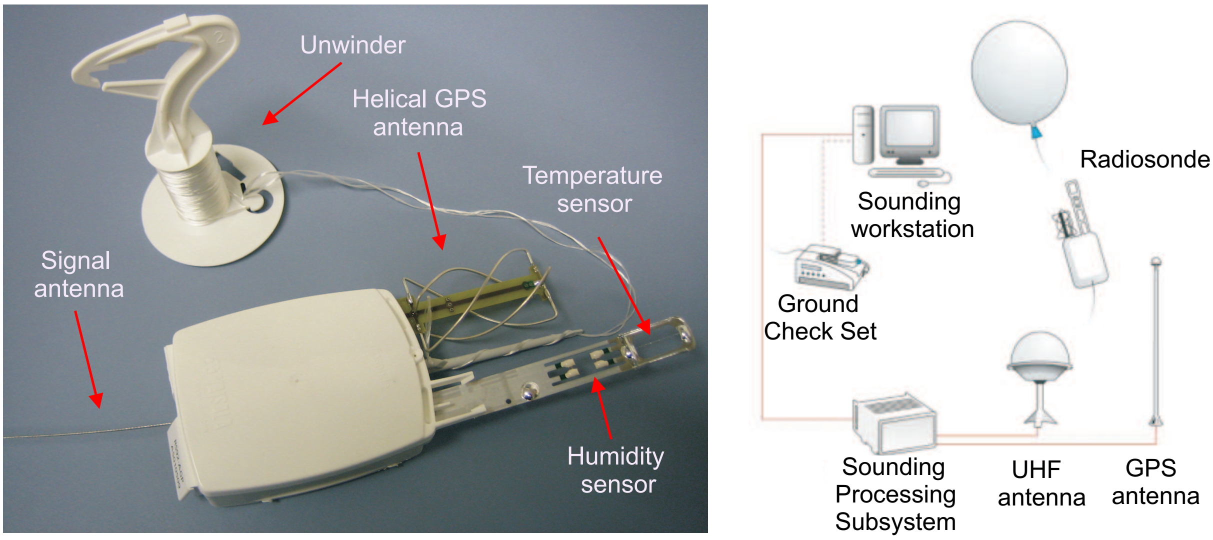

Figure 4.1: The DigiCora®III Sounding System MW31 developed by Vaisala.

The radiosonde system used during the flight experiment described in Chapter 7 is a DigiCora®III Sounding System MW31 developed by Vaisala. In Figure 4.1 one can see a photograph of the balloon-borne RS92 Vaisala radiosonde and a sketch of the radiosonde system. The radiosonde operates in 400 MHz frequency band and provides raw data in every 0.5 second and edited data in every 2 seconds. That, by ascent rate of 5 m/s gives spatial resolution of 10 m. The temperature and the pressure profiles provided by the radiosonde during sounding enable correction of the CTA data. Furthermore, the GPS data provide information on the payload position. Unfortunately, regular DigiCora®III online output is encoded binary and can not be used simultaneously with other software. To allow automatical steering of telemetry antenna (Chapter 4.2) an additional output was created. The payload position is written in a output ASCII file and updated once per 5 seconds. That provides information necessary for telemetry system for steering of the on-ground antenna and thus receiving of the data from the CTA.

4.2 Telemetry

The telemetry system was developed by Reimesch Kommunikationssysteme based on special requirements of our application. It consists of four main parts:

- modem recording, A/D converting, compressing, sending and saving the CTA data
- transmitting antenna attached to the modem
- on-ground receiving antenna
- on-ground antenna control unit

The telemetry was built after specification of IAP. First tests and design corrections have been part of this work.

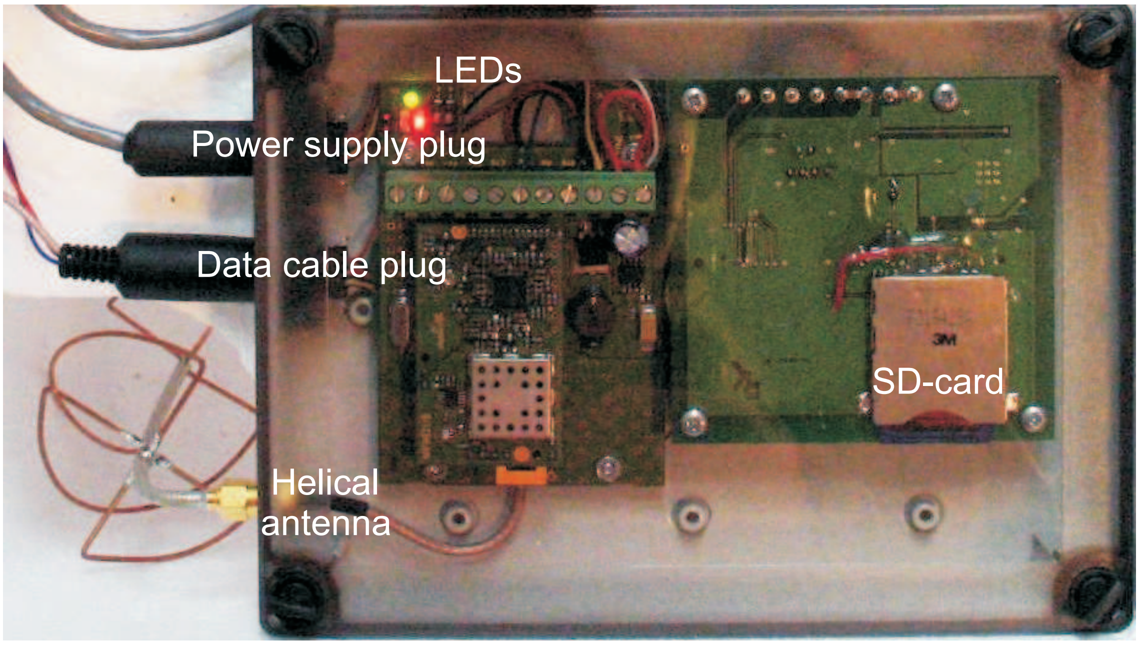

Figure 4.2: Telemetry modem.

4.2.1 Modem and transmitting antenna

The modem is an instrument, which provides 5 V power supply to the CTA and encloses A/D converter board. It enables compression of the data, sends the data to a transmitting antenna and saves it simultaneously to an 128 MByte SD-card. The compression procedure is described in Chapter 5. In Figure 4.2 one can see a picture of the modem.

Reimesch Kommunikationssysteme supplied a helical transmitting antenna to the modem. A cone of the helical antenna significantly determines direction, in which the antenna transmits the signal. During a flight the cone of the antenna would be placed mostly vertically. Considering the fact that the balloon trajectory is never vertical, we decided to change the type of the antenna. A new dipole antenna with a roughly spherical characteristics was built in IAP by Jörg Trautner. To compare those two antenna types, two experiments were carried out. In the first one, two Reimesch modems with different antennas were placed on a roof (80 m high) of a building distant 25 km from the receiving antenna at the IAP. In the second one, the modems (one after another) were transported with a car to a defined point, distant 50 km from the IAP. In both experiments, the signal from the helical antenna could not be received continuously. Many data gaps occurred in comparison to the tests with the dipole antenna. That means, that the dipole antenna is more suitable for the stratospheric measurements. It has a lower gain, but its radiation pattern is wider than in the case of the helical antenna.

4.2.2 Receiving antenna

The on-ground receiving antenna is placed on the roof of the IAP main building. It consists of four single helical antennas set in form of a square with a 72 cm long side. A characterization of the antenna is shown in Figure 4.3. It works in an axial (or endfire) mode and has a gain of 19.18 dBi. The angular range of the antenna pattern in which at least half of the maximum power is still emitted is described as a beamwidth. Bordering points of this major lobe are therefore the points at which the field strength has fallen in the room around 3 dB with respect to the maximum field strength. This angle is then described as beam width or aperture angle or half power (-3 dB) angle. The beamwidth of our antenna is equal 11.9°. As shown in the Fig. 4.3, the antenna pattern has radiation concentrated in several lobes. The radiation intensity in one lobe (major lobe) is considerably stronger than in the others, the side lobs ratios are about -8 dB and -12 dB. Knowing the antenna parameters allowed us to estimate a rate at which the antenna position had to be changed during the data acquisition. As calculated, even if the coordinates from the radiosonde (Chapter 4.1) were updated in every 20 seconds, the beamwidth of the antenna would still enable satisfactory tracking of the balloon and reception of the data. Thus, short breaks in the radiosonde GPS signal do not influence the data acquisition drastically. The steering of the antenna is provided by an electronic control unit. The unit connects the antenna with a 12 V DC power supply and with a computer, and the same enables data storage and antenna steering. A photo of the antenna is shown in Figure 4.4.

The first point before every data acquisition is setting the antenna in a start position, what means orientating it horizontally in the north direction. The azimuth and elevation angle of the antenna are screened on two 4-digit displays of the control unit. The steering procedure of the antenna can be carried out manually or automatically. The manual mode enables stepwise changing of the antenna's position directly on the control unit. In the automatical steering, the antenna's setting is changed according to GPS coordinates provided from an external source, in our case from the radiosonde. The position data are delivered in two text files `ant_pos.txt` and `balloon_pos.txt`. In the first one coordinates of the fixed receiving antenna are given, in the other one the GPS coordinates of the modem position. Those are commensurate with the radiosonde GPS coordinates. In both files the data are written in the following format: <Longitude in WGS84 Format>;<Latitude in WGS84 Format>;<Altitude in meters> for example: 11.18921;55.95844;227. The program scans the files in every 5 seconds, calculates the azimuth and elevation angles and sends the information via a COM port to the antenna control. Finally, the rotor changes the direction and tilt of the antenna.

The data received by the antenna are transmitted through the receiver module to the control unit and further saved as time data series to the computer. Whilst the receiving, the incoming data as well as the compression rate can be monitored and charted in a display of a BalloonDataLogger software developed by IAP (see Chapter 5).

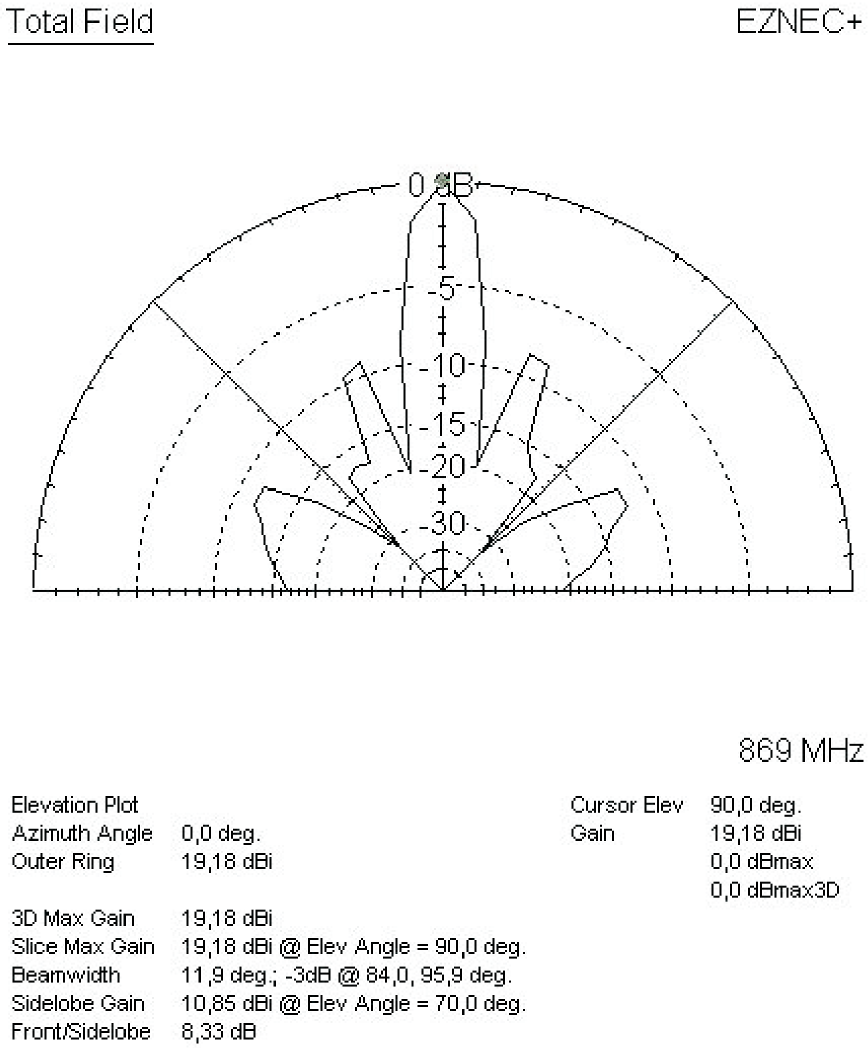

Figure 4.3: Characterization of 869 MHz helical receiving antenna.

4.3 The recovery system

To prevent problems with data acquisition in case of telemetry failure, as well as because of intension to recover the instrument for further use, a recovery system was attached to the payload. The used recovery GPS-9018/Akku system was developed by SELNEX-electronics. It is supplied with accumulators and provides long-lasting tracking in GSM zones. It includes GSM modem and a GPS receiver with corresponding antennas. The positions of the modem can be obtained instantaneously by SMS and online by a related software. Since the information from the recovery system is not needed during the sounding and since in the stratosphere the GPS and GMS signals are strongly limited, the recovery system was supplied with a power-on time delay relay device. The system activation time depends on the expected flight time and is set on 2-3 hours after the

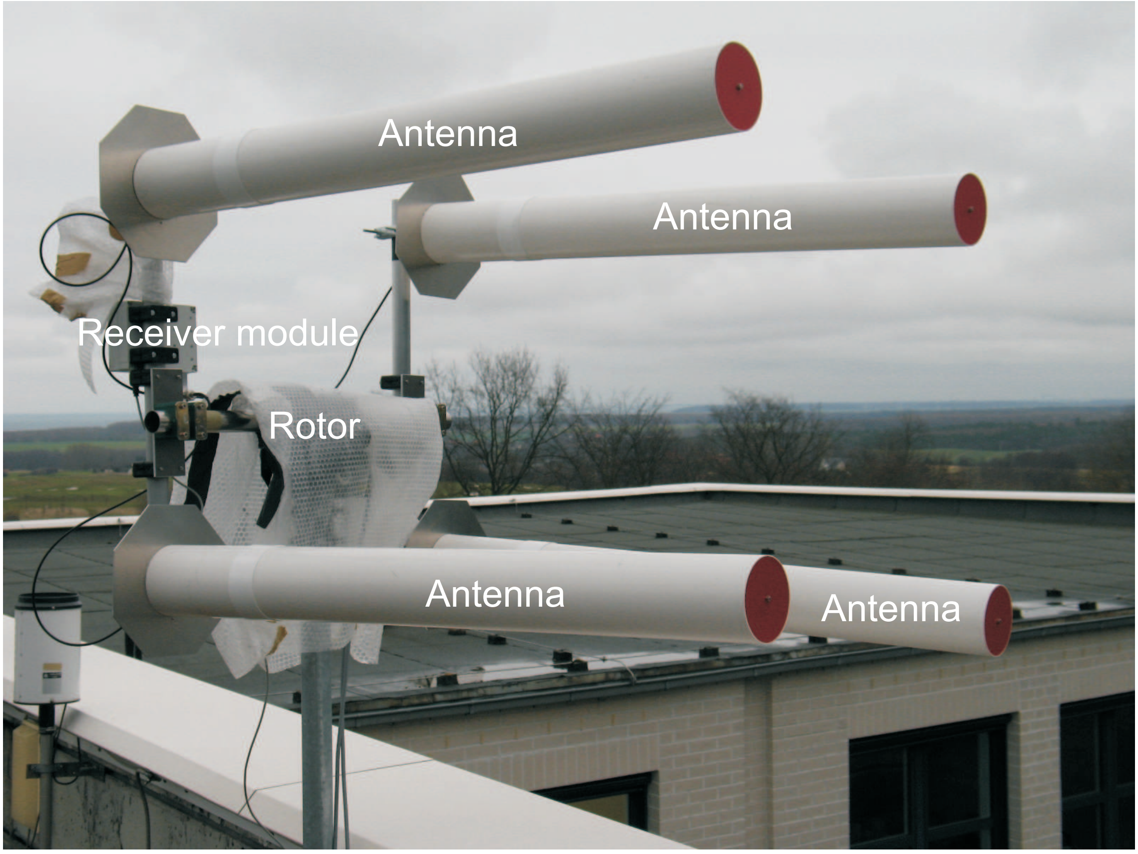

Figure 4.4: Receiving antenna on the roof of IAP, Kühlungsborn.

launch. It allows minimization of the battery power consumption and provides information on payload localization directly after the landing or shortly before it. Because of that the recovery procedure can be started even during the balloon descent.

5 Analysis software

The software system described in this Chapter was developed with the Borland Delphi 6.0 developer package and consists of two main parts: BalloonDataLogger serving for compression of the binary data and as a display for the received data and WindData providing the velocity data determination and analysis.

The CTA signal is recorded with a sampling rate of 2 kSamples per second and resolution of 16 Bit. The data are saved to the 128 MByte SD-card and simultaneously transmitted by the telemetry antenna. Because the bandwidth of the transmission line does not enable recording of the data of such high data rate, data compression is necessary. Additionally, bytes for the data synchronization and data quality examination are needed. An appropriate compression routine was developed by Torsten Köpnick from IAP, Kühlungsorn. The software groups the data within the telemetry signal in frames of 21 samples each. The first sample in every frame is completely coded, and from the following ones only the differences between the particular sample and its predecessor are recorded. The largest difference provides information on a compression degree. All difference values are reduced to the minimal necessary number of bits. Every byte is filled with 7 bits only. A bit with the value of 128 indicates the beginning of a new frame and is not disposable for data writing. In every fifth frame a timestamp is placed. After every 500th frame (ca. in every 5 seconds), a counter position is incremented and the position number is included into the 500th frame. Thus, in a case of any break during the data receiving, the time allocation of a particular sampled value is possible. To identify a transmission error, a checksum is created for every frame.

During the measurements, the data received by the antenna are saved in ASCII files of 355 kByte each. During 2 hours of data acquisition approximately 300 of those files are saved. An ASCII file from the SD-card has a size of about 100 MByte in case of 2 hours of observation. Those data are handled by the WindData software, which was developed within this work and will be described further in this chapter.

5.1 WindData software

The first procedure of the WindData program is the reconstruction of the actual binary data, implementation of a time information and combining the data field with other data sets. The additional data are necessary for estimation of the time-voltage, time-velocity field and analysis of the obtained results. The calibration data of a particular sensor are included in an INI FILE. In the INI FILEs one can find the time of the calibration, number of the telemetry modem with which the sensor was calibrated, calibration parameters, ambient temperature T_0 during calibration and sensor hot temperature T_w.

Data saved on the SD-cards do not include any time information, and this one is as well provided by the INI FILEs. All those data are necessary for the voltage-velocity transformation and data correction (see Chapter 3), which are further proceeded by the software.

Flight analysis requires the data from radiosonde. The radiosonde provides height after distinct flight time, that allows converting time-dependant velocity into height-dependant. The altitude information is given in every 2 seconds. Thus, before the conversion, the radiosonde altitude data are interpolated with 1000 points per interval. The acquired resolution depending on the ascent velocity is 10^{-3} m - 10^{-6} m. That enables creating the height-dependant wind field. Furthermore, radiosonde provides the information on temperature and pressure at different altitudes. This is needed for correction due to the ambient conditions. In case of on-ground or laboratory tests those data are manually entered into the program, as shown in Figure 5.1.

The procedure of data reconstruction and creation of the time-altitude-voltage field takes about 8 minutes at a typical PC, if the radiosonde data are available. To enable fast data handling, the field is saved in form of a stream into a file. The stream file of 2 hours long observation has a size of approximately 100 MByte. The data utilized for transformation are displayed in the main panel of the WindData interface. The calibration polynomial coefficients and eventual stable temperature and pressure during an experiment (as shown in the left screenshot from Figure 5.1), as well as the date and the record number of the radiosonde data bank can be recalled.

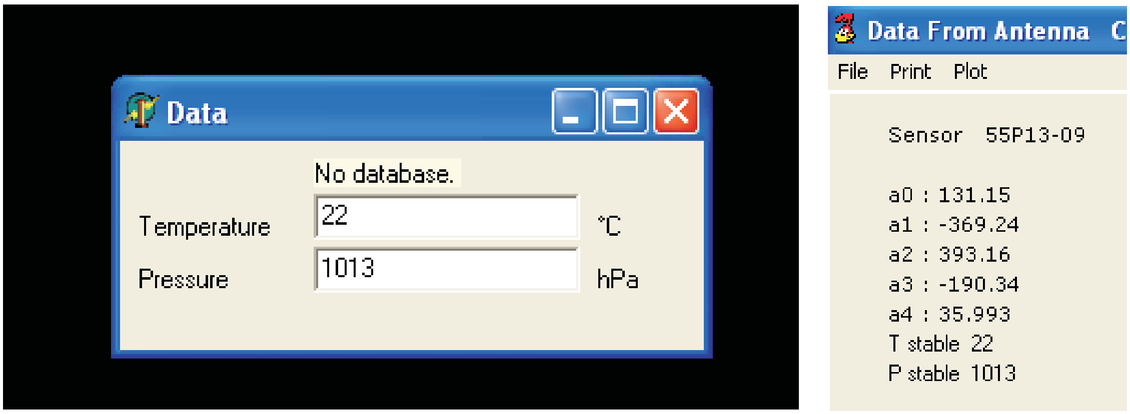

Figure 5.1: Screenshot of module for manual inscription of the ambient conditions. In case of on-ground or labor measurements, the ambient temperature and pressure data can be entered manually (left picture). The program displayed the information on the main panel under the calibration coefficients.

The full screenshot of main software module is shown in Figure 5.2. The main panel serves not only for data displaying (number 1. and 3. in Figure 5.2), but also as an instrument for data series analysis. One can plot here the time-velocity fluctuations, altitude-velocity fluctuations, wavenumber-PSD or frequency-PSD curves of data blocks with 2^n data samples, where n is an integer and $12 \leq n \leq 18$. The blocks' sizes result from the power-of-two criterium used in the Fast Fourier transform (FFT) and correspond to packages of data approximately 4, 8, 16, 32, 64, 128 or 256 seconds long. Another chart possibility is the Wavelet analysis of a particular package. The length as well as the altitude or time of an investigated package can be freely changed on a panel marked in Figure 5.2 with number 2. and named PLOTS. Furthermore, the voltage and velocity data can be seen in the listbox.

Additionally, the software provides a possibility of simultaneous display of data from the whole flights as a function of altitude (see Figure 5.3). The data are then averaged in 1 second steps. That allows a quick identification of regions of larger wind fluctuations. Analysis of velocity fluctuations in a freely chosen region is possible by an additional panel, which enables zooming into the altitude-velocity field. This panel is shown on the right-hand side in Figure 5.3.

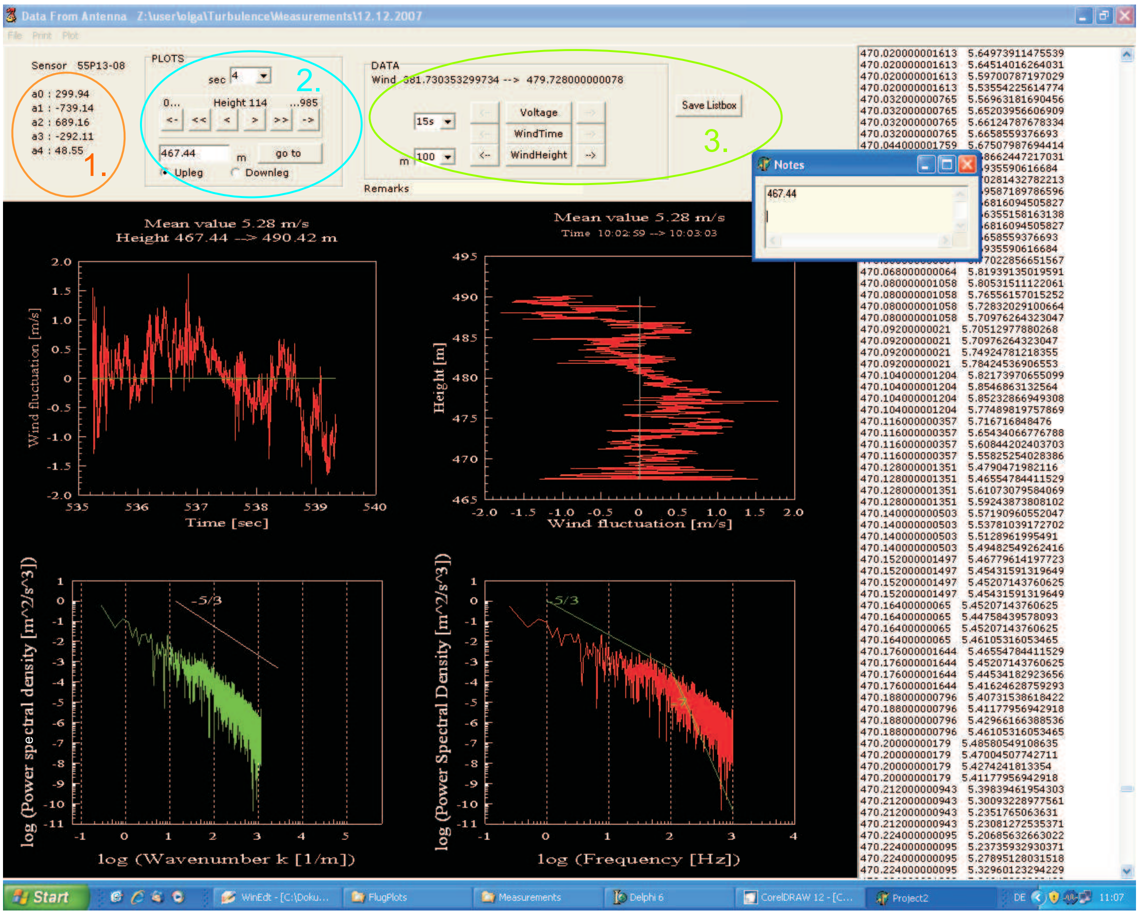

Figure 5.2: Screenshot of the main panel of the analysis software.

5.2 Methods of mathematical analysis

Two main methods utilized for data analysis are the power spectral density (PSD) and wavelet transform. The spectral analyses are used to provide information about how the

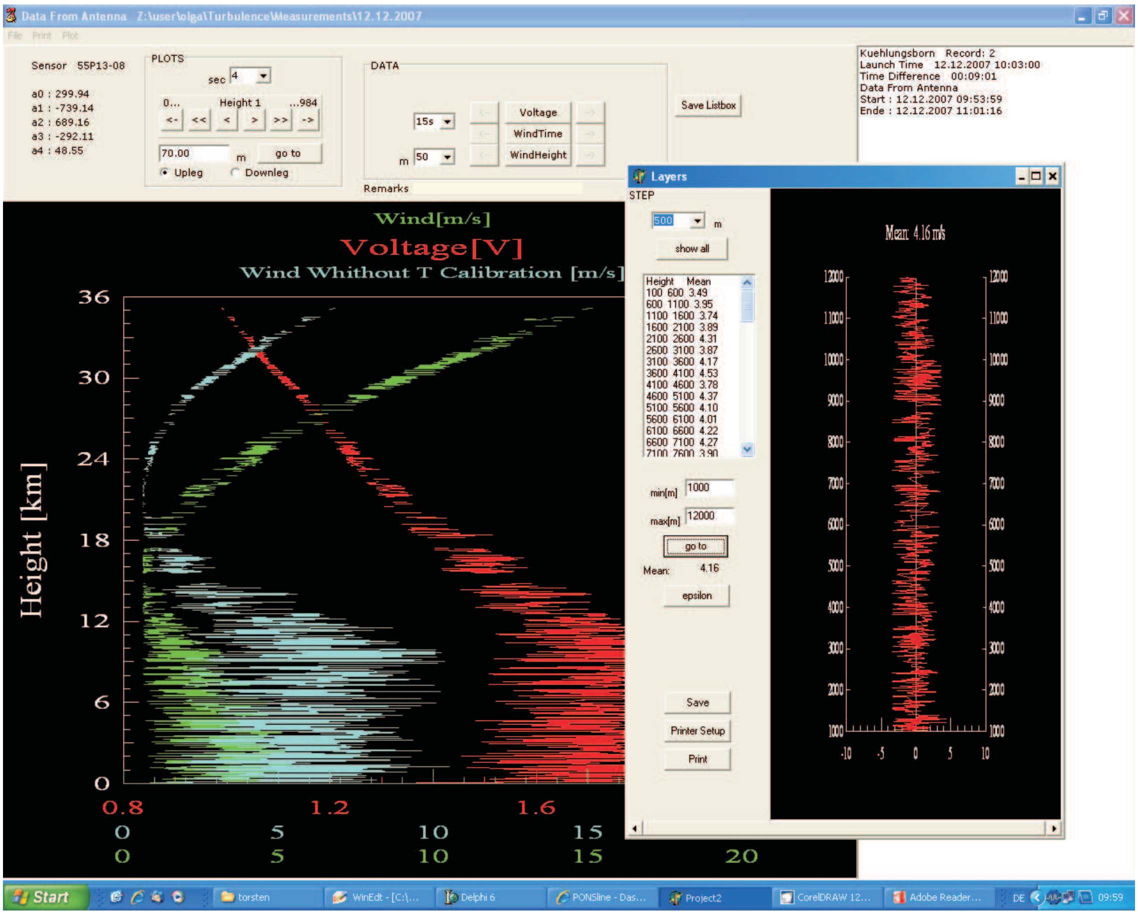

Figure 5.3: Screenshots of modules for analysis of a whole flight data set.

energy of the signal is distributed with respect to the frequency (or wavenumber). The diverse algorithms used for calculation of the spectra base on the Fast Fourier Transform, which produces values of discrete frequencies within sub-records of the signal. In other words, taking the Fourier Transform of a correlation function leads to frequency-domain representation in terms of the spectral density function. In our case firstly the mean wind of an analyzed data window is calculated and subtracted from the wind data. Next, the Hanning data windowing is performed. Due to the windowing the information leakage is reduced and frequency resolution segregated. Because of that, the accuracy of the amplitude is improved. The utilized formula is displayed below.

$$U'_H = \frac{1}{2}[1 - \cos(\frac{2\pi U'}{N})] \tag{5.1}$$

The U'_H is the wind fluctuation after the windowing, U' before and N the number of samples in the window. After this procedure the power spectral density estimation is carried out according to a method that follows a procedure described by *Press et al.* [1992].

The frequency-wavenumber transition is performed according to the formula:

$$k = \frac{2\pi f}{\overline{U}} \tag{5.2}$$

where k is the wavenumber, f frequency and $\overline{U}$ corresponds to the mean wind (or mean wind shear in case of the balloon flight) in a particular data block.

The wavelet transform is a relatively new and still developing spectral analysis tool. In contrast to the Fourier analysis, which decomposes time series into a sum of the infinite in-time harmonic functions, namely sine and cosine, the wavelet analysis decomposes the signal into the time-frequency domain. Wavelet transforms use analyzing functions, called wavelets, which are localized in space. For the analysis included in the thesis (see Chapter 6.3), the Morlet wavelet function was utilized. This kind of wavelet can be explained as a sine wave multiplied by a Gaussian envelope. The scale decomposition is obtained by dilating or contracting the Morlet wavelets before convolving it with the signal. The limited spatial support of wavelets is important because then the behavior of the signal at infinity does not play any role. Therefore, the wavelet analysis or synthesis can be performed locally on the signal, as opposed to the Fourier transform which is inherently nonlocal due to the space-filling nature of the trigonometric functions [*Farge*, 1992].

In the context of turbulence, the wavelet transform yields some elegant decompositions of turbulent flows. The continuous wavelet transform offers a continuous and redundant unfolding in terms of both space and scale. It enables tracking the dynamics of structures and measure their contributions to the energy spectrum. Furthermore, the discrete wavelet transform allows an orthonormal projection on a minimal number of independent modes which might be used to compute or model the turbulent flow dynamics in a better way than with Fourier modes [*Farge*, 1992].

Results of the FFT and wavelet analysis are described in Chapters 6 and 7. In the fist one the data from the laboratory and on-ground tests are analyzed. In the second one, one can find the analysis of data from the balloon-borne experiment.

6 Test measurements

The two main aims of the tests presented in this chapter were estimation of the CTAs' behavior during stratospheric soundings and selection of a suitable probe. The experiments were carried out in a wind tunnel, in a vacuum chamber and in the planetary boundary layer.

To select the proper probe for the stratospheric soundings, the 55P13 and 55P03 probes have firstly been calibrated (Chapter 6.1.1) and then their characteristics have been compared (Chapter 6.4). The effect of contamination has been investigated by the three 55P13 probe calibrations, that took place after definite periods of time (Chapter 6.1.2). Since the CTA's response is strictly dependent on the flow characteristics, the 55P13 probe has also been examined according to the condition during flight. Particularly, its response on the changing wind direction due to the pendulum movement of the balloon payload (Chapter 6.1.3) and on the changing pressure (Chapter 6.2) has been analyzed.

6.1 Wind tunnel experiments

Calibration of our MiniCTA systems and all the tests described in this chapter were made at the Chair of Fluid Mechanics (LSM, Lehrstuhl für Strömungsmechanik) at University of Rostock, Germany. The experiments were performed in the Göttingen type wind tunnel. A schematic sketch of this wind tunnel is shown in Figure 6.1. The open test section of the tunnel has a length of 1.40 m and height and width of 0.65 m. That gave us an opportunity to carry out many tests that require frequent changes in the probe setting. Especially, during the experiment on the CTA response on the changes in the wind direction (Chapter 6.1.3), the large sizes of the test section significantly simplified an access to the probe. The disadvantage of this wind tunnel is its disability of generation of stable velocities under 1 m/s. That impeded the probes calibration. During all the data acquisition the probes were kept in one place in the middle of the air stream and the velocities varied between 1 m/s and 15 m/s. Additionally, the probes' responses on the zero wind were measured.

6.1.1 Calibration

Every anemometer was calibrated with a defined telemetry modem (see Chapter 4.2.1). Firstly, overheat was adjusted for every single probe. For this we used the overheat spreadsheet developed by DantecDynamics (see Chapter 3). When the operating resistance on the MiniCTA bridge was fixed, the probes were exposed to different velocities,

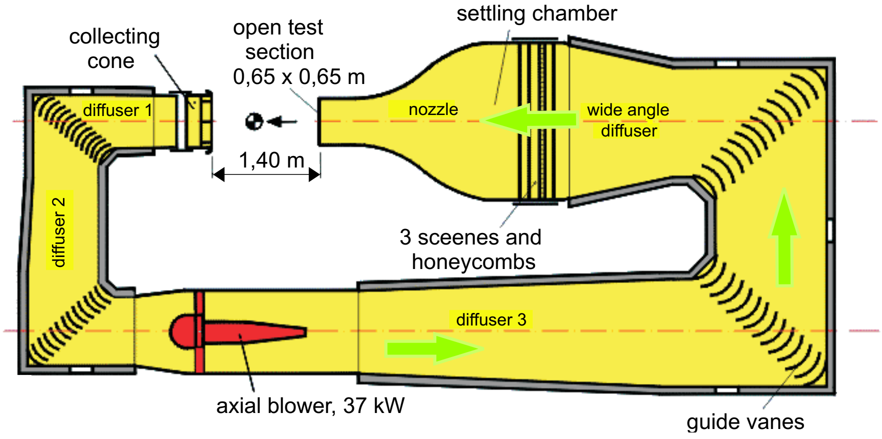

Figure 6.1: Schema of the Göttingen type wind tunnel used during the calibration and tests of CTA anemometers. Picture: courtesy of the Chair of Fluid Mechanics at University of Rostock.

U, in the wind tunnel. The true velocity was given by the tunnel operating software and was based on an internal laser sensor. During the calibration the velocities varied between 0 m/s and 15 m/s and the acquired voltage E was measured. The ambient temperature (T_0 =20 °C) and the pressure were kept constant.

Figure 6.2 shows two calibration curves of two 55P13 probes and one of the 55P03 probe. The green line corresponds to the $U(E)$ dependance of the 55P13 probe, that has been used in the experiments introduced later in this chapter. The yellow line represents the calibration of the 55P03 probe. The blue line characterizes another 55P13 probe. The comparison of the 55P13 probes indicates the necessity of the calibration of every single probe.

Figure 6.3 shows differential sensitivity of the same 55P03 and 55P13 probes. From the plot it can be verified that the 55P03 probe with the gold plated wire is able to measure the small velocities more accurately than the 55P13 probes. However, in almost all of the tests described in this thesis and during the first test flight, the 55P13 probes have been used. 55P13 probes were bought and tested several months before the 55P03 probes were ordered. This is the main reason why the examination of the 55P13 is more comprehensive than in the case of the 55P03. Another reason is the relatively low price of the not gold plated probes, which allowed us to carry many tests with those very perishable instruments.

The velocity-voltage relationships from Figure 6.2 were obtained as the least squares fit with a 4^{th} order polynomial (see Chapter 3.4). To estimate the accuracy of this fitting, the King's law fitting was additionally investigated. Charts from Figure 6.4 show analysis of two different calibration fittings in the region of velocities between 0 and 1.9 m/s (big chart) and between 0 and 15 m/s (small chart). The low velocities are of special interest in turbulence measurements and the suitable fitting in this region is crucial. However,

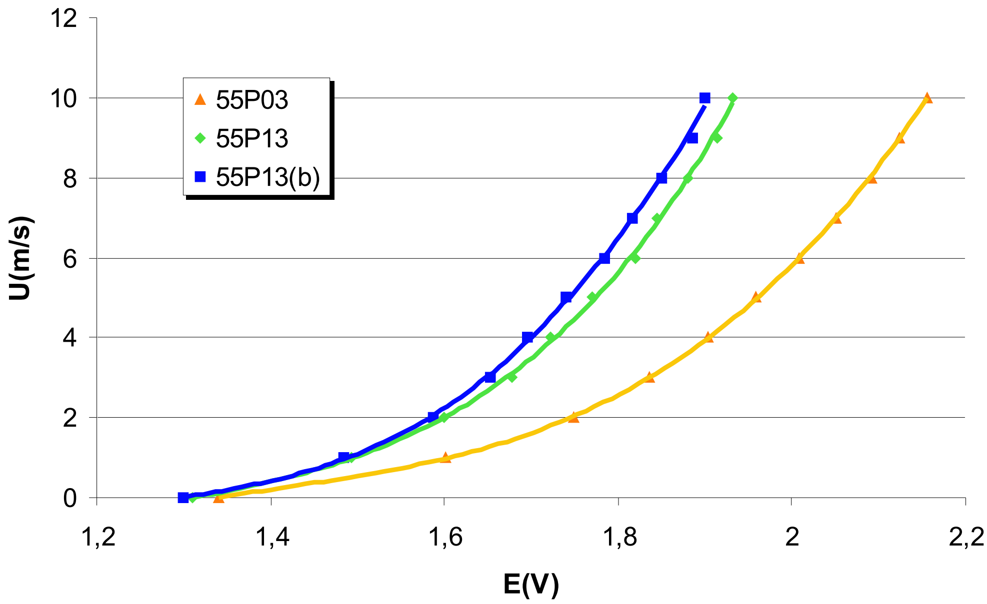

Figure 6.2: Calibration curves of two 55P13 (green and blue line) and 55P03 (yellow line) probes from 19^{th} May 2008. The calibrations were carried out at 20°C.

due to the technical limitations of the LSM wind tunnel, the measurements of the small velocities provide many difficulties. The minimal, non-zero, stable velocity reached in our tests was 1 m/s. Below this value the measurements were not possible. The black line on the plot represents the linear interpolation curve of the acquired data. The other two lines are the polynomial curve of the 4^{th} order (green line) and the King's law curve (violet line) fittings. Those two methods of curve fitting have been introduced in Chapter 3.4 as the main procedures of transfer function calculation.

Both curves provide acceptable and similar results in the higher speeds range. However, below 1 m/s the King's law does not provide probable fitting. The King's law requires the squares of voltage values larger than the coefficient A. If the squares are smaller, a root of zero or minus value occurs. During the calibration, the smallest acquired voltage equaled 1.23 V. Square of 1.23 V gives value larger than A. However, under different ambient conditions, CTA provides different voltages at defined winds (cf. Chapter 3.5). It means, that without proper corrections, the measured voltage can be lower than 1.23 V and a root of a minus value appears. As long as the voltage correction due to the varying ambient conditions is not complete, the King's law can not be applied. Furthermore, the n in Eq. 3.11 is velocity dependant [*Jørgensen*, 2002]. The polynomial fitting enables more calculational and acceptable fits in the low velocities range. Because of that, in our probes' characterization this kind of fitting has been mostly used.

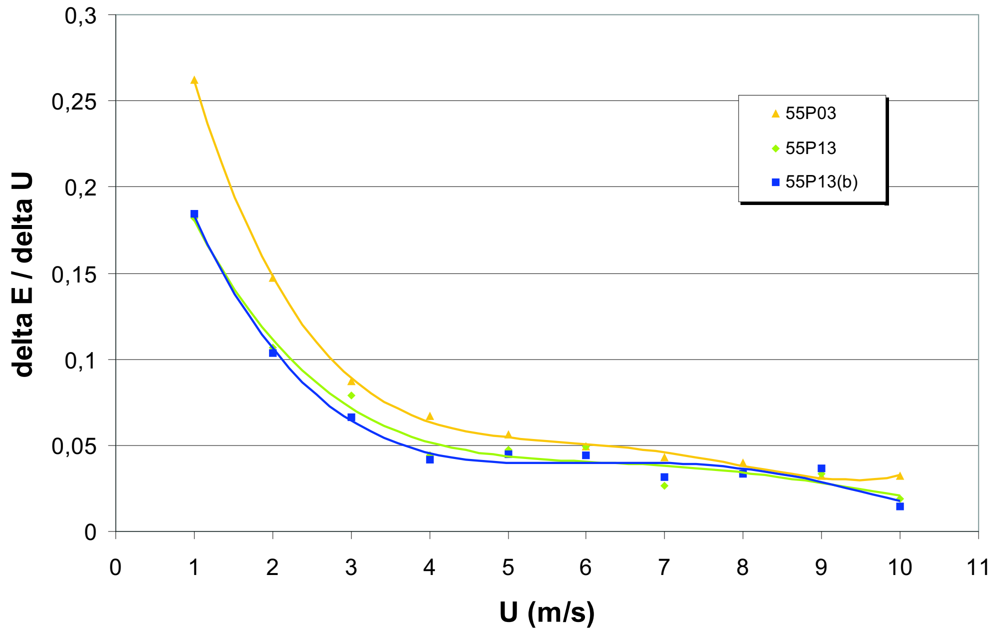

Figure 6.3: Comparison of differential sensitivity of two 55P13 probes (green and blue line) and 55P03 (yellow line) probe.

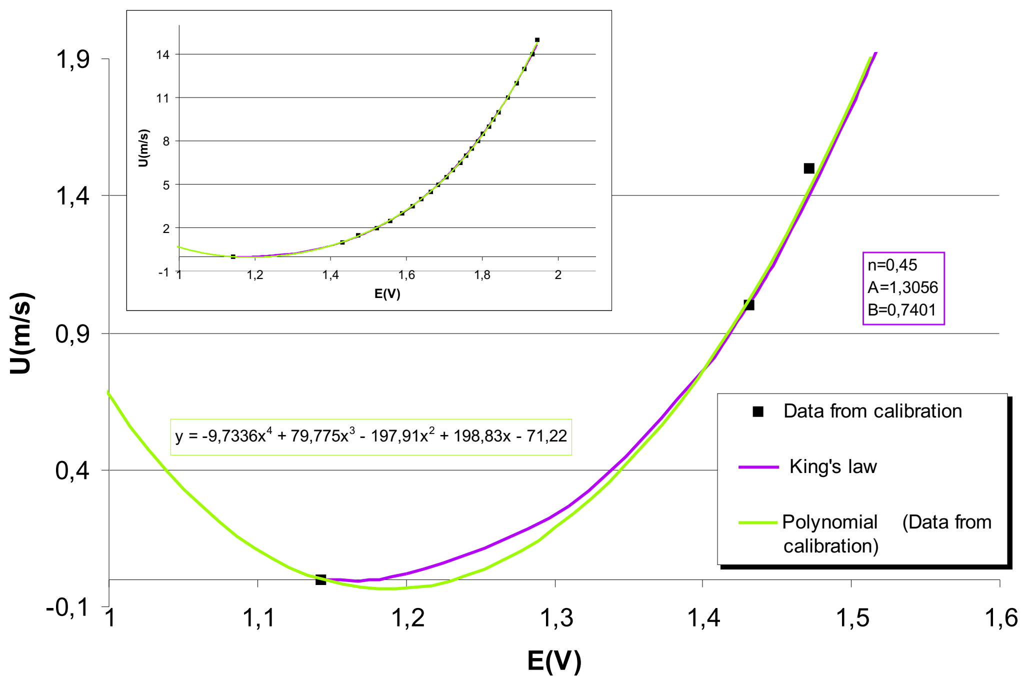

Figure 6.4: Different calibration fittings of the 55P13 probe. The black squares correspond to the data acquired during the calibration. The two lines are the King's law and polynomial curve fittings, parameters of the curves are given in the boxes.

6.1.2 Contamination effect

The deposition of impurities in the flow around the sensor can drastically alter the calibration characteristics and reduce the frequency response. Acquiring representative results requires cleaning the wire, what may cause the sensor damage. Another solution is recalibration of the probe. Figure 6.5 indicates the importance of this procedure. The lines shown on the plot represent the polynomial lines of the data acquired during different calibrations of the 55P13 probe. The first calibration took place in October 2007, the second in May 2008 and the last one in June 2008. Between the calibrations the probe was used in several outdoors and laboratory tests. During this time, due to the contamination not only a voltage measured by a defined wind increased, but also the calibration curve incline changed. After this experiment, to ensure the validity of the calibration, we limited our operation procedure to periods of 2 weeks after the calibration.

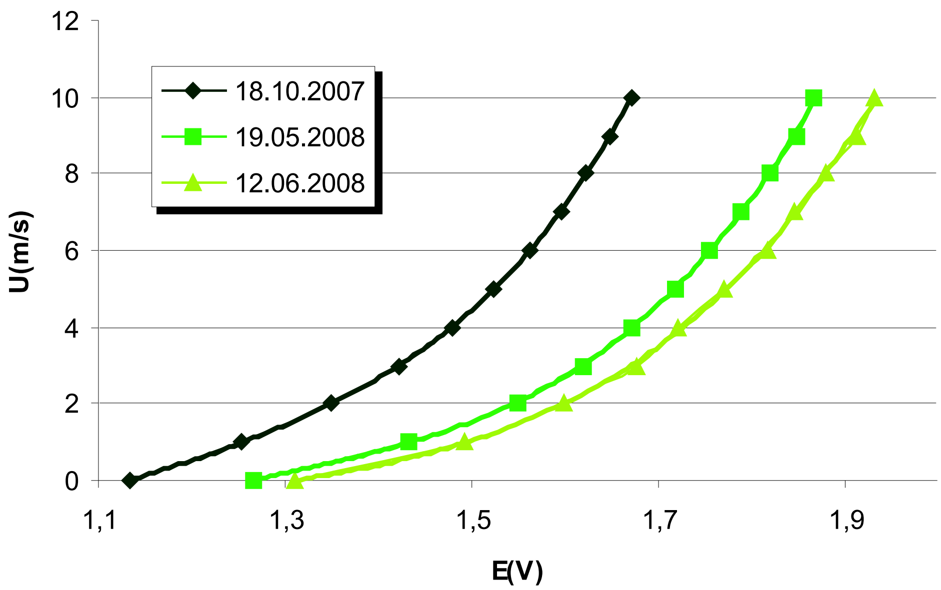

Figure 6.5: Three calibration characteristics of one 55P13 probe obtained at different days. The temperature by all of the data acquisitions was kept constant and at 20°C.

6.1.3 Pitch and yaw effects

During the flight, the CTA's probe is placed vertical to the payload and above the center of mass of it. The payload is suspended from a balloon and thus experiences rotation and pendulum movements. That can strongly influence the response of CTA. If the wire had infinite length, then the components of a flow parallel to the wire would have no effects on it. The effective cooling velocity that the sensor experienced would be that which was perpendicular to the sensor. Furthermore, the absence of prongs would prevent creation of perturbation around of the wire. However, the wire has a finite length. Because of that the temperature is not constant over the whole length of it and aerodynamic perturbations are created by the prongs. To estimate the magnitude of those effects on the CTA's response during balloon-borne stratospheric soundings, the evaluated velocities for changing sensor yaw and pitch orientation have been investigated.

During the velocity calibration described in Chapter 6.1.1, the wire was set perpendicular to the mean-flow direction. This position of the 55P13 probe corresponded to $\alpha = 0°$, and the velocity calibration part of the yaw and pitch investigation was therefore carried out at $\alpha = 0°$. Directly after the sensor calibration, the yaw effect was investigated. The 55P13 probe was fastened to a rotating stand with a protractor, as shown in the Figure 6.6, and placed in the wind tunnel. The wind velocity in the wind tunnel was set to about 5 m/s. After the measurement at $\alpha = 0°$, the sensor was turned by 10° angle. The procedure was repeated till 180° was reached. Next, the flow velocity was decreased to about 3 m/s and the whole experiment was carried out once more.

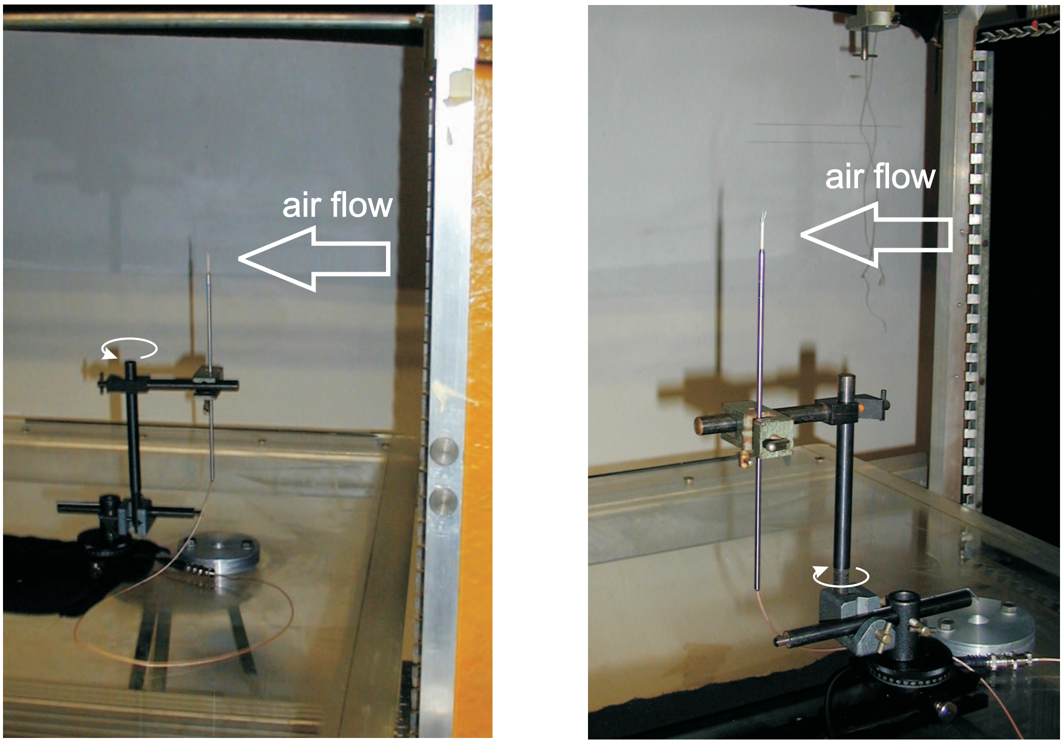

Figure 6.6: Experimental setup for the investigation of the yaw effect. On the left-hand side setup by $\alpha = 0°$, on the right-hand side by $\alpha = 180°$.

Figure 6.7 shows the results of those two experiments. The variation in the evaluated velocity is about 15-20 % depending on angle. It is obvious, that both data sets lines indicate the largest values at 90° and minimum measured values at the angle of 180°. Since the main aim of our turbulence measurements is finding the turbulent layers and estimation of their intensity, only relative wind is regarded. The apparent wind changes in the relative wind due to the rotation can be identified in the frequency analysis of the CTA's response and can be neglected in subsequent evaluations.

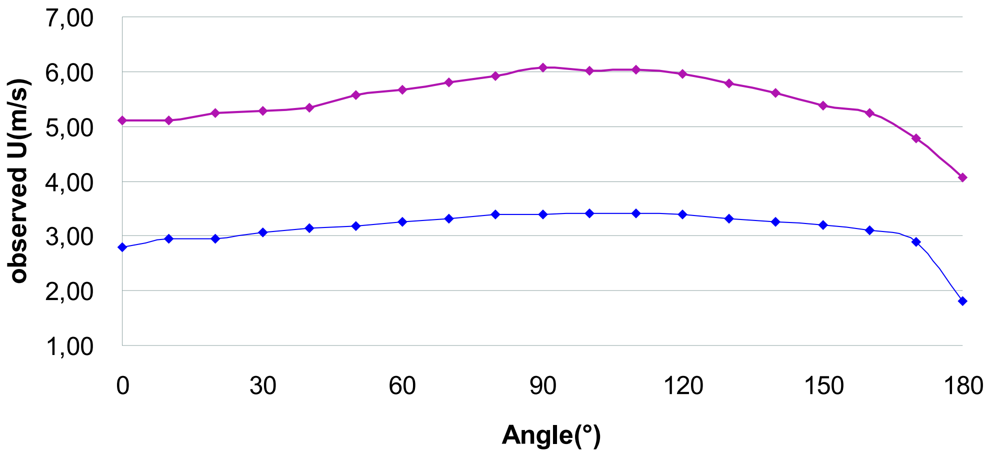

Figure 6.7: Comparison of the observed velocities for changing 55P13 sensor yaw orientation by the wind velocities of about 3 m/s (blue line) and about 5 m/s (violet line).

The pitch angular sensitivity was investigated similar to the yaw effect. The 55P13 probe was tilted in 10° steps. The setup used in this experiment is shown in Figure 6.8. The flow had velocities of about 3 m/s and about 5 m/s. The probe responded to pitch angle changes in a manner shown in Figure 6.9. The observed velocities changed significantly due to the changing orientation. However, the pendulum movement of payload below the balloon has typically an angle not larger than +/- 10°. Figure 6.9 shows, that between those angles (region within the green rectangle) the influence of the probe orientation is relatively small. In case of both curves the variation in the observed velocity is less than 5 %. Furthermore, as in the case of rotation movement, the pendulum frequency can be revealed in the FFT of CTA's response analysis.

The experiments carried out in the wind tunnel provided information on probes' behavior under varying wind conditions. The results of the experiments showed, that every single probe has to be calibrated and that the 55P03 probes are more accurately than the 55P13 ones. Furthermore, two possible calibration curves were compared, the King's law and the least squares fit with a 4^{th} order polynomial. The second one provided better fitting at the velocities below 1 m/s and was chosen as the main procedure of transfer function calculation. To estimated the contamination effect on the probes, we calibrated a 55P13 probe three times at different days. We noticed that with the time, the voltage measured at defined wind increased and that the calibration curve incline changed. To ensure validity of the calibration, we decided to limit the operation procedure period to 2 weeks after the calibration. We investigated the probe response on changing sensor yaw and pitch orientation. Depending on the angle the variation in the evaluated velocities equaled about 15-20 % due to the yaw effect and 5 % due to the pitch effect. Those

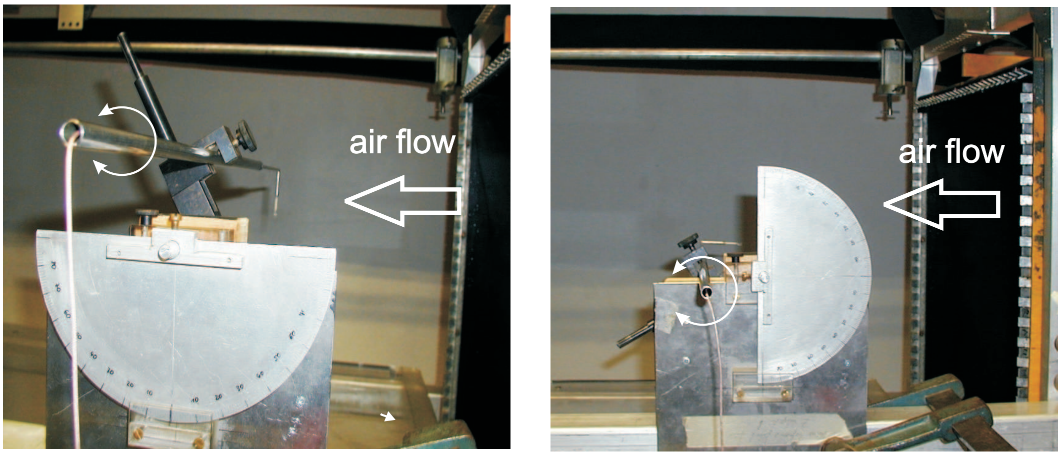

Figure 6.8: Experimental setup for the investigation of the pitch effect. On the left-hand side setup by $\alpha = 0°$, on the right-hand side by $\alpha = 90°$.

apparent wind changes can be identify in the frequency analysis of the CTA's response and can be neglected in subsequent evaluations.

6.2 Tests in vacuum chamber

Pressure, as an atmospheric variable, is strongly combined with the density and the mean free path of particles in the air. Thus, changes in the pressure significantly influence the heat conduction from the CTA's wire. Considering that fact, it becomes obvious, that the CTA measurements at different altitudes require correction due to the varying pressure. Unfortunately, up to now there are no scientific publications regarding to this problem.

To predict and understand the influence of the low stratospheric pressure on the CTA's response, 55P13 probes were placed in a vacuum chamber and their response on varying pressure was measured. The pressure was changed from 1000 hPa to approximately 5 hPa, which was the lowest pressure possible with the utilized vacuum chamber. That enabled performing the experiment under conditions similar to those experienced in the stratosphere. Due to the small sizes of the vacuum chamber, it was imposable to insert a wind tunnel into it. Larger vacuum chamber was unfortunately not available. Because of that, the tests were carried out at the flow velocity of 0 m/s. Figure 6.10 shows velocities evaluated by two different probes at different pressures. As one can see, both curves have a characteristic slope with strong incline at pressures lower than 200 hPa. Similar behavior was observed in the data acquired during the first test flight, the equivalent results are included in Chapter 7.1. A final correction of the vacuum effect is up to now not possible, as the sensor can not be calibrated in the vacuum chamber with non-zero wind velocities.

The Fast Fourier Transformation (FFT) of the data acquired in the vacuum chamber allowed us to identify a noise level of the CTA signal. Plot 6.11 shows the FFT analysis of a about 0.5 and 4-seconds long data sets provided by CTA at 1013 hPa under no wind

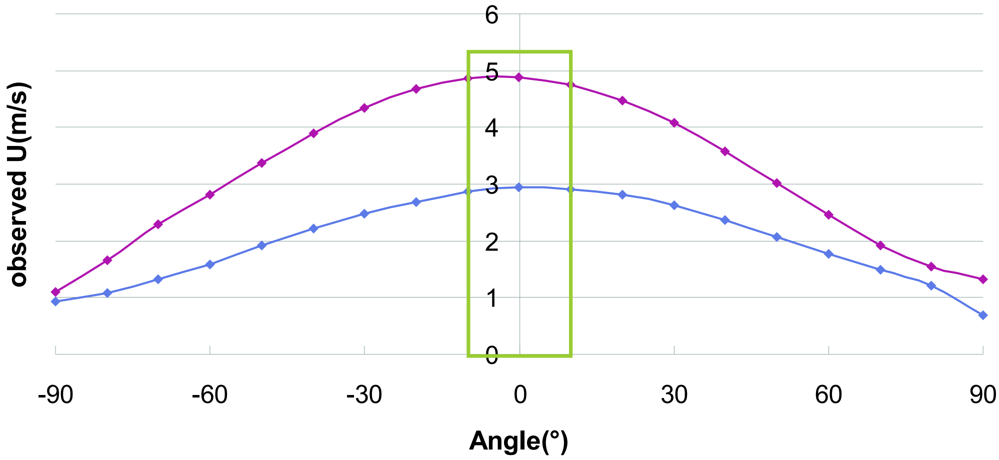

Figure 6.9: Comparison of the observed velocities for changing 55P13 sensor pitch α orientation by the wind velocities of about 3 m/s (blue line) and about 5 m/s (violet line).

conditions. This information allows us to estimate the white noise at the scales under the $\sim 10^{-6}$ of frequency PSD. In case of the 0.5 second long data set (left plot), the white noise level is at about $\sim 10^{-7}$, in the 4-seconds long set (right plot) the noise level is at about $\sim 10^{-8}$. This effect might be caused by the Hanning data windowing (see Chapter 5.2) performed before the FFT analysis. As one can see both of the showed spectrum are not totally flat. We assume that the measurements were influenced by the sound waves generated in the laboratory.

The experiment in the vacuum chamber revealed the importance of the CTA measurements correction due to the changing pressure. The probes' response on zero wind decreased strongly with the decreasing pressure. Up to now there is no formula, that could be used for the CTA data correction. To solve this problem, we plan to place a wind tunnel in a vacuum chamber and calibrate our probes under changing pressure conditions. The experiments in the vacuum chamber enabled identification of the white noise level of the CTA signal. We noticed also that the noise level in the PSDs depends on the amount of data samples. In case of the 1024 samples, the white noise level is at about $\sim 10^{-7}$, by 8194 at about $\sim 10^{-8}$. That is probably caused by the mathematical description of the utilized windowing and FFT analysis.

6.3 Comparison of 55P13 and 55P03 probe

Two available 55P13 and 55P03 probe types were evaluated by an experiment in the planetary boundary layer. An aim of this experiment was revealing the optimal probe type for atmospheric soundings, even if the lab tests and the prototype flight described in this thesis were limited to the more simple probe 55P13. The calibrated probes were placed at a height of 50 cm in the distance of 50 cm from each other. This setting

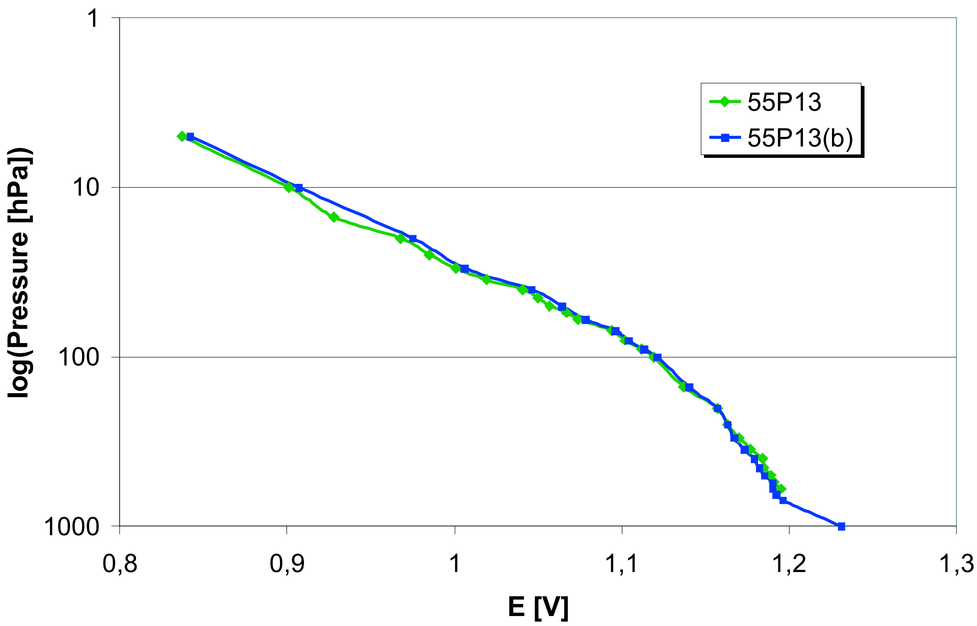

Figure 6.10: Ambient pressure influence on the 55P13 probes' response at flow velocity 0 m/s.

minimized the reciprocal influence of the probes on their measurements and ensured that both probes experienced a similar flow. The data sets from the CTAs were collected simultaneously.

Figure 6.12 shows examples of the wind fluctuations measured simultaneously with the gold plated 55P03 and the simple 55P13 probe. The displayed data series are 4- (right plots) and 8-seconds (left plots) long. Such short time periods enable determining the essential differences between the responses of these two probes. The 8-seconds long data series in both cases have a similar characteristics and mean velocity value equal 0.62 m/s. One can also see that the signal is more stable in the case of the 55P03 probe than in the case of the 55P13 probe. It evidences earlier mentioned (Chapter 6.1.1) higher response stability of the 55P03. The analysis of the 4-seconds long data series (right plots) shows the same behavior. The influence of this factor on the turbulence measurements can be determined in the FFT power spectrum (PSD). In Figure 6.13 the frequency (upper plot) and wavenumber (lower plot) PSDs of both probes of the same 4-seconds long data series are displayed. The analysis of the 55P03 signal (yellow PSD) shows noise at lower scales of PSDs than in the case of 55P13 signal (green PSD). The noise level of the 55P03 signal is at about $\sim 10^{-9.4}$ of frequency PSD and the noise level of the 55P13 signal is at about $\sim 10^{-8}$ of frequency PSD. The noise level occurs at lower frequencies in case of the 55P13 probe signal ($\sim 10^{2.5}$ Hz) than in case of the 55P03 signal ($\sim 10^{2.7}$). It means that the gold plated sensor is more accurate in turbulence measurements. Furthermore, the 55P03 wavenumber PSD indicates a bend from $-5/3$

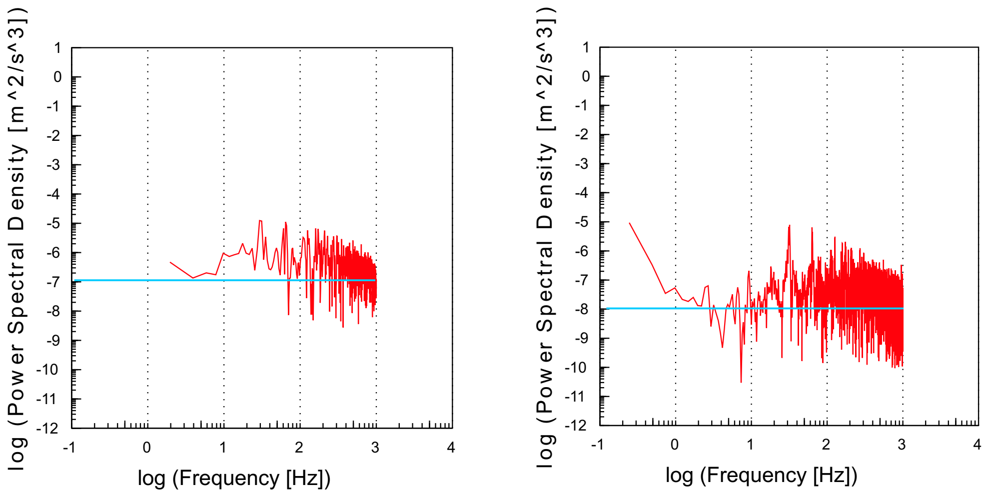

Figure 6.11: Power Density Spectrum of CTA data acquired during the experiment in vacuum chamber. The left exemplary data set contains 1024 samples (approximately 0.5 second of data). The right one 8192 (about 4 seconds). The pressure by acquisition was stable and equaled 1013 hPa. The blue horizontal lines indicate the approximate noise level.

to -7 at about 320 m^{-1} (blue line in the lower plot of Figure 6.13). That corresponds to the boundary between the inertial and viscous subrange, called the inner scale (cf. Figure 2.1). The differences in the wavenumber values reached by the 55P03 and 55P13 probes are caused by the various mean winds measured by the probes. The wavenumber $k = \frac{2\pi frequency}{\overline{U}}$, where $\overline{U}$ corresponds to the mean wind.

Since FFT spectral analysis can only provide nonlocal information, it carries limitation for the study of intermittent, nonstationary phenomena like turbulence, which displays rapid changes in phase, amplitude, and statistical properties. Due to those requirements, a wavelet analysis of the data provided by the 55P03 probe was prepared and plotted in Figure 6.14. The power is color-coded, as shown by the color bar on the right side. Red color reflects the highest power and the dark-blue to the violet the noise. The wavelet analysis was capable of resolving localized structures in the time-frequency domain. Although, the energy transport between the whole can not be observed, they are some smaller examples that indicate energy transport through adjoining scales. This can be seen at 115 and 117 second.

The differences in response of those two probe types result from their construction. The reduced accuracy of 55P13 turbulence measurements is probably caused by the interference from the prongs, which are directly connected to the wire. By the 55P03 the ends of the wire are gold platted, what defines accurately the sensing length and reduces the amount of heat dissipated by the prongs. This results in a much more uniform temperature along the wire than in the case of the not gold plated wire. Additionally, prongs of the 55P03 are more distant from each other. That minimizes the interference from the prongs on the flow at the point of measurement. All those factors increase the accuracy of the 55P03 measurement at high turbulence levels.

In the prototype flight the 55P13 probe was used. However, the results presented in this chapter and in Chapter 6.1.1 show that the 55P03 probe is more suitable for the atmospheric turbulence measurements. The 55P13 provides more accurate results at lower velocities. Because of that the next soundings are planned with the 55P03 probes.

6.4 Turbulence spectrum from on-ground measurements

The planetary boundary layer (PBL) is characterized by continuous turbulence throughout the layer and high energy dissipation due to friction. To examine the 55P13 probes' response in a turbulent flow, two probes were placed in the planetary boundary layer at different heights. One of the probes was attached to a 2 m long stand, the other one was set at a height of 60 cm. Figure 6.15 shows a picture and a sketch presenting setting of the probes. The experimental site was surrounded from north by the IAP building (10 m high, 4 m distant), from east by a small earth wall (2 m high, 4 m distant), from south by a bush and from west by a building (10 m high, 20 m distant) (see Figure 6.15). The wind blew from East and the probes were directed against the flow.

Figure 6.16 shows the wind fluctuations data provided by the anemometers during the experiment. The left plot corresponds to the data set acquired at 2 m, the plot on the right hand side to 60 cm. Although the flow characteristics are similar, the mean wind as well as the wind fluctuations have larger values in the upper layer. This wind characteristics agrees with the typical wind profile of the PBL, where the velocities increase with altitude due to decreasing friction. In our case the experimental site was shadowed by the small earth wall, that additionally impeded the wind in the lower layer and caused relative strong fluctuations at 2 m. When the easterly wind passed the earth wall it experienced a sharp direction change within the layer and that intensified the turbulent flow. This process influenced stronger the flow at the height of 2 m than at 60 cm.

The wind fluctuations at both heights are analyzed using smaller data windows. Figure 6.17 shows an analysis of two exemplary consecutive 16-seconds long data series. Upper and lower plots in this figure correspond respectively to the measurements from 2 m and 60 cm. At both heights the turbulence occurs and the equivalent PSDs show similar characteristics. In both layers the inertial ($k^{-5/3}$) as well as the viscous (k^{-7}) subsections can be observed. The theoretical turbulent spectra (black lines) have been fitted as suggested by *Lübken et al.* [1993]. Due to this fitting, the TKE dissipation rates ε and inner scales l_o could have been estimated. The inner scale l_o is at about 0.01 m in all cases. ε equals 0.001 W/kg to 0.003 W/kg. The noise-level in all cases in at about $\sim 10^{-10}$ of wavenumber PSD.

To verify our assumption from the Chapter 6.2, that the noise level depends on the amount of samples in the analyzed data set, we analyzed 4 data sets of various length acquired at 2 m above the ground. The corresponding spectra are presented in Figure

6.18. The frequency spectrum of 1-second long data set shows noise at $\sim 10^{-9.1}$ of PSD, 2-seconds long at $\sim 10^{-9.9}$, the 4-seconds long at $\sim 10^{-10}$ of PSD and the 8-seconds long at $\sim 10^{-10.2}$ of frequency PSD. It confirms the effect observed in the PSDs of the white noise measured in the vacuum chamber (Figure 6.11). The noise level of PDSs of longer data series is at higher wavenumbers than in case of shorter data series.

The experiments allowed us to assume that the sensors work well and are appropriate tools for the turbulence measurements under out-door conditions. The acquired data agree with the estimations and suit to the wind profile typical for the PBL. High spatial resolution was achieved, what provided information on turbulence. The noise level was significant only at very fine scales ($\sim 10^{-10}$ PSD) at longer data series (4, 8, 16 second). That confirmed results of the measurements in the vacuum chamber (Chapter 6.2).

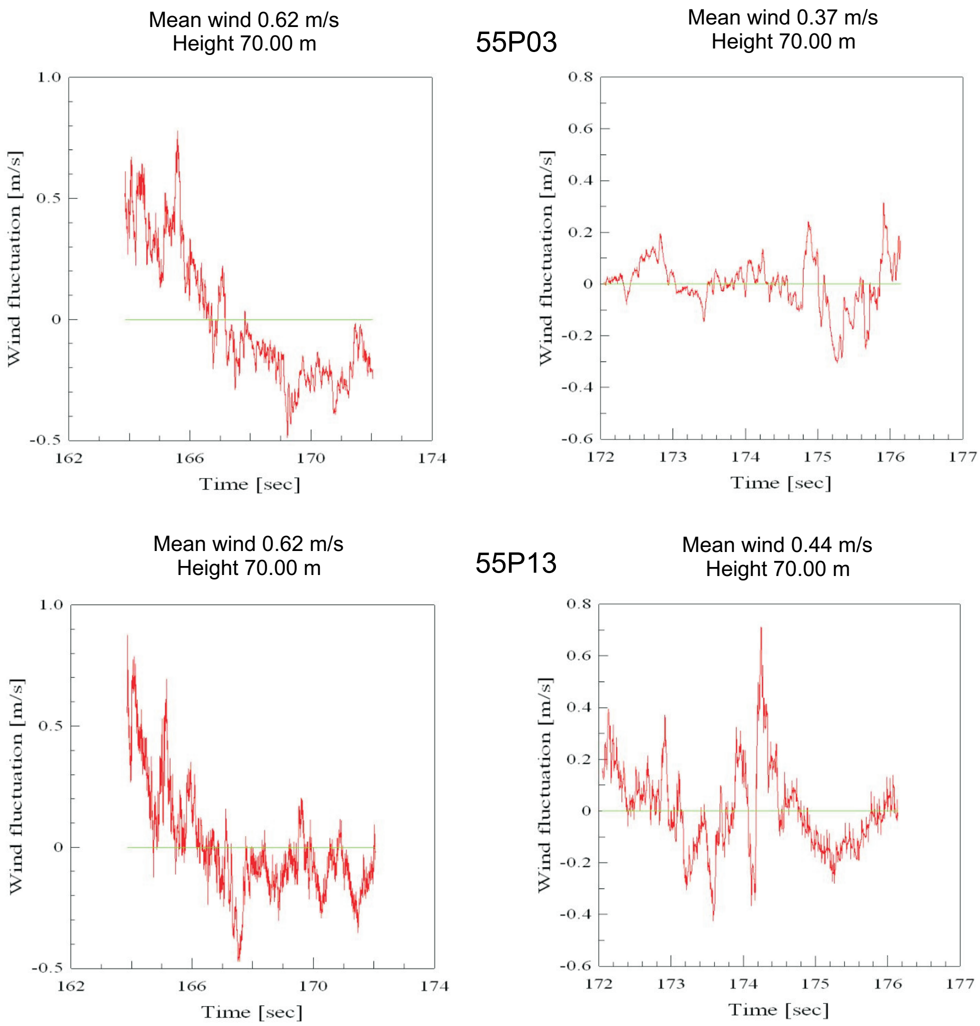

Figure 6.12: Comparison of two data time series acquired with the 55P03 and the 55P13 probe in the planetary boundary layer. Experiment took place on 14h July 2008. Left plots show 8-seconds long data sets. In the right plots the data sets are 4 seconds long. Evaluated mean winds are given above the plots.

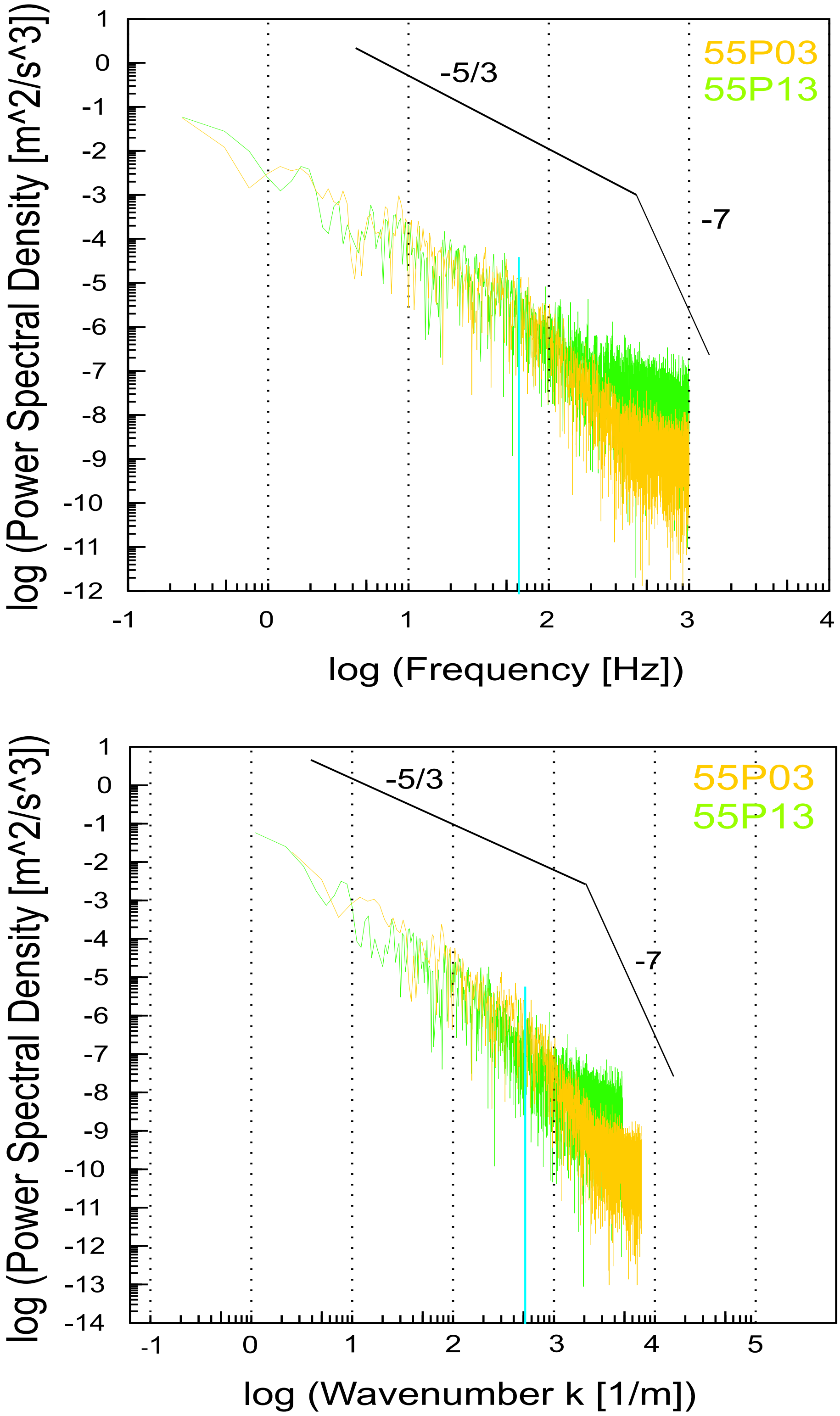

Figure 6.13: Comparison of PSD of 4 seconds long data sets acquired simultaneously with the 55P03 and the 55P13 probe on 14th July 2008. Upper plot presents the frequency PSDs, the lower one the wavenumber PSDs. Blue vertical lines indicate bends between inertial $-5/3$ and viscous -7 subsections of the spectra.

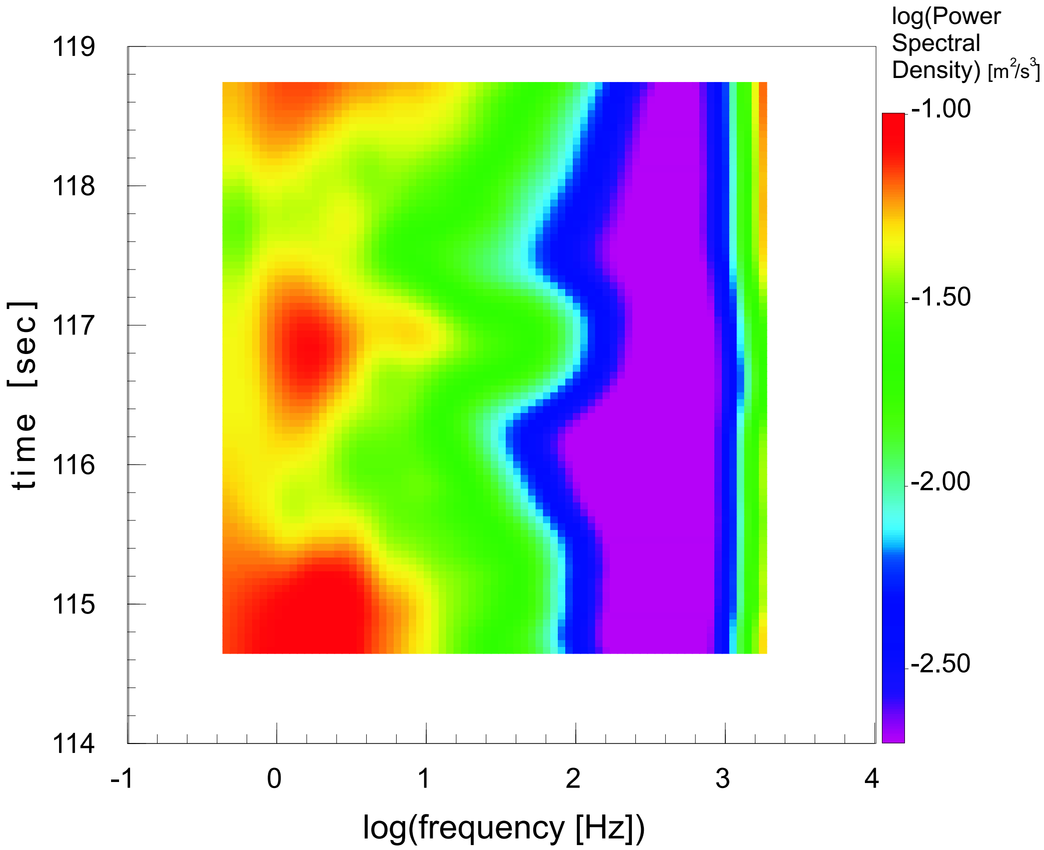

Figure 6.14: Wavelet power spectrum of wind fluctuations measured with the 55P03 CTA probe during measurements within the planetary boundary layer on 14th July 2008.

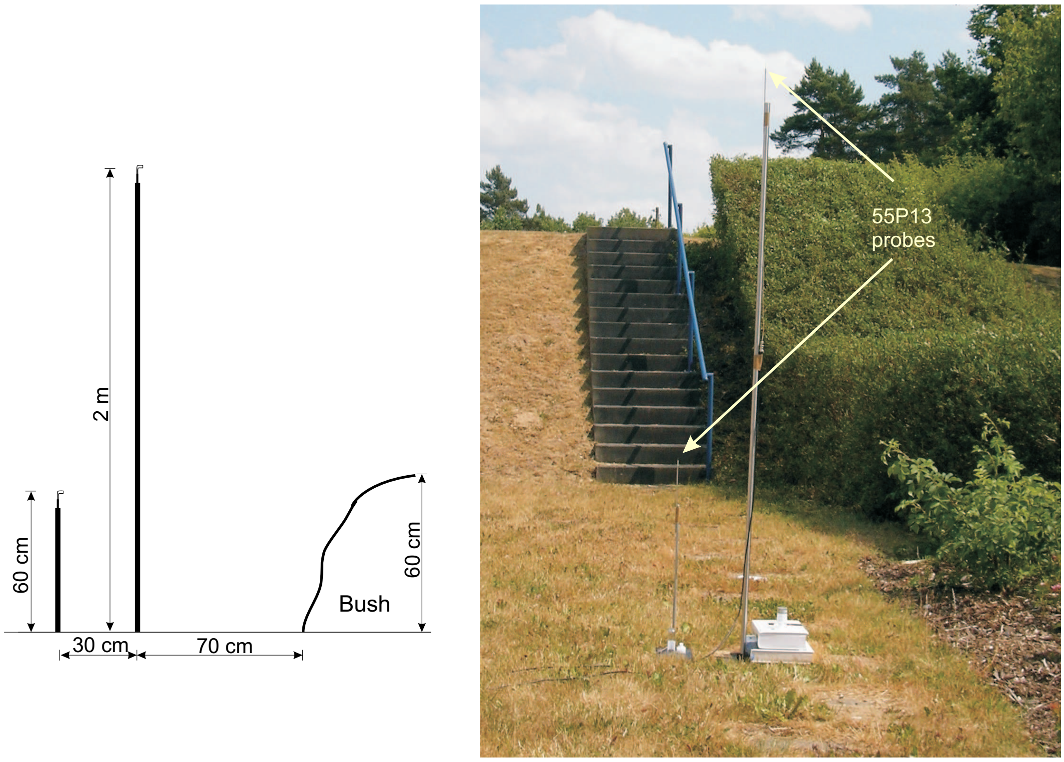

Figure 6.15: Schema of an experiment in the Prandtl boundary layer with two 55P13 probes placed at different heights. The wind blew from East (from the small hill with stairs in the direction of probes) and the probes were directed against the flow. The experiments was carried out on 10th September 2008.

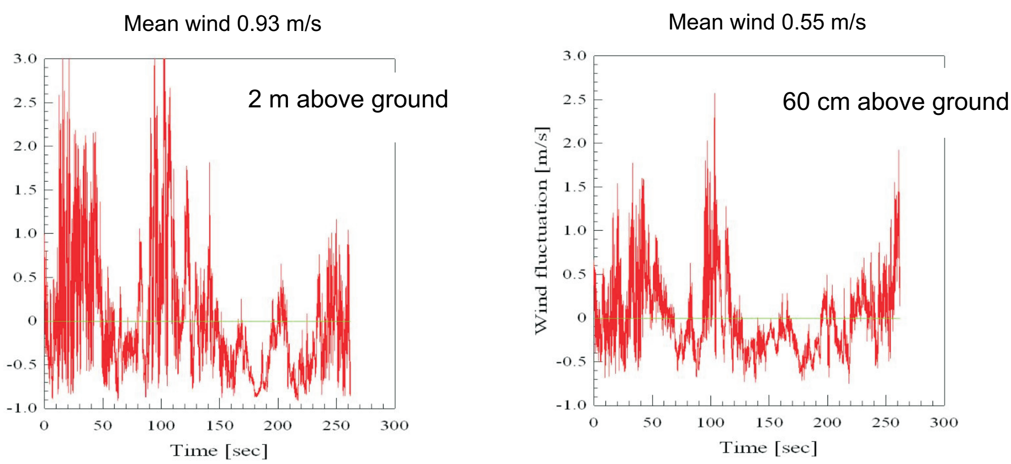

Figure 6.16: Wind data series from the measurements in the planetary boundary layer from 10th September 2008. Plot on the left hand side presents the data set collected by a 55P13 probe placed at 2 m height. The right plot shows the wind data evaluated by a 55P13 probe set at a height of 60 cm. Mean winds are given above the plots.

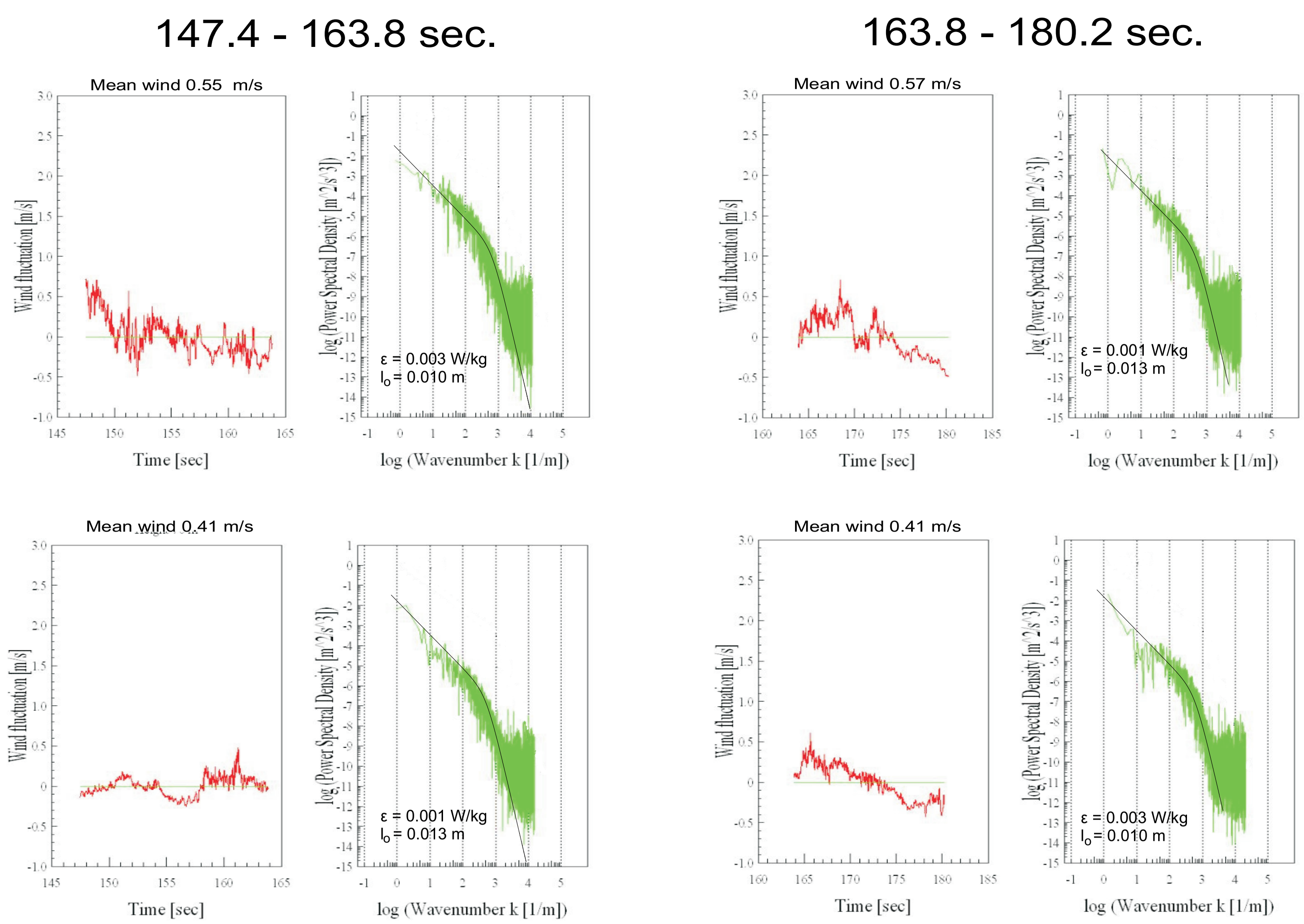

Figure 6.17: PSD analysis of exemplary consecutive wind data series acquired during measurements in the planetary boundary layer. Upper plot presents the data set collected by a 55P13 probe placed at 2 m height. The lower plot shows the wind data evaluated by a 55P13 probe set at a height of 60 cm. Mean winds are given above the plots. To every PSD turbulent theoretical spectra (black lines) have been fitted as proposed by *Lübken et al.* [1993]. The estimated turbulent kinetic energy dissipation rate ε and inner scale l_o are given for every PSD.

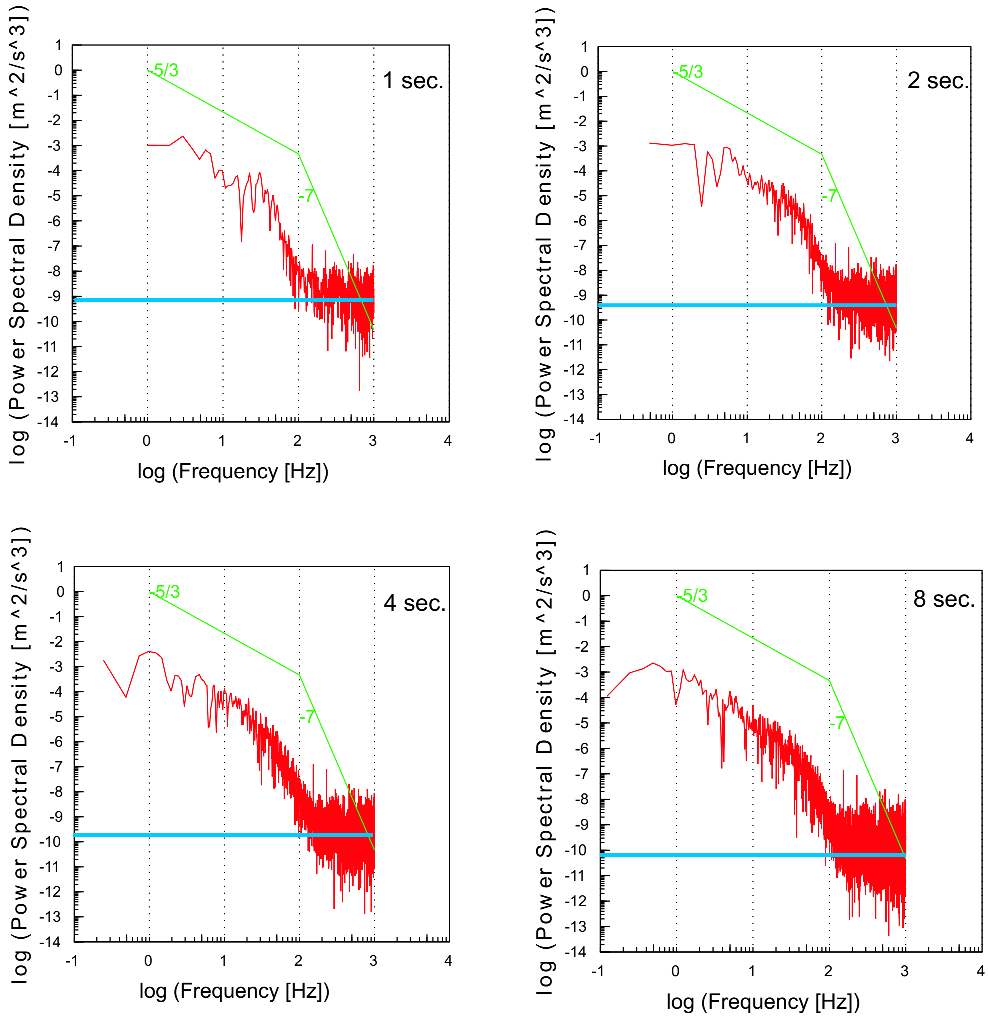

Figure 6.18: Influence of the length of the CTA data series on the spectrum noise level. The noise levels are indicated by blue lines.

7 Balloon-borne experiment

The first balloon-borne stratospheric turbulence sounding with the 55P13 CTA system took place on 12th December 2007. An instrumented balloon was launched from the Leibniz Institute of Atmospheric Physics (IAP) in Kühlungsborn, Germany (54°07'N, 11°46'E) at 10:03 UT.

The date and time of the launch were chosen considering predicted atmospheric conditions and flight tracks. The 12.12.2007 was chosen due to its relatively low precipitation and poor cloudiness. That minimized the humidity influence and contamination effect on the sensor. Furthermore, thick clouds weaken the GPS signal and through this may impede the balloon localization. The balloon track predictions for 12.12.2007 and for surrounding days were estimated with an internet 'Balloon Track' program of University of Wyoming. It enabled choosing a suitable launch time with an estimated landing place on land and outside large lakes. This procedure reduced as well the possibility of loosing the system in the Baltic See (3.5 km distant from the IAP). In Figure 7.1 one can see the predicted track for December 12, 2007 at 10:03 UT.

The single parts of the instrument were inserted into or attached to a styrofoam 40 x 40 x 40 cm payload box. Figure 7.2 shows the payload carrying the CTA and the supporting instrumentation (RS92 Vaisala radiosonde, telemetry modem, recovery system etc.). The anemometer probe was placed vertically to the payload and above the center of mass of the styrofoam box. In this way errors from self-induced oscillations of the payload were reduced. The RS92 Vaisala radiosonde, as well as the GPS and GSM antennas were fixed outside of the box to minimize damping of the electromagnetic signals by the styrofoam. The payload was suspended from a 50 m long line from a meteorological balloon. A special unwinder let the payload slowly out as the balloon gained height.

The described system allowed us to transmit real-time measurements of CTA velocity data down from the payload package with a rate of 2 kSamples per second and radiosonde position, pressure, temperature, and humidity data roughly once every two seconds. Other important characteristics of the instrument are:

- autonomous operations for few hours onboard a stratospheric platform as an independent payload
- resources minimization in terms of mass (3 kg) and operational requirements
- working environment compatible with Earth upper stratospheric conditions (pressure, temperature)
- instrument partly recoverable and re-usable with minimum refurbishment

Figure 7.1: Track prediction of the 12.12.2007 flight. The chart was provided by the University of Wyoming's "Balloon Track" program from: http://weather.uwyo.edu/polar/balloon_traj.html.

- two simultaneous data storage methods

Additionally, at 06:56 UT and at 12:55 UT the same day, meteorological balloons with RS92 Vaisala radiosondes were launched. Thus, temperature and wind profiles provided by the radiosonde during the CTA flight could be properly analyzed. The data from the surrounding soundings provided the time resolution of the atmospheric background perameters.

7.1 Measurements overview

The balloon-borne experiment from 12 December 2007 provided interesting data, that enabled investigation of the wind field in the stratosphere with a very high spatial resolution. An overview of the flight is included in Table 7.1. The table shows the basic information on the flight and the CTA data acquired during the experiment. The sounding started at 10:03 UT and finished after about 2 hours, the maximum altitude reached by the balloon equaled 35309 m. The CTA was turned on 10 minute before the launch and provided more than 2 hours of data. The 20% of data gaps in CTA measurements during the ascent were caused by problem with steering of the telemetry

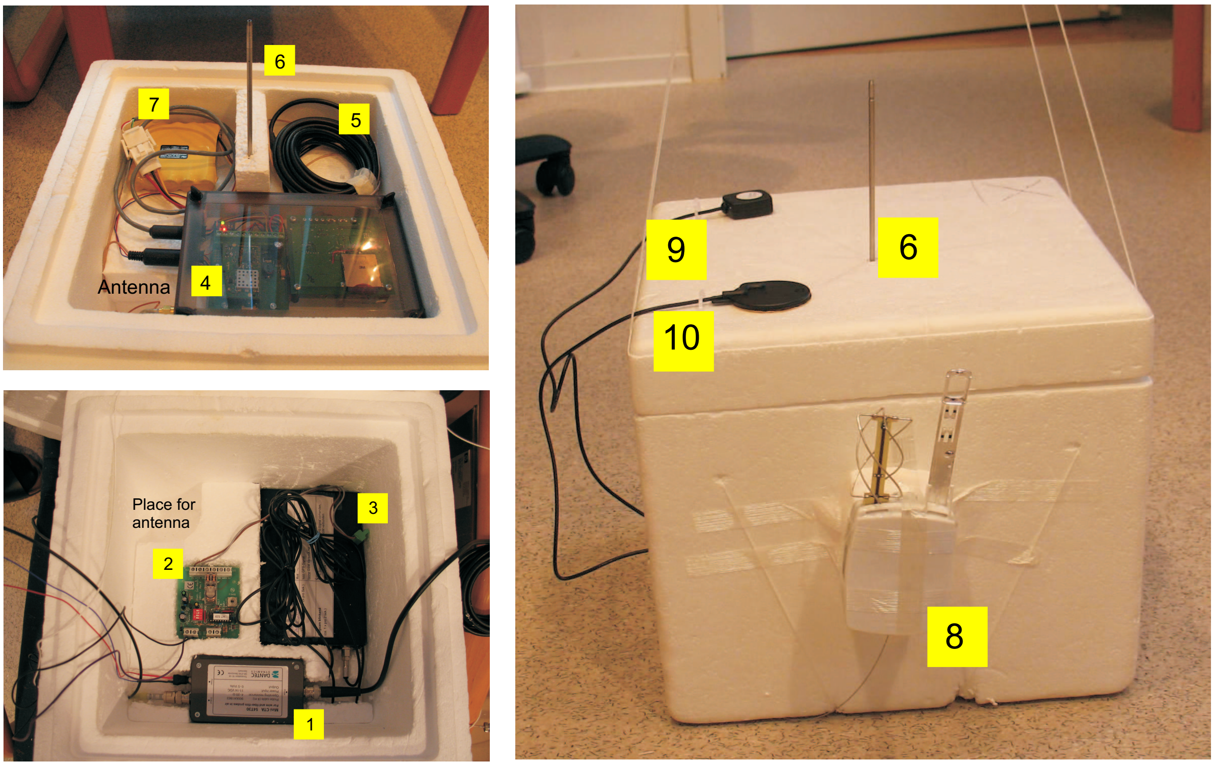

Figure 7.2: Payload of the meteorological balloon used at 12.12.2007 for the stratospheric turbulence sounding. In the upper left photo: upper level of payload box with the data conversion and storage modem (4), probe cable (5), probe body (6) and battery (7). Lower left photo: lower level of the payload with MiniCTA-bridge (1), time relay (2) and the recovery system (3). The photo on the right-hand side: styrofoam box with attached radiosonde (8) and GPS and GSM antennas of the recovery system (9,10); at the top of the box the CTA's probe body (6).

antenna. Normally, the GPS signal from the radiosonde enables the automatical steering of the receiving telemetry antenna. Since the GPS reception of the radiosonde was erroreous, the position of radiosonde could not be estimated and the automatical steering mode of the receiving telemetry antenna was disabled. The further steering was provided manually according to the earlier developed track prediction map (Figure 7.1). If the received signal level was too low to acquire the data, the antenna had to be manually adjusted. Then the data gaps occurred. During ascent 80% of the data were received. In the troposphere approximately 95% and in the stratosphere 40%. Therefore, in the stratosphere we got 30 minutes of data acquired in 1.25 hour of measurements.

The reasons of the lack of the radiosonde GPS signal could have been the vicinity of the styrofoam and the fast rotation of the payload, to which the radiosonde was attached. To localize the radiosonde three satellites have to be detected simultaneously. The rotation of the payload caused shadowing of the radiosonde from the satellites. That made the synchronization impossible. The strong rotation of the payload can be observed in temperature measurements carried out during the flight. Figure 7.3 shows three up-leg profiles from 12.12.2007 acquired during 6:56, 10:03 and 12:55 UT soundings. The second sounding was the one with the CTA instrument. From the plots it is obvious that the second flight varied significantly from the two others. The fluctuations in the temperature field indicate strong rotation of the payload. The radiosonde was placed on one of the walls of the payload box. During the rotation it was turned in the sun direction or was hidden in the shadow. That resulted in changes of the measured temperature.

Radiosonde	
Launch Localization	54°07'N, 11°46'E
Launch Altitude	70 m
Launch Time	10:03:00
End Time	11:55:22
Measurements Time Length	01:52:22
Ground Pressure	1026.2 hPa
Ground Temperature	3.9 °C
Ground Wind Speed	1.8 m/s
Ground Wind Direction	114°
Max Altitude Time	11:31:22
Max Altitude	35309
Tropopause Altitude	10379
CTA	
Start Time	09:53:59 (∼ 10 min before launch)
End Time	11:55:14
Measurements Time Length	02:01:15
Data Lack (Ascent)	20%

Table 7.1: Radiosonde and CTA data overview from the 12.12.2007 10:03 UT flight. The time is given in UT.

Another problem that occurred after the flight was a lack of response from the recovery system. Although the GSM antenna was working properly (the mobile phone number reception was possible) more than 24 hours after the impact, the system was not able to localize its position. Possibly, like in the case of the GPS from the radiosonde, the styrofoam weakened or completely impeded the signal. Or there was a leakage of the recovery system battery. The Li-Polymer battery was not placed in a pressurized container and possibly did not stand the conditions at the high altitudes. Since the location of the impact could not be directly estimated from the GPS data, it was obtained approximately from the GSM signal. The search field was selected as area enclosed by a circle of a radius of 3 km around one of the transceiver GSM antennas. Eventually,

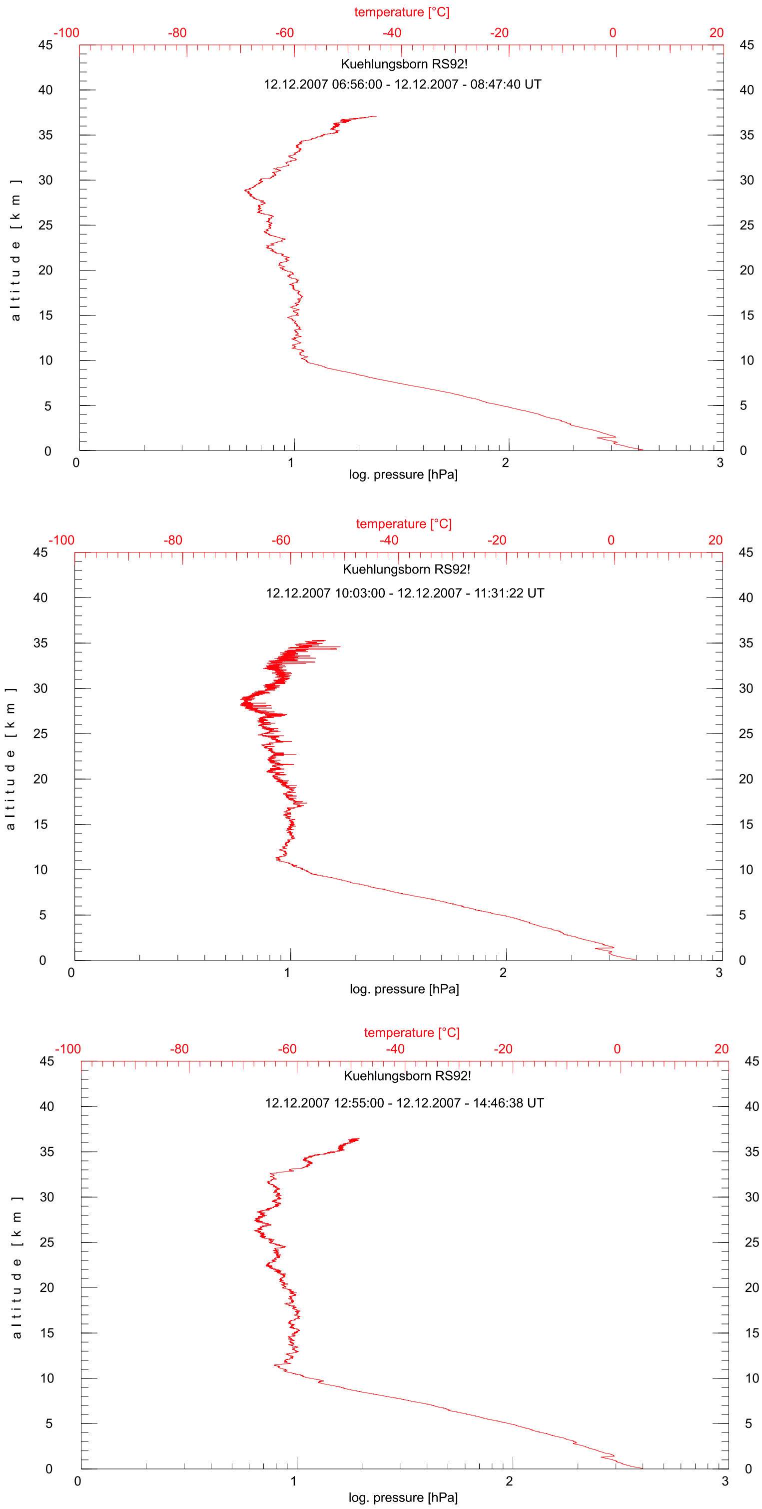

Figure 7.3: RS92 Vaisala radiosonde temperature up-leg profiles from 12.12.2007.

the system equipped with the SD-card was not found. Due to this, all further analyzed CTA data are the time data series acquired from the telemetry system.

The CTA raw data acquired during the flight are shown in Figure 7.4. The data are averaged in 1-second steps. As one can see in Figure 7.4, the voltage provided by the CTA changes drastically with altitude. Above approximately 10 km we observe a very steep slope. The slope is due to the atmospheric conditions. Figure 7.5 shows voltage data converted into wind data. The wind speed is given in arbitrary units due to the dependance of the calibration on temperature and air density (cf. Chapters 3.5 and 6.2). As in the voltage data from Figure 7.4, the wind speed profile also has the artificial slope (described below). This effect however, does not influence strongly our FFT analysis. We obtain our spectra in 4 seconds periods and during such short time the CTA does not experience significant changes in the background conditions.

Red points in Figure 7.5 present the wind data without any corrections. This data set indicates a slope into the direction of lower values above about 10 km. It agrees with the voltage data characteristics. However, at the altitudes between 20 and 35 km, the observed wind values get larger. That characteristics results from the polynomial fitting of the calibration curve (see Figure 6.4). The voltage measured during the experiment has lower values, as the one that was measured at zero wind conditions during the calibration procedure. In our case the voltage value at zero wind equals 1.23 V, what is shown in Figure 7.4 as a blue vertical line. Voltage values lower than 1.23 V occur due to the insignificant correction and the polynomial fitting converts them into unrealistic wind values. This behavior emphasizes the importance of voltage correction at low air densities. Green points in the Figure 7.5 show the wind data after temperature correction of the CTA voltage. The influence of this correction is significant, but still not sufficient to provide realistic wind shear data. From the figure it is obvious, that the ambient temperature in the stratosphere is not the reason for the observed low voltage values above about 10 km. We assume that the information on the density and humidity influence on the CTA response will explain this characteristics. More about the attempts of solving the density issue is included in Chapter 7.4.

From the radiosonde data several interesting layers for turbulence examination can be identified. Figure 7.6 shows the Brunt-Väisälä frequency as a measure of static stability from the radiosonde temperature profile. The four regions between dotted lines with low N^2 indicate layers, where the flow can be expected to be turbulent. To every layer a number between 1 and 4 is assigned. Analysis of the CTA data within those layers is enclosed in Chapter 7.2.

7.2 CTA data analysis

The data analysis of the four layers in shown in Figures 7.7, 7.8, 7.9 and 7.10. Figure 7.7 denotes to the layer between 21.5 km and 22.5 km, Figure 7.8 to the layer between 24 km and 24.8 km, Figure 7.9 to the layer 27 km to 29 km and Figure 7.10 to the layer 31.5 km and 32.5 km. Due to the mentioned telemetry problems, data gaps occurred. In layer number 1 only 32% of the data were received, in 2nd layer 44%, in 3rd 47% and

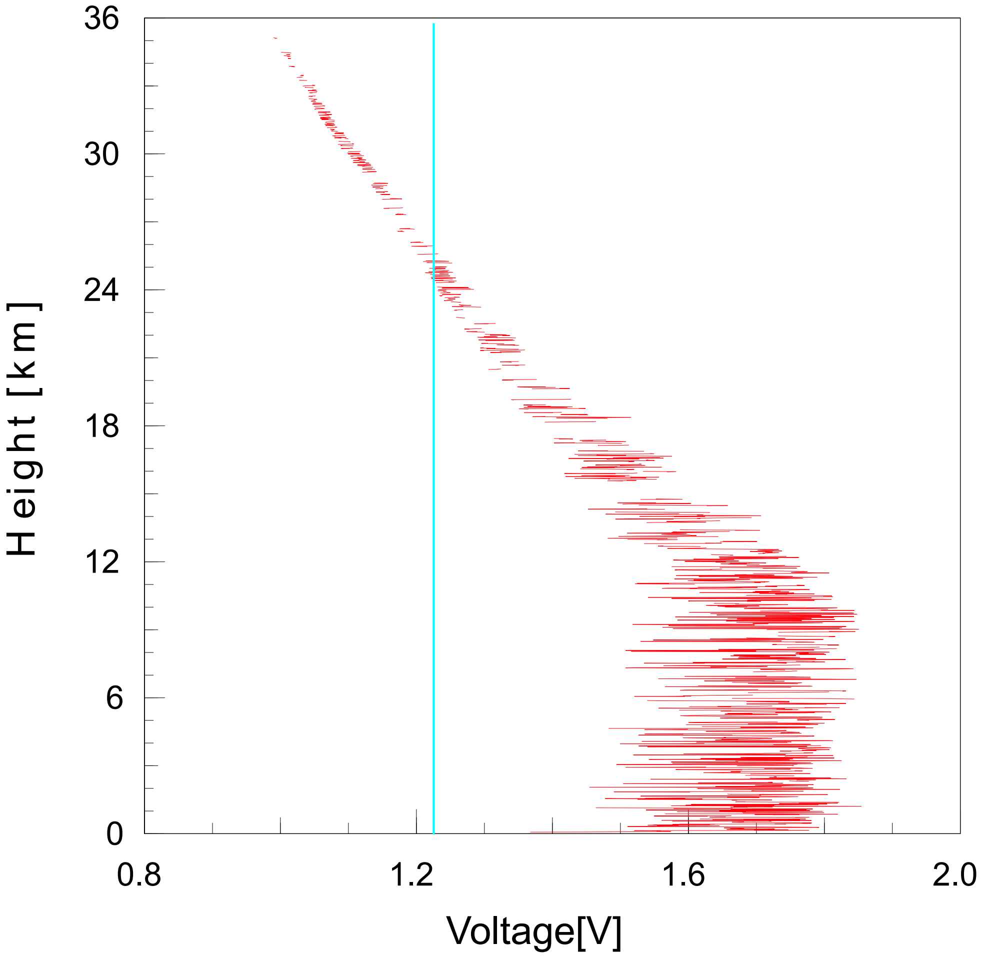

Figure 7.4: Raw data acquired with the CTA during the 12.12.2007 sounding. The red color shows voltage data acquired during the stratospheric sounding and averaged in 1-second steps. The blue line indicates voltage equal 1.23 V. It is a value at which the CTA measures zero wind velocity under the on-ground conditions.

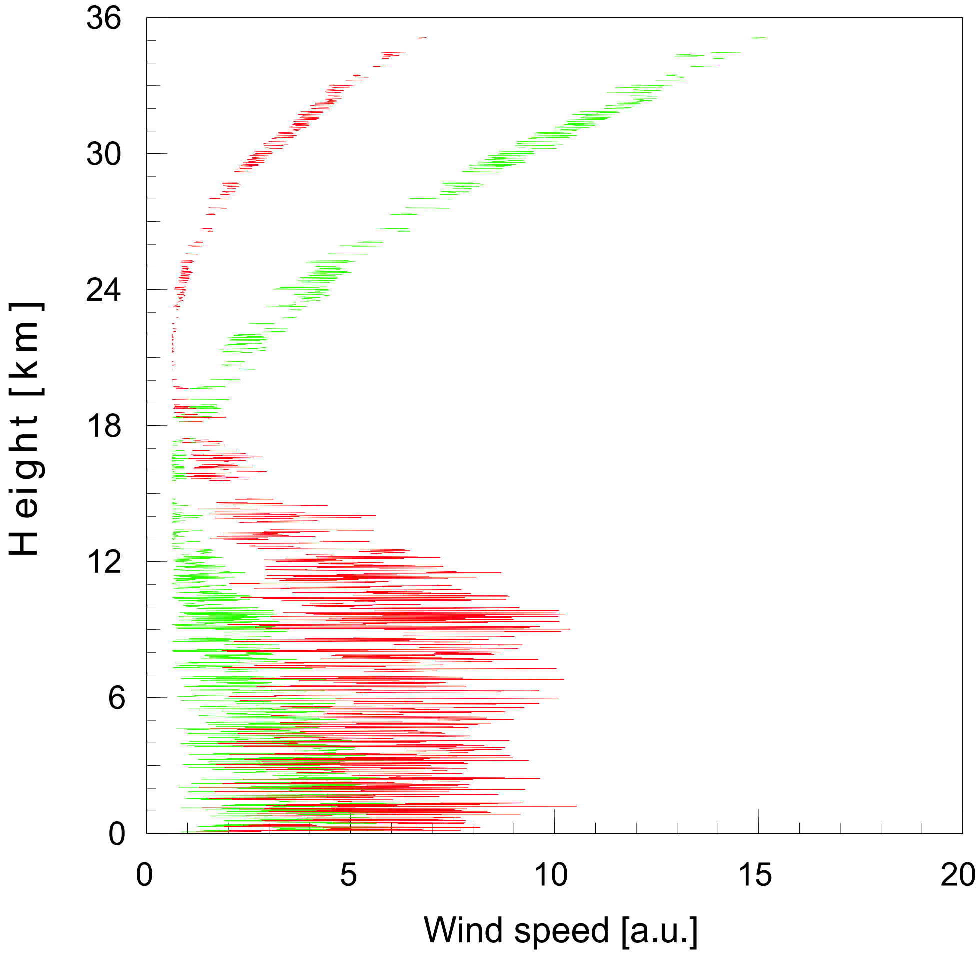

Figure 7.5: Wind shear calculated from the raw CTA data acquired during the flight from 12.12.2007. The red points represent wind without temperature correction and the green points with temperature correction.

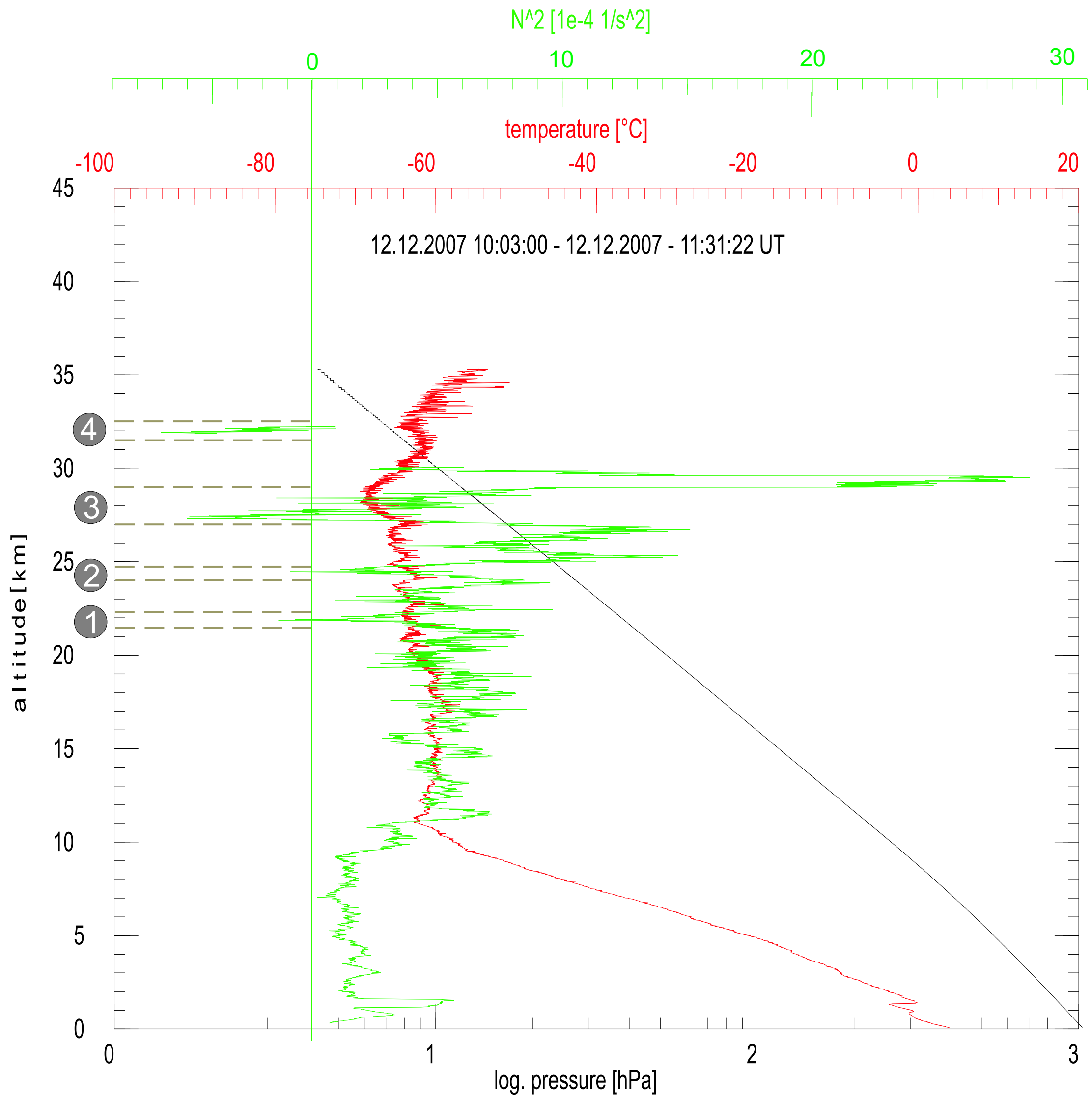

Figure 7.6: Brunt-Väisälä frequency calculated from the radiosonde data from 12.12.2007, 10:03 UT flight. Values below 0 indicate possible turbulent layers. Numbers between 1 and 4 refer to the selected layers 1 - region between 21.5 km and 22.5 km, 2 - between 24 km and 24.8 km; 3 - between 27 km and 29 km and 4 - between 31.5 km and 32.5 km.

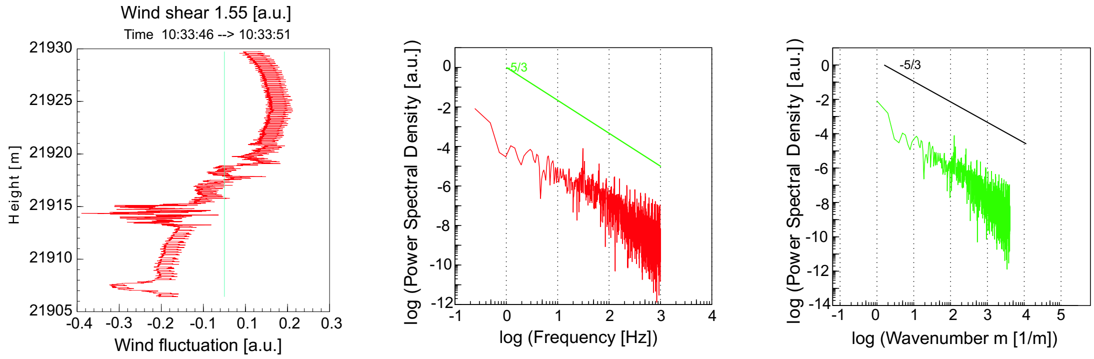

Figure 7.7: Layer 1 (21.5 - 22.5 km). 4-seconds long time data series, frequency PSD and wavenumber PSD.

in the highest layer 59%. That is why only a few exemplary plots from every layer are presented. From the acquired data the Fourier power spectral density of the measured altitude profile was derived and analyzed in terms of its spectral shape. The wind values are presented in arbitrary units (a.u.), due to the insufficient corrections of the acquired CTA voltage. In all presented frequency spectra a vibration of approximately 17 Hz can be obtained. This vibration is also visible in the time data series of the four layers. We assume that the payload vibrated during the ascent and the signal is the response of CTA on the apparently changing wind direction (see Chapter 6.1.3).

Charts on the right-hand side of Figures 7.7, 7.8, 7.9 and 7.10 show the spectral analysis of the estimated turbulence layers with respect to vertical wavenumber m. The two higher layers (Figures 7.9 and 7.10) show $-5/3$ slope only at the wavenumbers above $\sim 10^2$ with a PSD less than 10^{-6}. That is the region where the noise occurs and plays significant role (cf. Chapter 6.2 and Chapter 6.4). Secondly, in both layers a strong PSD decrease occurs at about 100 Hz. The lower layers (Figures 7.7 and 7.8) have the $-5/3$ slope starting at the wavelengths equal about 1 m^{-1} and ranging higher PSD scales. We assume that the differences in various layers result from not sufficient correction of acquired voltage due to atmospheric conditions. The influence of this factor seems to have larger impact at higher altitudes than at lower ones. Secondly, a substraction of a polynomial from the signal should solve the problem with the PSD decrease at 100 Hz in the 3rd and 4th layer.

The radiosonde data acquired during the 12.12.2007 sounding enabled identification of 4 possible turbulent layers. Due to the very high frequency response of the CTA, we got spatial resolution of 0.25 cm. The analysis of those layers shows, that in the 1st (21.5 - 22.5 km) and the 2nd (24 - 24.8 km) layer a high energetic inertial subrange occurs (that is, the part of the spectrum characterized by a $m^{-5/3}$ spectral dependence). That can indicate the turbulence in this region. However, full analysis of those regions requires better understanding of the temperature, density and humidity effects on the CTA response.

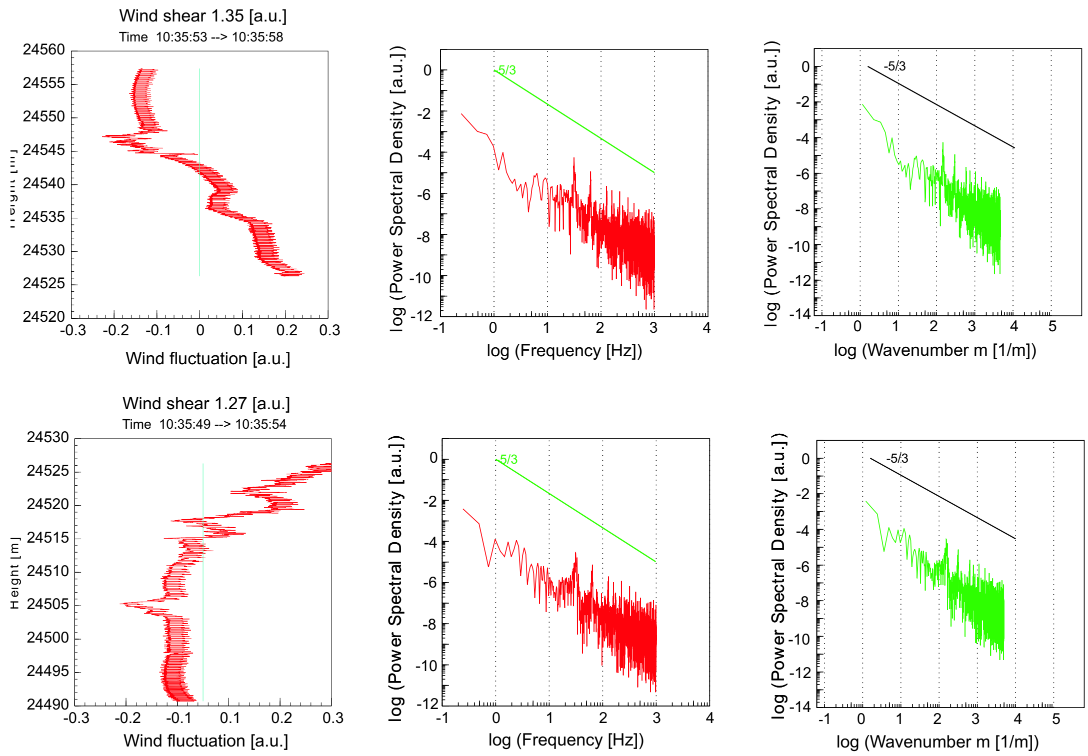

Figure 7.8: Layer 2 (24 - 24.8 km). 4-seconds long time data series, frequency PSD and wavenumber PSD.

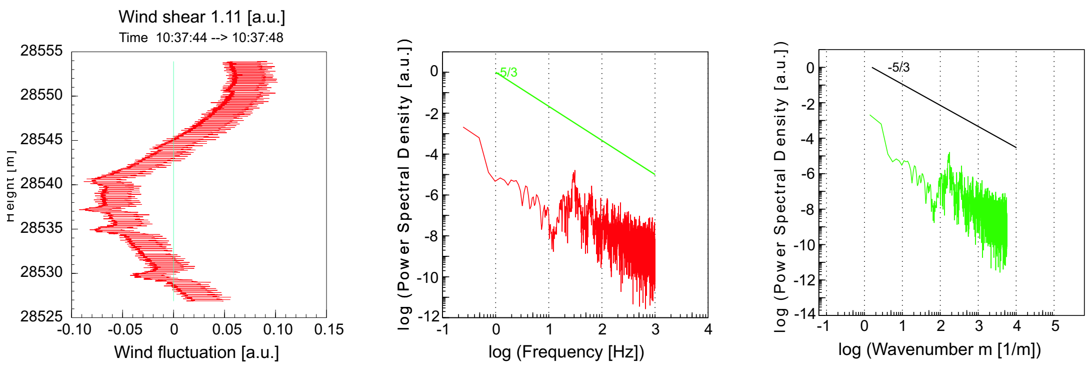

Figure 7.9: Layer 3 (27 - 28 km). 4-seconds long time data series, frequency PSD and wavenumber PSD.

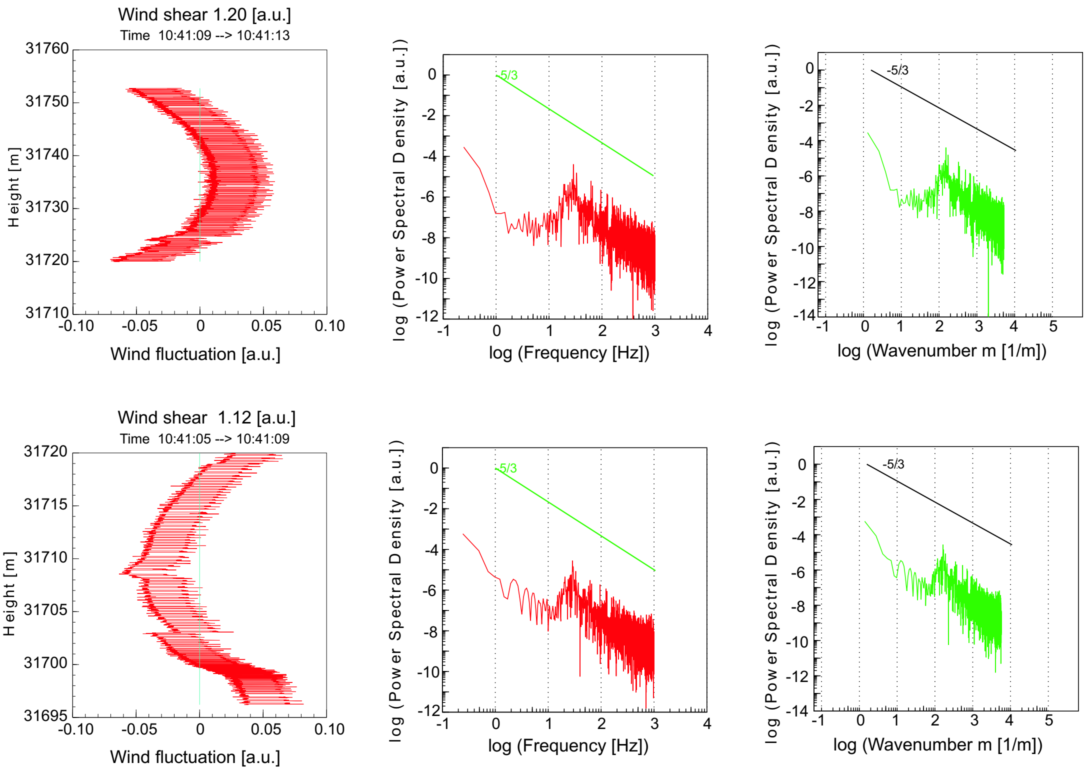

Figure 7.10: Layer 4 (31.5 - 32.5 km). 4-seconds long time data series, frequency PSD and wavenumber PSD.

7.3 Comparison of CTA and radar measurements

Simultaneously to the in situ measurements, investigation of the fluctuation in the atmospheric wind field was performed by remote sensing. The Ostsee-Wind-Radar (OSWIN) running in IAP Kühlungsborn is a VHF-radar working at a frequency of 53.5 MHz. In Figure 7.11 one can see a wind field over IAP from 12.12.2007 with a noticeable layer of high wind speeds at altitude of 10-11 km. The north-eastern winds in the lower troposphere confirm the predicted flight track (Figure 7.1). The time of the balloon launch (10:03 UT) is shown by a red line.

Figure 7.12 compares wind data acquired with the radar system and with the 55P13 probe during the flight from 12.12.2007. The OSWIN radar provides horizontal wind profile in every 3 minutes. The radar data shown in Figure 7.12 represent mean values of one hour long measurements starting from the balloon launch time at 10:03 UT. Both data sets are displayed in form of root mean squares of the fluctuating part of the wind $U'_{r.m.s}$ (Eq. 2.5) and cover the altitudes between 2 and 16 km. CTA data set is represented by a blue line, the red curve with squares corresponds to horizontal wind measurements with radar. When comparing those data sets, it is not possible to unambiguously identify any turbulent layer simultaneously sampled by the OSWIN radar and the CTA. However, the comparison of those totally independent measurements allows us to assume that the acquired CTA and radar data agree well with each other.

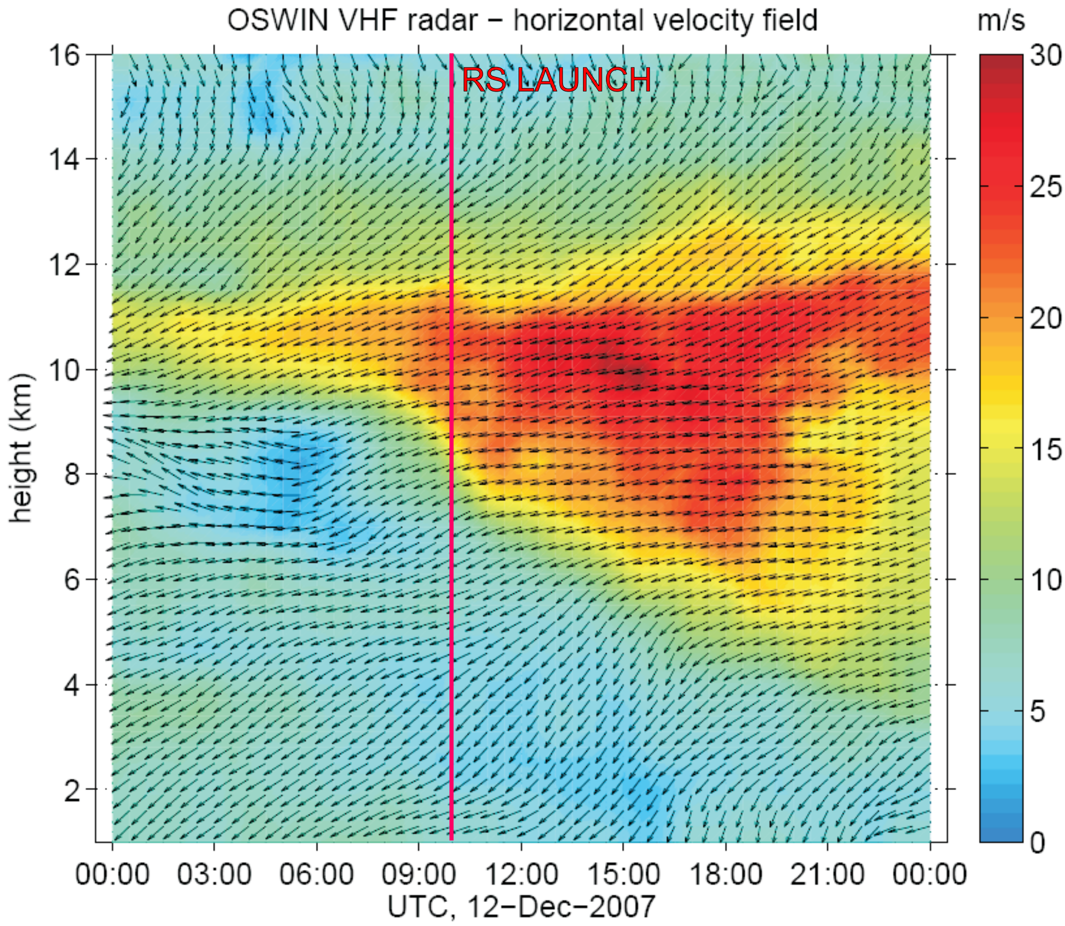

Figure 7.11: Horizontal wind field over Kühlungsborn, Germany on 12th December 2007. Arrows show direction of wind, the velocities are represented by colors.

That let us assume that the CTA gives a good representation of the wind shear in the atmosphere.

7.4 Discussion

The measurements in the stratosphere from 12.12.2007 provide a large amount of wind shear data and some information on the existence of turbulent layers along the balloon track. The Brunt-Väisälä frequency calculated from the potential temperature (Figure 7.6) indicated 4 layers with lower level of static stability, where the turbulence could have been expected. However, to confirm unambiguously the appearance of the turbulence in those layers, the CTA response under atmospheric conditions has to be analyzed. Understanding of the influence of pressure, temperature and humidity is necessary for sophisticated data corrections and preparation of further stratospheric soundings.

The raw data acquired during the stratospheric experiment showed strong influence of the ambient conditions on the CTA response. Before conversion of the raw data into the wind values, we provided a temperature correction on the data. Nowadays we look for a solution that would enable accurate formula for corrections due to ambient pressure and humidity. Plot 7.13 shows voltage data provided by the CTA at the altitudes between 70 m and approximately 35 km. The data set is compared with the data from the experiment in the vacuum chamber (Chapter 6.2). In this case the pressure scale was converted to geometric altitudes. Above 12 km one can notice a strong decrease of the voltage in both cases. Furthermore, the fluctuations above this altitude are significantly smaller than in the troposphere, where the density is higher. It means that our assumptions were right and the probes have to be calibrated in a vacuum chamber before stratospheric soundings.

To provide the accurate data analysis, the mathematical description of the FFT has to be deeply analyzed and adjusted to the characteristics of the measurements. Especially the mean wind value utilized for the frequency-wavenumber conversion should be corrected due to pendulum movement of the payload and due to the wind shear influence. Substraction of the polynomial from the data sets before the FFT analysis should prevent leakage from large scales to smaller ones.

It is important to clear the noise level and its changing position in the spectrum. Comparison of the data from the tests in the vacuum chamber (Chapter 6.2), from the on-ground measurements (Chapter 6.4) and the flight (Chapter 7.2) show different levels at which the noise occurs. The noise level decreases with increasing length of the data set (e.i. samples amount). The main reason for that is the FFT analysis of larger data sets resolves finer scales. However, it is difficult to estimate if the acquired resolution is due to the CTA measurement or due to mathematical description. This effect should be further analyzed and the FFT algorithm has to be adjusted according to the data set lengths.

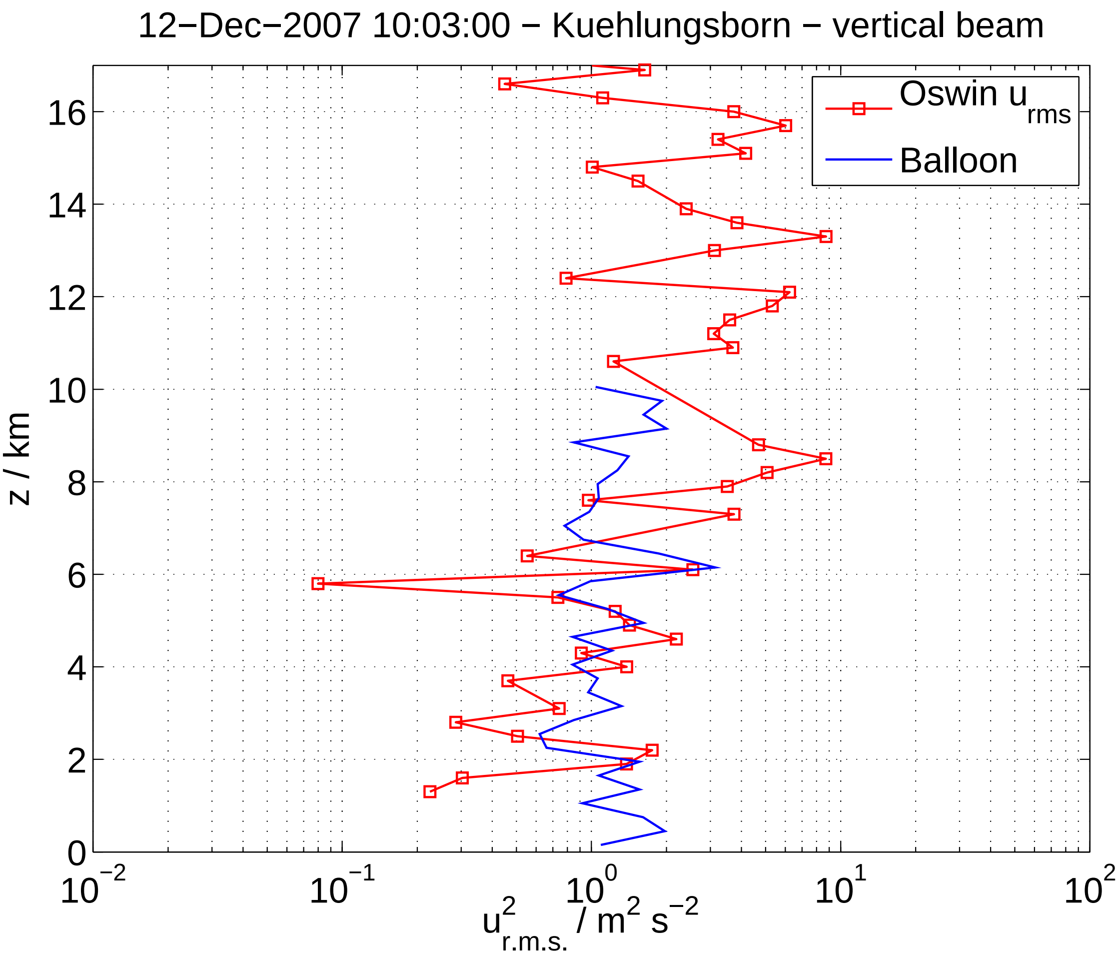

Figure 7.12: Comparison of root mean square $U'_{r.m.s}$ velocity determined from data acquired with OSWIN radar and with 55P13 CTA system on 12th December 2007. The CTA $U'_{r.m.s}$ is averaged in 100 m steps. The radar data represent a averaged one hour profile (between the balloon launch time at 10:03:00 and 11:03:00). The radar measurements were preformed in 3 minutes periods. The u in the plot corresponds to U'.

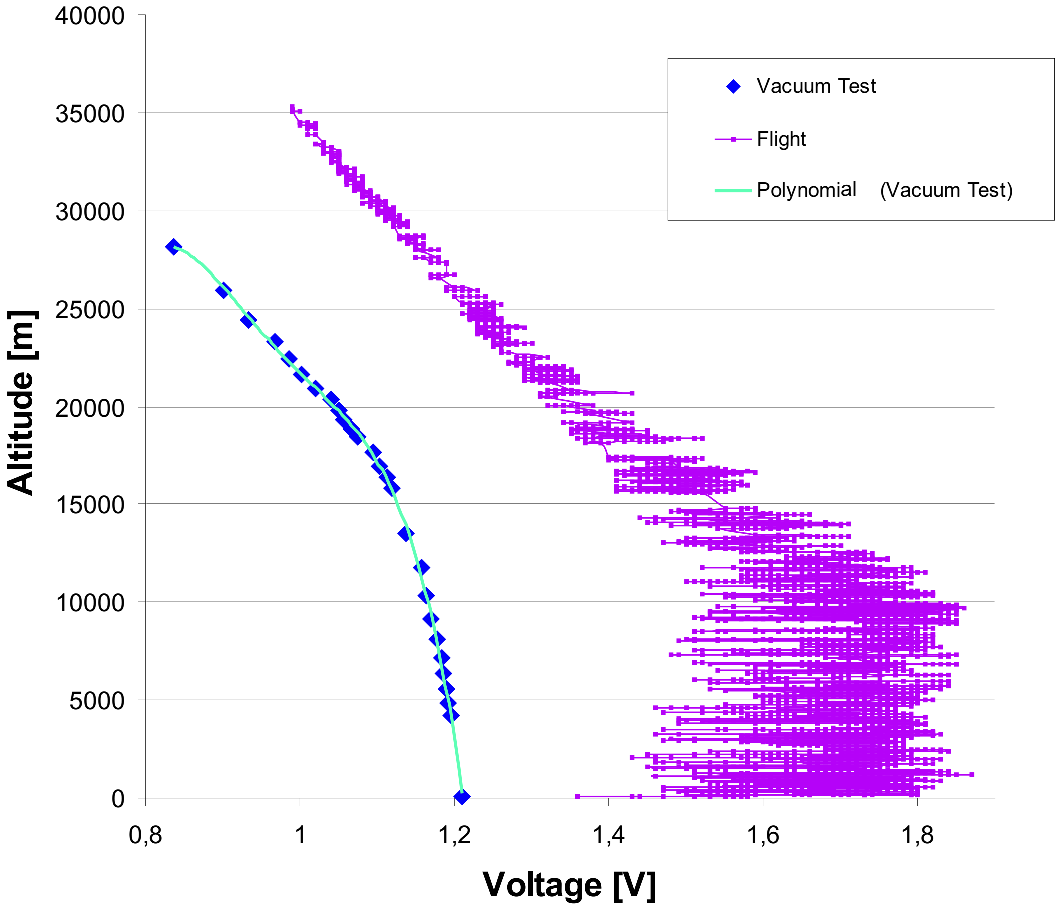

Figure 7.13: Raw data acquired with CTA during the 12.12.2007 sounding and influence of the pressure on the CTA measurements. The blue points with polynomial curve correspond to the voltage measured in the vacuum test (see Chapter 6.2). The violet color shows voltage data acquired during the stratospheric sounding and averaged in 1-second steps.

8 Summary and outlook

The results enclosed in the Chapter 7 showed that the constant temperature anemometer (CTA) is a suitable instrument for the stratospheric turbulence soundings. The CTA is a device that provides very high resolved temporal and spatial information on the flow dynamics. However, up to now this instrument was not used for investigation of the stratospheric turbulence. The main aim of this thesis was to prepare and test the CTA with regard to this new application, as well as to perform a stratospheric sounding and to present the first results of the balloon-borne experiment.

Application of the CTA for the stratospheric turbulence soundings required many tests in the wind channel, laboratory and planetary boundary layer. Through the experiments we gained information on the behavior of the anemometer at low pressure and at changing wind direction. We estimated the influence of the contamination on the CTA response and investigated the noise level. Furthermore, our 55P13 probe was compared with 55P03 probe under outdoor conditions. We tested the CTA in planetary boundary layer at different heights and researched the turbulence in this layer. All data acquired during the experiments were handled and analyzed with a WindCata software developed within this work.

The new instrument for stratospheric turbulence soundings introduced in this thesis consists of the CTA and supporting instrumentation, that enables data correction, compression, storage and transmission from a flying platform. All of necessary devices were combined and lifted to the stratosphere with a balloon. During the first flight on 12th December 2007 we acquired high resolved wind shear data between the altitudes of 0 and about 35 km. Due to the high response frequency of the CTA (2 KHz), we got a spatial resolution of measurement of 0.25 cm at balloon ascent rate of 5 m/s. Up to now, such high resolution has never been reached in the stratosphere.

In the future we plan to couple our soundings to special geophysical situations. The time of flights will be chosen according to the probability of occurring of turbulence. Furthermore, we want to be able to compare the CTA with radar and lidar data. In the future a simultaneous measurement with those methods are planed. However, before those experiments can be carried out, the balloon-borne instrument has to be improved.

The recovery system has to be equipped with a batter that would be able to stand the low stratospheric pressure. Another important factor is the placement of the GPS antenna of the recovery system. The best solution is to put it away from the styrofoam box to minimize the signal dumping. The same has to be done with the radiosonde GPS antenna. The idea is to attach the radiosonde to a rope below the payload. It will not only minimize the signal damping, but also protect the temperature measurements from the influence of the payload rotation and sunshine reflection.

Furthermore, reduction of the strong payload rotation has to be performed. It can be done with help of a vane or with stabilized balloons. In comparison with the classical balloons, stabilized balloons remain always in laminar flow and are distinguished by a strong reduction of parasite movements, as well in the vertical axis (ascent speed) as in the horizontal plane (4 to 5 m/s). The CTA data from the stabilized balloon payload will be more representative and not burdened with additional information from oscillations.

The mathematical description of the FFT has to be deeply analyzed and adjusted to the characteristics of the measurements. Especially the mean wind value utilized for the frequency-wavenumber conversion should be corrected due to pendulum movement of the payload and due to the wind shear influence. Substraction of the polynomial from the data sets before the FFT analysis should prevent leakage from large scales to smaller ones. Moreover, there are still many data corrections and data analysis algorithms, that will be introduced into the WindData program in the future. Because of that, it is important to implement batch processing into the software. It will speed up and simplify the data analysis.

In the next soundings the gold plated 55P03 probes will be used. They have higher accuracy at fine scales than the 55P13s and due to this provide more representative results. Now it is important to test the 55P03 probes in the same way as it was performed with the 55P13 (cf. Chapter 6).

In October 2008, our balloon-borne instrument took part at the BEXUS (Balloon Experiments for University Students) programme organized by German Aerospace Center (DLR, Deutsches Zentrum für Luft- und Raumfahrt) and the Swedish National Space Board (SNSB) in cooperation with European Space Agency (ESA). The IAP prepared two projects and both of them were accepted. One of them, called TURAWIND, concerned the simultaneous turbulence measurements with two 55P03 CTA probes. The research campaign was carried out in Esrange in Kiruna, Sweden. The probes were placed above a payload of a balloon of a volume of 12000 m^3 and lifted to an altitude of about 29 km. The experiment finished with success and nowadays the acquired data are being analyzed.

List of Figures

1.1 A temperature profile at Kühlungsborn, Germany 1
1.2 Length scales of importance for turbulence in the atmosphere 5
1.3 Gravity waves visible in temperature field measured at night 12 - 13 November 2003 over Kühlungsborn, Germany. 6
1.4 Comparison of two power spectral density (PSD) of in-situ turbulence measurements 8

2.1 Energy spectrum of turbulence 13

3.1 Constant Temperature Anemometer principle diagram 20
3.2 Picture of hot-wire probe 55P13 24
3.3 Sensor types: 55P13 and 55P03 24
3.4 The dependence of the constant temperature hot-wire voltage E_w on the air velocity U, for various ambient temperatures. 27
3.5 Response of CTA on wind equal at various ambient temperature. 28

4.1 The DigiCora®III Sounding System MW31 developed by Vaisala 30
4.2 Telemetry modem 31
4.3 Characterization of 869 MHz helical transmitting antenna. 33
4.4 Receiving antenna on the roof of IAP, Kühlungsborn. 34

5.1 Screenshot of module for manual inscription of the ambient conditions. . 36
5.2 Screenshot of the main panel of the analysis software 37
5.3 Screenshots of modules for analysis of a whole flight data set. 38

6.1 The Göttingen type wind tunnel schema. 42
6.2 Calibration curves of two 55P13 and one 55P03 probes. 43
6.3 Comparison of differential sensitivity of two 55P13 probes and one 55P03 probe 44
6.4 Possible calibration fittings. 44
6.5 Three calibration characteristics of one 55P13 probe obtained at different days. 45
6.6 Experimental setup for the investigation of the yaw effect 46
6.7 Comparison of the observed velocities for changing 55P13 sensor yaw orientation. 47
6.8 Experimental setup for the investigation of the pitch effect 48

6.9 Comparison of the observed velocities for changing 55P13 sensor pitch orientation. . . . 49
6.10 Ambient pressure influence on the 55P13 probes' response. . . . 50
6.11 PSD of CTA data acquired in the vacuum chamber at 1013 hPa in no-wind conditions. . . . 51
6.12 Comparison of wind fluctuations acquired with the 55P03 and the 55P13 probe in the planetary boundary layer from 14th July 2008. . . . 54
6.13 Comparison of PSD of 4 seconds long data sets acquired with the 55P03 and the 55P13 probe on 14th July 2008 . . . 55
6.14 Wavelet power spectrum of wind fluctuations measured with the 55P03 CTA probe during measurements within the planetary boundary layer on 14th July 2008. . . . 56
6.15 Schema of an experiment in the planetary Prandtl boundary layer with two 55P13 probes placed at different heights. . . . 57
6.16 Wind data series from the measurements in the planetary boundary layer from 10th September 2008 . . . 57
6.17 PSD analysis of exemplary consecutive wind data series acquired during measurements in the planetary boundary layer. . . . 58
6.18 Influence of the length of the CTA data series on the spectrum noise level. 59

7.1 Track prediction of the 12.12.2007 flight . . . 62
7.2 Payload of the meteorological balloon used on 12.12.2007 for the stratospheric turbulence sounding . . . 63
7.3 RS92 Vaisala radiosonde temperature up-leg profiles from 12.12.2007 . . 65
7.4 Raw data acquired with the CTA during the 12.12.2007 sounding. . . . 67
7.5 Wind shear calculated from the raw CTA data acquired during the flight from 12.12.2007. . . . 68
7.6 Brunt-Väisälä frequency calculated from the radiosonde data from the 12.12.2007, 10:03 UT flight . . . 69
7.7 Spectral analysis of the 1st layer . . . 70
7.8 Spectral analysis of the 2nd layer . . . 71
7.9 Spectral analysis of the 3rd layer . . . 71
7.10 Spectral analysis of the 4th layer . . . 72
7.11 Horizontal wind field over Kühlungsborn, Germany on 12th December 2007 73
7.12 Comparison of $U'_{r.m.s}$ velocity determined from data acquired with OSWIN radar and with 55P13 CTA system. . . . 75
7.13 Raw data acquired with CTA during the 12.12.2007 sounding and influence of the pressure on the CTA measurements. . . . 76

Bibliography

Afanasyev, Y. D., and W. R. Peltier (2001), Numerical simulation of internal gravity waves breaking in middle atmosphere: The influence of dispersion and three-dimensionalization, *Journal of the Atmospheric Science*, *58*, 132–153.

Alisse, J., P. H. Haynes, J. Vanneste and C. Sidi (2000), Quantifiation of stratospheric mixing from turbulence microstructure measurements, *Geophysical Research Letters*, *27*(17), 2621–2624.

Barat, J. (1982), Some characteristics of clear-air turbulence in the middle stratosphere, *Journal of the Atmospheric Science*, *39*(11), 2553–2564, doi: 10.1175/1520-0469(1982)039<2553:SCOCAT>2.0.CO;2.

Barat, J., and F. Bertin (1983), On the contamination of stratospheric turbulence measurements by wind shear, *Journal of the Atmospheric Science*, *41*(5), 819–827.

Barat, J., C. Cot and C. Sidi (1984), On the measurement of the turbulence dissipation rate from rising balloons, *Journal of Atmospheric and Oceanic Technology*, *1*, 270–275.

Bellot, G. C. (1976), Hot-wire anemometry, *Annual Reviews of Fluid Mechanics*, S. 209–231.

Blackadar, A. K. (1997), *Turbulence and diffusion in atmosphere: Lectures in Enviromental Science*, Springer.

Bruun, H. (1995), *Hot-wire Anemometry, Principles and Signal Analysis*, Oxford University Press.

Dalaudier, F., M. Crochet and C. Sidi (1989), Direct comparison between in situ and radar measurements of temperature fluctuation spectra: A puzzling result, *Radio Science*, *24*(3), 311–324.

DantecDynamics (2007), Probes for hot-wire anemometry.

Engler, N., R. Latteck, B. Strelnikov, W. Singer and M.Rapp (2005), Turbulent energy dissipation rates observed by doppler MST radar and by rocket-borne instruments during the MIDAS/MaCWAVE campaign 2002, *Annales Geophysicae*, (23), 1146–1156.

Farge, M. (1992), Wavelet transforms and their applications to turbulence, *Annual Reviews of Fluid Mechanics*, *24*, 395–457.

Fritts, D. C., and M. J. Alexander (2003), Gravity wave dynamics and effects in the middle atmosphere, *Rev. Geophys.*, *41*(1), 3/1–64, doi:10.1029/2001RG000106.

Fritts, D. C., C. Bizon, A. Werne and C. K. Meyer (2003), Layering accompanying turbulence generation due to shear instability and gravity-wave breaking, *Journal of Geophysical Research*, *108*(D8).

Gatski, T. B., M. Hussaini and J. Lumley (1996), *Simulation and Modeling of Turbulent Flows*, Oxford University Press.

Gerding, M., J. Höffner, J. Lautenbach, M. Rauthe and F.-J. Lübken (2008), Seasonal variation of temperatures between 1 and 105 km altitude at 54°N observed by lidar, *Atmospheric Chemistry and Physics*, submitted.

Glover, K. M., R. J. Boucher, H. Ottersten and K. R. Hardy (1969), Simultaneous radar, aircraft and meteorological investigations of clear air turbulence, *Journal of Applied Meteorology*, *8*, 634–640.

Heisenberg, W. (1948), Zur statistischen Theorie der Turbulenz, *Zeitschrift für Physik*, *124*, 628–657.

Hicks, J. J., I. Katz, C. R. Landry and K. R. Hardy (1967), Clear Air Turbulence: Simultaneous Observations by Radar and Aircraft, *Science*, *157*(3790), 808–809.

Hocking, W. (1996), An assessment of the capabilities and limitations of radars in measurements of upper atmosphere turbulence, *Advanced Space Research*, (17), 1137–1147.

Hocking, W. K. (1985), Measurements of turbulent energy dissipation rates in the middle atmosphere by radar techniques: A review, *Radio Science*, *20*(6), 1403–1422.

Holmes, P., J. L. Lumney and G. Berkooz (1996), *Turbulence, Coherent Structures, Dynamical Systems and Symmetry*, Cambridge University Press.

Jagoda, J., N. Komerath and J. Seitzman (2005), *Unsteady Velocity Measurements in a Jet Using a Hot Wire Anemometer*, GeoriaTech, Collage of Engineering, School of Aerospace Engineering.

Jørgensen, F. E. (2002), *How to measure turbulence with hot-wire anemometers*, Dantec Dynamics.

Kalapuereddy, M. C. R., K. K. Kumar, V. Sivakimar, A. K. Ghosh, A. R. Jain and K. K. Reddy (2007), Diurnal and seasonal variability of TKE dissipation rate in the ABL over a tropical station UHF wind profiler, *Journal of Amospheric and Solar-Terrestial Physics*, (69), 419–430.

Kirchhoff, R. H., and R. Safarik (1974), Turbulence calibration of a hot wire anemometer, *American Institute of Aeronautics and Astronautics Journal*, *12*(5), 710–711.

Kolmogoroff, A. (1941), The local structure of turbulence in incompressible viscous fluid for very large Reynold's numbers, *Dokl. Akad. Nauk SSSR*, *30*, 301–305.

Latteck, R., W. Singer and W. K. Hocking (2005), Measurement of turbulent kinetic energy dissipation rates in the mesosphere by 3 MHz Doppler radar, *Advances in Space Research*, (35), 1905–1910.

Lilly, D. K., and P. F. Lester (1974), Waves and turbulence in the stratosphere, *Journal of the Atmspheric Science*, *31*(3), 800–812.

Lübken, F.-J. (1993), Experimental results on the role of turbulence for the heat budget of the upper atmosphere, Habilitation thesis, University of Bonn.

Lübken, F.-J., and G. Lehmacher (1993), First in-situ observations of neutral and plasma density fluctuations within a PMSE layer, *Geophysical Research Letters*, *20*(20), 2311–2314.

Lübken, F.-J., W. Hillert, G. Lehmacher and U. von Zahn (1993), Experiments revealing small impect of turbulence on thr enrgy budget of the mesosphere and lower thermosphere, *Journal of Geophysical Research*, *98*(D11), 20,369–20,384.

Lübken, J.-F., W. Hillert, G. Lehmacher and U. von Zahn (1992), Neutral air turbulence during DYANA: First results, *Advanced Space Research*, *12*(10), 135–139.

Lumley, J. L., and H. A. Panofsky (1964), *The structure of atmospheric turbulence*, Interscience Monographs and Texts in Physics and Astronomy, New York: Wiley.

Merceret, F. J. (1976), Measuring atmospheric turbulence wit airborne hot-film anemometers, *Journal of Applied Meteorology*, *15*, 482–490.

Muschinski, A., R. Frehlich, M. Jensen, R. Hugo, A. Hoff, F. Eaton and B. Balsley (2001), Fine-scale measurements of turbulence in the lower troposphere: an intercomparison between a kite- and balloon-borne, and a helicopter-borne measurement system, *Bounduary-Layer Meteorology*, *98*(2), 219–250, doi:10.1023/A:102652061824.

Payne, S. J. (2001), Unsteady loss in a high pressure turbine stage, Dissertation, Department of Engineering Science, Unversity of Oxford.

Press, W. H., S. A. Teukolsky, W. T. Vetterling and B. P. Flannery (1992), *Numerical Recipes, The Art of Scientific Computing*, Cambridge University Press.

Reynolds, O. (1895), On the dynamical theory of the incompressible viscous fluids and the determination of the criteria, *Philos. Trans. R. Soc. London*, *A*(186), 123–164.

Richardson, L. F. (1920), The supply of energy from and to atmospheric eddies, *Proc. Roy. Soc.*, *A*(97), 354–373.

Serafimovich, A., P. Hoffmann, D. Peters and V. Lehmann (2005), Investigation of inertia-gravity waves in the upper troposphere/lower stratosphere over northern germany observed with collocated VHF/UHF radars, *Atmospheric Chemistry and Physics*, *5*, 295–310.

Siebert, H., K. Lehmann and R. Shaw (2005), On the use of hot-wire anemometer for turbulence measurements in clouds, *Journal of Atmospheric and Oceanic Technology*, *24*, 980–993, leibniz-Institute for Tropospheric Research.

Stearns, L. P., P. Kuhn, R. L. Kurkowski and F. Caracena (1981), Clear Air Turbulence: An Airborne Alert System, *Science*, *213*(4511), 1007–1008.

Steinback, P. C., and K. Nagabushana (1996), Review of hot-wire anemometry, *Electronic Journal of Fluid Engineering, Transation of the ASME.*

Strelnikov, B. (2006), In situ measurements of small scale neutral and plasma dynamics in the mesosphere/lower thermosphere region, Dissertation, University of Rostock.

von Weizsäcker, C. (1948), Das spektrum der Turbulenz bei großen reynoldsschen Zahlen, *Zeitschrift für Physik*, *124*, 614–627.

Wright, J. M. J. (1997), *Rawinsonde and Pibal Observations, Federal Meteorological Handbook*, Washington.

Yamanaka, M. D., H. Tanaka, H. Hirosawa, Y. Matsuzaka, T. Yamagami and J. Nishimura (1985), Measurement of stratospheric turbulence by balloon-borne "glow-discharge" anemometer, *Notes and Correspondence*, *63*(3), 483–489.

Acknowledgement

This thesis wouldn't be possible without Prof. Dr. F.-J. Lübken, who not only gave me the opportunity to work in IAP but also through his courses showed the importance of atmospheric research.

I thank my supervisor, Dr. Michael Gerding, for all the help and patience he provided me throughout the research. I also thank Torsten Köpnick for his advice about software routines and work done during development of the setup and Anne Theuerkauf for great ideas.

Moreover I'd like to thank Monika, Ulrike, Michael P., Josef, Irina, Boris, Mischa, Armin, Markus, Marius and of course Jörg Trautner for his work designing the dipole antenna.

I thank Dr. Martin Brede from the Chair of Fluid Mechanics at the University of Rostock for enabling and organizing the calibration and tests of the anemometer in a wind tunnel. I also thank Ulf Grebin and Mario Jensch for their help during the running of those measurements.

Finally, I thank the administration staff and other coworkers in IAP for their patience in dealing with me and my poor knowledge of German and for their inestimable help in learning the language.

Declaration of Autorship

I hereby ensure that the thesis at hand is entirely my own work, employing only the referenced media and sources.

Rostock, 24 November 2008

Olga Alicja Sumińska